MAGYAR ÁLLAMI
EÖTVÖS LORÁND
GEOFIZIKAI INTÉZET

GEOFIZIKAI
KÖZLEMÉNYEK

ВЕНГЕРСКИЙ
ГЕОФИЗИЧЕСКИЙ
ИНСТИТУТ
ИМ Л. ЭТВЕША

ГЕОФИЗИЧЕСКИЙ
БЮЛЛЕТЕНЬ

EÖTVÖS LORÁND
GEOPHYSICAL INSTITUTE
OF HUNGARY

GEOPHYSICAL TRANSACTIONS

CONTENTS

VOL. 29. NO. 4. DECEMBER 1983. (ISSN 0016—7177)

BUDAPEST

TARTALOMJEGYZÉK

СОДЕРЖАНИЕ

GEOPHYSICAL TRANSACTIONS 1983
Vol. 29. No. 4. pp. 265—296

INTERPRETATION OF GRAVITY AND MAGNETIC ANOMALIES IN AREAS OF COMPLICATED TECTONICS (THE VELENCE HILLS)

Anna PINTÉR*

The Velence hills are surrounded by a plain covered by young Neogene (Pannonian) formations. The limited number of borehole data give insufficient information for a detailed knowledge of the deep structure. The paper presents experiments to delineate the most important deep structural elements, starting out from different versions of gravity and magnetic maps. A sketch map is given summarizing the results which is thought to be useful for further geophysical and drilling research. The methodological considerations concerning the gravity and magnetic methods could also be useful in interpreting the gravity and magnetic anomalies of similarly covered regions.

d: gravity interpretation, magnetic interpretation, filtering, analytical downward continuation, Velence hills (Hungary)

1. Introduction

*1.1 Geological outline***

The Velence granite hills are situated at the centre of a region of about 1500 km^2, between Budapest and Lake Balaton. The Velence hills are strongly eroded, weathered, emerge from their surroundings by some 100 m only; from the W-NW they are bordered by the mainly Mesozoic—Carboniferous Bakony and Vértes Mts. and by the Buda hills (eastern part of the Transdanubian Central Range) *(Fig. 1)*. The Velence hills—Balatonfő region belongs to the SE flank of the Transdanubian Central Range, the region is divided into two geologically different parts by the structural zone across Polgárdi and Velence Lake. In the northern part the basement of the thick upper Permian-Mesozoic group of formations consists of Palaeozoic rocks, these appear on the surface and mainly under Neogene sediments. The formations embedded in the intricate nappe structures contain the most complete Palaeozoic series of the Transdanubian Central Range:

Ordovician	quartz phyllite;
Silurian	schist, foliated siltstone, foliated sandstone, lydite, metamorphized acidic volcanites;
Devonian	schist, foliated siltstone, crystalline limestone, diabase;
Lower Carboniferous	limestone, schist, foliated sandstone;
Upper Carboniferous	sandstone, conglomerate.

* Eötvös Loránd Geophysical Institute of Hungary, POB 35. Budapest, H—1440
** The geological outline was written by I. Horváth of the Hungarian Geological Survey, POB 106. Budapest, H—1442
Manuscript received: 8.7.1983

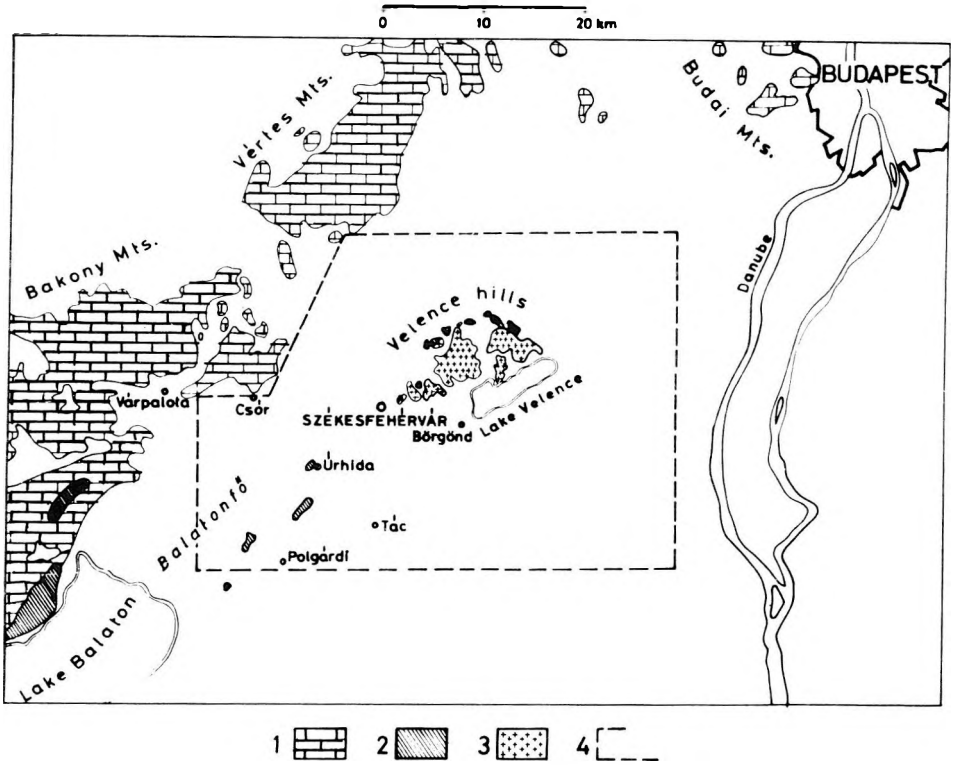

Fig. 1. Study site and the surrounding area
1 — Mesozoic carbonate rocks on the surface; 2 — different Palaeozoic metamorphic rocks on the surface; 3 — granite on the surface; 4 — the Velence hills study site

1. ábra. A kutatási terület és tágabb környezete
1 — mezozoos karbonátos kőzetek a felszínen; 2 — különböző paleozoos metamorf kőzetek a felszínen; 3 — gránit a felszínen; 4 — a Velencei-hegységi kutatási terület

Рис. 1. Район исследования и широкая окружность его
1 — мезозойские карбонатные породы выходят на дневную поверхность; 2 — различные палеозойские породы выходят на поверхность; 3 — гранит на поверхности; 4 — район исследования в горах Веленце

The Ordovician—lower Carboniferous formations evidently underwent epi- and anchimetamorphism. The upper Carboniferous formations of local extension are not metamorphic, the upper Carboniferous granite of the Velence hills, intruded into the Silurian—Devonian formations, has a postkinematic character. At the north-western part of the region the upper Permian red sandstone and the Triassic carbonate formation overlie the Palaeozoic rocks with angular unconformity.

South of the Polgárdi—Velence Lake line the oldest known formation is the lower Permian (?) quartz diorite found in a drilling. The upper Permian consists of predominantly lagunary—marine carbonate evaporitic formations, the Triassic consists of a carbonate formation of the Buda hills type.

In the northern part of the region, east and northwards from the Velence hills there appear upper Eocene sediments and andesitic volcanic formations, as well as Oligocene sediments. At the western side, southwards to Úrhida we also see andesitic tuff embeddings in the Eocene sedimentary series. In the southern part of the region Eocene andesitic subvolcanic bodies appear in the upper Permian—Triassic formations. Older Neogene rocks occur only in the north-western (Várpalota—Csór) and southern (Tác—Börgönd) part of the region. In the middle zone of the territory the Pannonian layers directly overlie the Palaeogene or older formation.

1. 2 Overview of the gravity and magnetic surveys

The first country-wide gravimeter survey of Hungary (of approx. 1 station/km^2 density) was completed in 1955. The new geological—geophysical explorations launched in 1976 were motivated mainly by the ore-prospectivity of the region and by the fact that a large part of the area has become a fashionable holiday resort where more thermal waters were needed [PINTÉR—SZABADVÁRY 1978].

Recognition of the regularities of the major structures is greatly facilitated by gravity and magnetic surveys. The detailing of the first reconnaissance gravity survey took place in 1976—78 resulting in the present-day 10 station/km^2 density net. The regional gravity anomalies are presented in *Fig. 2* and *Enclosure No 1*. Besides the gravity anomalies the regional magnetic ΔZ highs are also shown. The magnetic reconnaissance survey in 1951—55 revealed a magnetic anomaly of high intensity over a large area north-east of and south of Velence Lake, around the middle of the region *(Enclosure No. 2)*. The character of the anomalies suggests that in the Velence hills (and in their surroundings) several more extended anomalous bodies should be expected besides the high-susceptibility andesite dikes at some hundred metres depth [VASADY–KOVÁCS 1962].

2. Methodological considerations

2.1 Problems of depth estimation

As a first step in the quantitative interpretation of the gravity anomaly map we tried to establish a correlation between the depth values of the Mesozoic and Palaeozoic rocks known from drillings and the Bouguer anomaly values. In the case of a fair correlation the interpretation is quite straightforward and one can

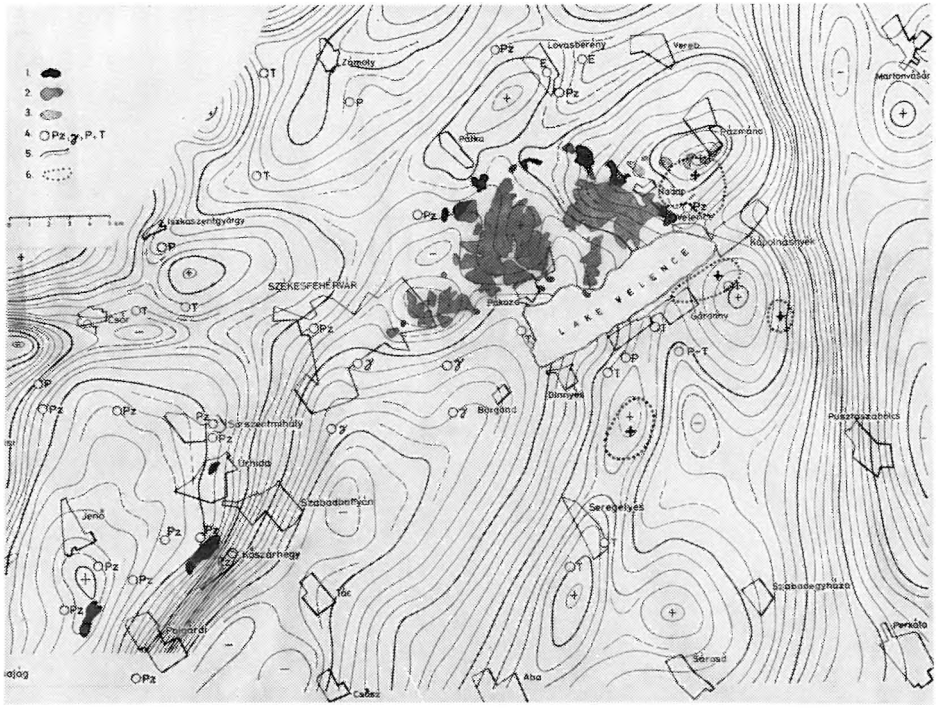

Fig. 2. The Velence hills study site with regional gravity and magnetic anomalies
1 — Palaeozoic rocks on the surface; 2 — granite on the surface; 3 — metasomatite (andesite) on the surface; 4 — basement formations hit by drillings: Palaeozoic in general (Pz), granite (γ), Permian (P), Triassic (T); 5 — regional gravity anomalies (isoline spacing 1 mgal); 6 — regional magnetic highs

2. ábra. A Velencei-hegységi kutatási terület a regionális gravitációs és földmágneses anomáliákkal
1 — paleozoikum a felszínen; 2 — gránit a felszínen; 3 — metaszomatit (andezit) a felszínen; 4 — mélyfúrásban elért paleozoikum általában (Pz), gránit (γ), perm (P), triász (T); 5 — regionális gravitációs anomáliák (értékköz 1 mgal); 6 — földmágneses ΔZ értékek regionális maximumai

Рис. 2. Район исследования в горах Веленце с региональными аномалиями силы тяжести и геомагнетизма
1 — палеозой на поверхности; 2 — гранит на поверхности; 3 — метасоматит (андезит) на поверхности; 4 — вскрытые в скважине палеозой (P), гранит (γ), перм (P), триас (T); 5 — региональные аномалии силы тяжести (сечение изолиний — 1 мгл); 6 — региональные максимумы геомагнитных значений

compute an approximate basement contour map from the Bouguer anomaly values [PINTÉR—STOMFAI 1974]. Such maps have frequently been computed from Bouguer anomaly- and filtered gravity maps for different regions of Hungary, and have proved to be useful for further exploration work. In the present case, however, we had to realize that the gravity anomalies do not correlate with any for the formation boundaries known from boreholes.

The surface of the older than Triassic formations varies between +220 m and −350 m, i.e. in a domain of 570 m, while for the same borehole locations the variation of the Bouguer anomalies is 23 mgal (1 mgal = 10^4 nms^{-2} = = 10^{-5} ms^{-2}). If we assume a large density contrast, say of the order of 0.5 10^3 kg/m^3, between basement and overburden, a 2 mgal gravity anomaly change would correspond to every 100 m change in depth. The 570 m depth change would imply a variation in the anomaly of only 11.4 mgal, i.e. only half of the observed 23 mgal can be due to the depth changes of the basement. The rest of the anomaly is thus independent of the thickness of the roughly homogeneous Neogene formations, i.e. of the depth changes of the older formations, and should have its cause somewhere deeper than the basement. Since we have failed to transform the gravity anomaly maps into depth contour maps, we tried to base our interpretation on an individual analysis of the anomalies appearing on the various filtered maps.

2.2 Low-cut filterings

The general aim of filtering is to separate and enchance the aniomalies that appear in the Bouguer anomaly map in an interwoven obscure form, in order to yield a more characteristic picture of the subsurface mass distribution. Of course, we cannot expect any single filter to produce all these required effects (discrimination, enhancement) over a relatively large, geologically complicated area. As is well known [SKEELS 1967], the choice of the filter has always been subjective. In Hungary, for example, the low- and high-cut filters defined by MESKÓ [1966, 1967] have been found fairly successful. These were the filters used for the present investigations, both for the gravity- and for the magnetic ΔZ maps, with a sampling rate of $s = 250$ m being a bit less than average station spacing (approx. 300 m).

The selection of the filter parameters (slope of the rejection, sampling rate) defines the character of the filtering. The steep rejection slope and a relatively low sampling rate as compared with the depth and the lateral extension of the anomalous body are advantageous for the production of second-derivative-like anomaly maps, a more gentle rejection slope and a greater sampling rate favour residual-anomaly-like maps [PINTÉR—STOMFAI 1979]. The highs and lows of the residual-anomaly-like maps can generally be brought into a fair qualitative connection with the topography of the smaller near-surface anomalous bodies. On the derivative-like maps the lows and highs refer to the edges of the anomalous bodies and they are only indirectly connected with the shape of the

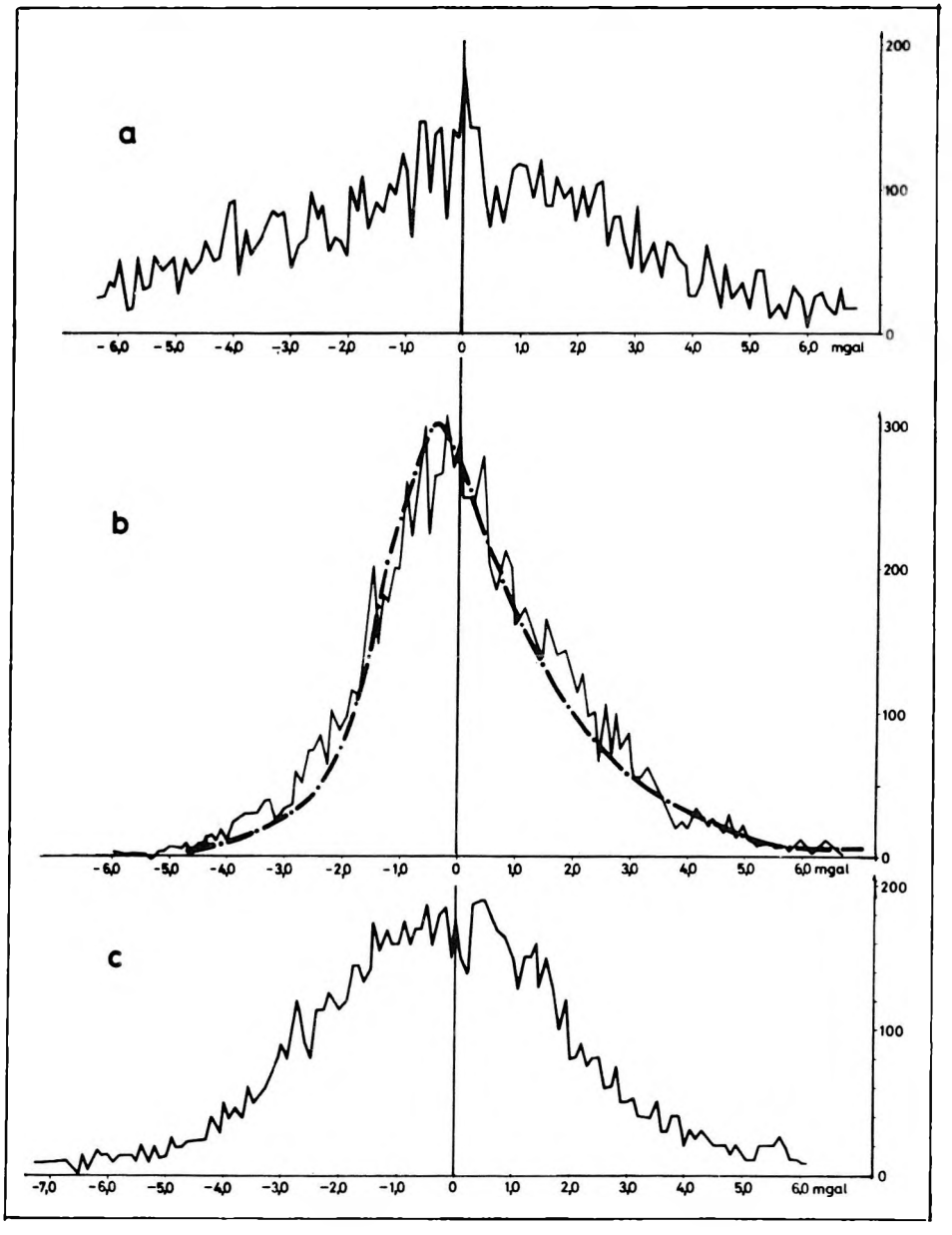
a
200
100
0
-6,0 -5,0 -4,0 -3,0 -2,0 -1,0 0 1,0 2,0 3,0 4,0 5,0 6,0 mgal
b
300
200
100
0
-6,0 -5,0 -4,0 -3,0 -2,0 -1,0 0 1,0 2,0 3,0 4,0 5,0 6,0 mgal
c
200
100
0
-7,0 -6,0 -5,0 -4,0 -3,0 -2,0 -1,0 0 1,0 2,0 3,0 4,0 5,0 6,0 mgal

anomalous bodies. Consequently, it is very important to recognize the character of the filtered map. The frequency histogram *(Fig. 3)* of the filtered anomalies, on the basis of 10,000 data, clearly shows the kind of map that should be expected as a result of filtering. If the filtered map has a residual-anomaly character, the anomalies will be more-or-less uniformly distributed without prominent parts in the frequency curve (Fig. 3, curve *a*). For derivative-like maps (Fig. 3, curbe *b*), the frequency curve shows a sharp maximum around the zero value. (The maximum of the frequency curves is a little bit shifted toward the negative values because the measured maxima are, as a rule, relatively larger than the measured minima.) The map of the study site filtered with a low-cut filter with an $s = 250$ m sampling rate *(Enclosure No. 3.)* is rather derivative-like according to curve *c* of Fig. 3, consequently the zero-line of the map should be considered—with some restrictions—as a distinguished value from the point of view of geological interpretation. The filtered gravity maps were computed from the Bouguer anomaly map corrected with an average density of $\sigma = 2.0\ 10^3$ kg/m^3. This average density fairly well corresponds all over Hungary to the mean density of the surface- and near-surface Neogene (sandy, clayey) formations. In the area of the Velence granite hills, however, the surface density is much higher: $\sigma = 2.65\ 10^3$ kg/m^3. Therefore, for the area of the hills, we computed another map of low-cut filtering based on the Bouguer anomaly map corrected by $\sigma = 2.65\ 10^3$ kg/m^3 average density *(Enclosure No. 4)*.

Fig. 3. Frequency distribution curves of filtered anomalies (computed from 10,000 data)
a) Frequency distribution for a residual anomaly-like map obtained by a filter of parameters $s = 250$ m, $\kappa = 4$;
b) Frequency distribution for a (second) vertical-derivative-like map obtained by a filter of parameters $s = 250$ m, $\kappa = 4$. The result-line represents the mean of several derivative-like maps from different regions;
c) Frequency distribution for a map of transient nature obtained by a filter of parameters $s = 250$ m; $\kappa = 4$. The map is characteristic to the surrounding area of the Velence hills

3. ábra. Szűrt anomáliák gyakorisági görbéi (10 000 adatra vonatkoztatva)
a) Az $s = 250$ m, $\kappa = 4$ paraméterű szűrővel készült maradék-anomália jellegű térkép gyakorisági görbéje;
b) Az $s = 250$ m, $\kappa = 4$ paraméterű szűréssel készült (második) vertikális derivált jellegű térkép gyakorisági görbéje. Az eredményvonal számos különböző terület derivált jellegű térképének átlagát jelzi;
c) Az $s = 250$ m, $\kappa = 4$ paraméterű szűrővel készült átmeneti jellegű térkép gyakorisági görbéje. A Velencei-hegység tágabb környezetére ez utóbbi jellemző

Рис. 3. Кривые частоты фильтрованных аномалий (по 10000 данным)
a) кривая частоты для карты типа остаточной аномалии, построенной с фильтром параметрами $s = 250$ м, $\kappa = 4$;
b) кривая частоты для карты характера вертикального производного, построенной с фильтром параметрами $s = 250$ м, $\kappa = 4$. Штрихпунктиром показана средняя для карт характера производного по ряду различных районов;
c) кривая частоты для карты переходного характера, построенной с фильтром параметрами $s = 250$ м, $\kappa = 4$. Эта карта является типичной для широкой окружности гор Веленце

2.3 Downward continuation

Due to the extreme complexity of the territory, in addition to the low-cut and high-cut filter matrices we have also experimented with filter matrices realizing analytical downward continuation to the depths $h = s$ and $h = 2s$, respectively [MESKÓ 1973] (*Enclosure No. 5*). Since we have not too much experience with analytical downward continuation, we carried out a few experiments to study the resulting filter matrices. Downward continuation matrices with different parameters were utilized, and in each case the downward continuation was carried out to several levels. The results can conveniently be compared along a profile (*Enclosure No. 5*). The basic result of this comparison, is that even though the different downward continuation matrices indicate the anomalies referring to the edges of the anomalous bodies at the same horizontal locations, they cannot be used for vertical resolution, i.e. to estimate the depth of the anomalous bodies. In the further investigations from among the downward continuation matrices only the fourth one from above has been used because of technical considerations (loss of areas at the edges of the map, representability of the anomalies).

Since the low-cut filter applied to the Bouguer anomaly map did not always enhance the smaller anomalies; the downward-continued maps were also processed by low-cut filters. From the considerable amount of different map versions only those will be dealt with which have — at least at some places — contributed to the interpretation by revealing some significant anomalies. The first downward continued map (*Enclosure No. 6*) is similar to the Bouguer anomaly map but contains much more details. The low-cut filtered version of this map was smoothed by high-cut filtering; that is, the map was band-pass filtered (*Enclosure No. 7*). The second (repeated) downward continuation further emphasizes the small-sized weaker anomalies in the deeper parts of the basin (*Enclosure No. 8*).

2.4 High-cut filterings

In order to study the large-size regional anomalous bodies we computed a regional anomaly map by high-cut filtering the Bouguer anomaly map, and superimposed on this map the regional magnetic ΔZ maxima (*Enclosure No. 1*). It should be noted that a high-cut filtering is generally nothing but a smoothing: the anomaly picture of even the simplest body is always divided by any low-cut or high-cut filter into a so-called residual and a so-called regional map. Consequently, the anomalies appearing in the regional map do not always correspond to some definite, deep (regional) anomalous body. In the attached map we cannot state with certainty whether anomalous high-density deep bodies are present unless the regional gravity anomalies coincide with regional magnetic anomalies, since generally these high-density bodies should also have high susceptibility values.

2.5. Magnetic residual anomalies

The magnetic residual anomalies (*Enclosure No. 9*) were computed only for such parts of the area where the average spacing of the points of measurement did not exceed 300 m. (The ΔZ measurements had been carried out over only about half of the Velence Lake.)

In the interpretation of magnetic maps it should be kept in mind that judging from the sporadic surface palaeomagnetic data the rocks have a significant remanent magnetization and its direction is frequently different from (or even opposite to) the induced magnetization. Sometimes the two kinds of magnetization cancel each other so that no measurable anomaly remains in spite of the high susceptibility of the rock. At certain places the remanent magnetization could even dominate, leading to a high-intensity negative anomaly. All the facts and measured data holding for the surface rocks should also hold for the deeper anomalous bodies so that any model calculations starting out solely from induced magnetization should be accepted with reservations; as a matter of fact we have been reluctant to do such computations. Except for a few small-sized andesite dikes on the area of the Velence hills, in the magnetic anomaly map of the area eastwards and southwards from the hills positive anomalies dominate. This implies that in the deep anomalous bodies, positive magnetization is dominant as the net vectorial resultant of the induced and remanent magnetizations. This fact should be utilized in the comparison with gravity anomalies. If the gravity and magnetic anomalies are possibly due to the same rock (body) then the magnetic highs should appear as shifted in the S, SE and SW directions, from the corresponding gravity highs, the magnitude of this shift being dependent on body size and on the exact direction of the magnetization [MADARASI et al. 1981].

2.6 Connection between magnetic and gravity anomalies

If we wish to pursue the connections between magnetic and gravity anomalies, it has to be assumed that the bodies causing magnetic anomalies have a smaller (greater) density than their surroundings and, consequently, they cause a local gravity minimum (maximum). As described above, the magnetic anomalies should be shifted by a certain amount N—NW—NE-wards until they coincide with either a gravity high or a gravity low [CSÖRGEI et al. 1982]. This shift, of course, is not unambiguous. If we assume that the magnetically anomalous bodies have a slightly smaller density than their immediate vicinity, i.e. they appear with local gravity lows, then after a relatively small shift in the N—NE (possibly also NW) direction the ΔZ residual anomalies would coincide with the minima of the downward continued gravity map. It should be noted that the direction and the magnitude of the shift tend to be uniform within individual clusters of anomalies. On the other hand, if we attribute the magnetic anomalies to rocks of higher density, then the magnetic highs should coincide

with gravity highs. This seems to be the case for the downward continued, band-pass filtered gravity residual anomaly map; as a matter of fact the coincidence becomes even better than before, though this is at the expense of larger shifts. It should be noted that the ΔZ maxima must be shifted in both cases to a greater extent than would have been implied by induced magnetism, and by the assumed 1000—1500 m depth of the anomalous body. This either refers to a larger depth of the anomalous body or to a remanent magnetization which strongly influences the direction of the induced magnetism. On the other hand, the concidence of the regional magnetic and regional gravity anomalies around Pázmánd and Dinnyés is very characteristic. Besides the strikingly similar shapes of the anomalies the regional magnetic high appears in both cases as shifted southwards from the gravity high. This implies that the deep anomalous bodies have a dominantly induced magnetism. Unfortunately, the amount of the shift cannot be used to infer the exact depth of the bodies for we do not know the direction of their eventual remanent magnetization or the exact location of the extremal values of these bodies. The extension (lateral dimensions) of the high-density, high-susceptibility body cannot accurately be delineated — all we have is subjective guesswork.

The occurence of such uncertainties (hypotheses) in the preliminary stage of exploration is almost inevitable. For a better understanding of the interconnection between gravity and magnetic anomalies more detailed measurements should be carried out over both kinds of anomalies in order to locate exactly the extremal points. (In this case, by a proper transformation of the gravity maps we could even prepare a pseudo-magnetic map that would be suitable for pointing out the actual coincidences with magnetic anomalies.)

2.7 Gravitational model computation

In the interpretation of the gravity anomalies important conclusions can be drawn from some simple model computations — even on a small pocket calculator. A simple result is shown in *Fig. 4*. It can be seen that usually the place of largest variation (the zero of the derivative of the anomaly) shows the location of the fault. Also, observe that the anomaly picture will become different if we interchange the position of the denser and the less dense rocks along the fault (Fig. 4, curve 3 *c* compared to 3 *a*). In nature, it is a much more frequently encountered situation that next to a very large residual gravity anomaly high we encounter a much weaker residual anomaly low (curve *a*). In such cases it is characteristic of the maximum—minimum transition that a more rapid change occurs near the maximum. However, on the nearly derivative-like filtered maps of the study site we sometime see relatively small maxima together with minima of very large magnitude. In such cases there is a high gradient near the minimum. This suggests a geological situation that could correspond to the model belonging to curve *c* of Fig. 4. (According to curve *c* of Fig. 4, the considerations concerning the derivative-like curves may be taken as approximately valid for our study site.)

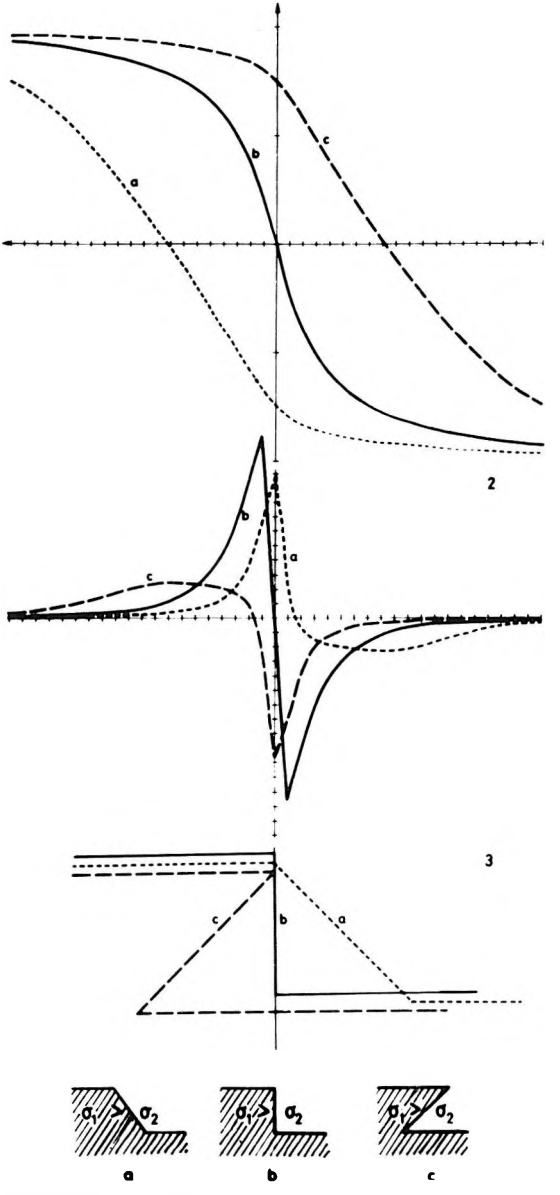

Fig. 4. Shape of Bouguer- (1) and vertical derivative (2) anomalies as function of the dip of the fault (3)

4. ábra. A Bouguer- (1) és a vertikális derivált (2) anomáliák alakja a vető dőlésszögének (3) függvényében

Рис. 4. Форма аномалий Бугэ и вертикальных производных в зависимости от угла наклона сбросов

2.8 Construction of isolines of the gravity maps

In the construction of the isolines of gravity maps — for convenience' sake — one generally connects by isolines those points which have the same integer mgal values (as, for example, e.g. 10, 11, 12 mgal), or the same half, quarter, tenth etc. mgal values (e.g. 0.25, 0.50, 0.75 mgal). This, however, is certainly not always optimal since it might occur that the anomaly would appear with a more characteristic shape for another set of isolines.

If we use a computer where a series of maps can be constructed for the different values of isolines, we might find that the shape of the anomaly is the most accurately inferred from a mosaic-like composite of the different map versions.

3. Geological conclusions

On the basis of the previously described methodological considerations we have sought for the following characteristic features on the maps:

a) are there any parallel anomaly lines that do not change their directions over longer sections (the zero lines on the residual anomaly maps)? These lines, in fact signify the approximate location of structural elements associated with density changes (faults, uplifts);

b) do we recognize characteristic (circular, elongated, annular, etc.) anomaly shapes from which we can conclude to the form and, indirectly, to the nature of the anomalous body?

c) do we see characteristic maximum—minimum transitions or minima with extremely large magnitude which reflect the mass distribution along the structural lines?

d) are there any observable orientation patterns extending over larger areas; do they change from subregion to subregion? The analysis of these patterns bears possible information on the interior structure of the basement;

e) is there any connection between magnetic and gravity anomalies, i.e. are the gravity anomalies associated with high-susceptibility volcanic rocks?

f) is there any connection between the high-density surface rocks (known from the geologic map) and the anomalies measured in their vicinity; that is, is it possible to follow the surface outcrops on the covered parts?

We attached specially selected keys to the characteristic gravity and magnetic anomalies that express their nature and at the same time refer to their possible geological meaning (*Fig. 5* and *Enclosure No. 10*, respectively). The sketch map of the results also shows the most characteristic anomaly-directions of the region, on the basis of the zero lines of the low-cut filtered anomaly maps. A part of the zero lines approximately coincide on the different maps (smaller deviations might be due to errors in rounding-off or due to the construction). Line segments that coincide on two or three maps are denoted by *solid lines*. We think that such lines occur at places where there is such a high density contrast

that it suppresses the effect of the secondary (transversal or otherwise directed) density changes. At the two sides of these lines the signs show whether the positive or the negative anomaly has the greater maximum along the zero line. (We refer once more to Fig. 4, where it is clearly seen that the zero lines are shifted depending on the nature of the structural element. The zero line runs exactly over the fault only in the case of a vertical fault.) *Thinner lines* denote those zero lines which appear on only one of the maps but either constitute a continuation of the solid lines or show a characteristic orientation within a certain subregion.

The map also calls attention to the characteristic gravity anomaly shapes, it also indicates whether they are connected to geomagnetic anomalies; characteristic magnetic residual anomalies that are not associated with gravity anomalies are also displayed. Where we have succeeded in interpreting the gravity highs as actual geological formations on the basis of borehole data or outcrops, this is duly indicated on the map.

On the basis of the characteristic features of the gravity anomalies listed above the following structural elements can be delineated in the Velence hills and in the surrounding area (these structural elements are associated with density changes at larger depths) (see Fig. 5, or Enclosure No. 10).

Anomalies referring to the structural elements of the Velence hills

The granite pluton of the Velence hills is surrounded by the semicircular minimum-zone of approx. 1 km width of the residual anomalies (*Enclosure No. 4*). This minimum zone is bounded north and north-westwards by several positive residual gravity anomalies. These partly lie in the areas of Palaeozoic schist outcrops which are older than the granite, so that is seems evident to interpret the residual anomaly highs as buried continuations of the schists. The minimum-zone is then interpreted as the tectonic contact zone between the granite and the older palaeozoic formation. The granite pluton itself is divided by several radial fractures (residual gravity anomaly lows) into roughly three parts. The Velence hills are bounded from the SE by a NE-SW-directed structural element (fault, transcurrent fault, parallel with the strike of Velence lake). This element is the most clearly recognized in the gravity anomaly map of Enclosures Nos. 3 and 6.

Anomalies referring to buried volcanic formations

On the basis of the characteristic circular or annular shape of the residual gravity anomalies, and according to the distribution of the magnetic residual anomalies, three deep volcanic formations can be assumed, viz. east from the Velence hills and south and east from the Velence lake, respectively (Enclosures Nos. 3, 6, 8 and 9). In two cases the coincidence of the regional gravity and

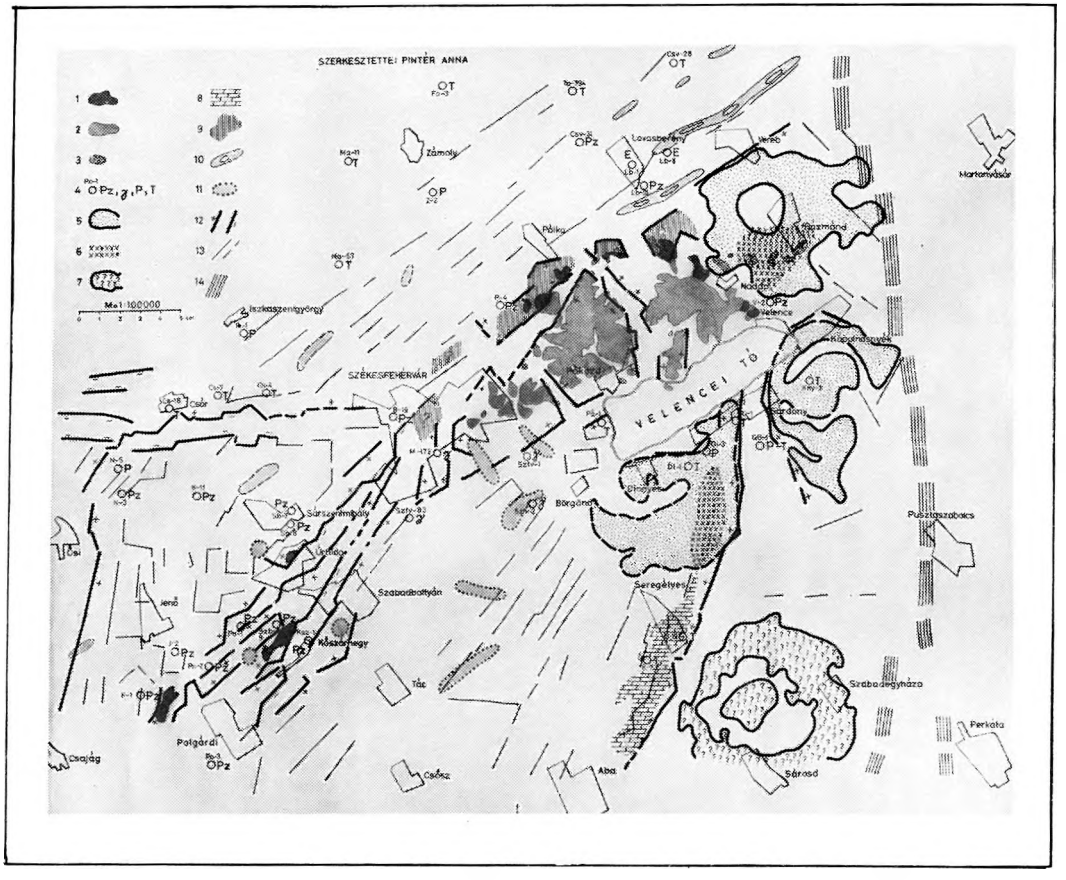

Fig. 5. Sketch map of results: geological interpretation of the gravity- and magnetic anomalies 1 — Palaeozoic rocks on the surface; 2 — granite on the surface; 3 — metasomatite (andesite) on the surface; 4 — basement formations hit by drillings: Palaeozoic in general (Pz), granite (γ), Permian (P), Triassic (T); 5 — characteristic circular residual gravity anomaly containing a dense cluster of residual magnetic anomalies in its interior: assumed deep volcanic formation; 6 — coincidence of regional gravity- and magnetic anomalies: diorite intrusion; 7 — characteristic annular gravity anomaly: unknown formation; 8 — elongated, narrow residual gravity anomaly: assumed extension of the dolomite known from the Seregélyes drillings; 9 — gravity high appearing as continuation of the Palaeozoic schist outcrops surrounding the granite pluton: deep continuation of the Palaeozoic schist; 10 — elongated residual magnetic anomaly: anomalous magnetic body connected with the directions appearing on the gravity maps; 11 — magnetic anomaly connected neither to known or assumed volcanic formations, nor to structural lines: anomalous body, possibly related to local Eocene volcanism; 12 — persistent zero line separating positive and negative residual anomalies, of high values (the sign of the larger anomaly being indicated): fault or upthrust appearing with density contrast; 13 — zero line separating positive and negative residual anomalies of low values, or not traceable over larger distances: density changes presumably related to interior basement structure; 14 — characteristic high-gradient zone: presumed deep fault

5. ábra. A gravitációs és földmágneses anomáliák földtani értelmezése
1 — paleozoikum a felszínen; 2 — gránit a felszínen; 3 — metaszomatit a felszínen; 4 — fúrásban elért paleozoikum általában (Pz), gránit (γ), perm (P) és triász (T) képződmény; 5 — jellegzetes kör alakú gravitációs maradék-anomália, amelynek területén a földmágneses maradék-anomáliák sűrűsödnek: föltételezett mélybeli vulkáni képződmény; 6 — a regionális gravitációs és földmágneses anomáliák egybeesése: diorit intruzió; 7 — jellegzetes gyűrű alakú gravitációs anomália: ismeretlen képződmény; 8 — hosszan elnyúlt, keskeny gravitációs maradék-anomália: a seregélyesi fúrásokból ismert dolomit feltételezett elterjedése; 9 — a gránitplutont övező felszíni paleozoos palakibúvások folytatásaként látható gravitációs maximum: a paleozoos pala mélybeli folytatása; 10 — hosszan elnyúlt mágneses maradék-anomália: a gravitációs térképekben jelentkező irányokhoz kapcsolódó földmágneses ható; 11 — az ismert (ill. feltételezett) vulkáni képződményekhez nem tartozó és nem szerkezeti vonalhoz kapcsolódó földmágneses anomália: föltételezhetően lokális eocén vulkanizmussal kapcsolatos ható; 12 — viszonylag nagy anomália-különbséggel jelentkező pozitív és negatív maradék-anomáliát elválasztó, hosszan nyomozható zérus vonal, a relative nagyobb anomáliaérték előjelének föltüntetésével: sűrűségkülönbséggel jelentkező vető vagy feltolódás; 13 — kisebb anomália-különbségű pozitív és negatív maradék-anomáliákat elválasztó,vagy rövidebb szakaszon nyomozható zérus vonal: feltételezhetően az aljzat belső szerkezetével összefüggő sűrűségváltozás; 14 — izovonal-sűrűsödéssel (nagy gradiensekkel) jelentkező széles zóna: föltételezhető mélybeli törés

Рис. 5. Геологическая интерпретация аномалий силы тяжести и геомагнетизма
1 — палеозой на поверхности; 2 — гранит на поверхности; 3 — метасоматит (андезит) на поверхности; 4 — вскрытые в скважине палеозой (Pz), гранит (γ), перм (P) и триас (T); 5 — характерная остаточная аномалия силы тяжести в форме круга: предположенная вулканическая формация на глубине; 6 — совпадение региональных гравиметрических и магнитных аномалий: диоритовая интрузия; 7 — характерная кольцообразная аномалия силы тяжести: неизвестная формация; 8 — узкая, продленная остаточная аномалия силы тяжести: предполагаемое распространение доломита, известного по скважине ок. с. Шерегейеш; 9 — гравитационный максимум в продолжении выходов палеозойских сланцев вокруг гранитового плутона: продолжение палеозойских сланцев на глубине; 10 — длинная остаточная геомагнитная аномалия: магнитное тело, приуроченное к проявленным на гравиметрических картах направлениям; 11 — геомагнитная аномалия, не принадлежащая к известной, или к предположенной вулканической формации, и неприуроченная к структурной линии: предполагаемое тело, связанное с местным зоценовым вулканизмом; 12 — продолжительно прослеживаемая нулевая линия, разделяющая положительные и отрицательные остаточные аномалии, с указанием знака относительно высокого значения аномалии: сброс или надвиг, проявляющиеся с расхождением плотности; 13 — нулевая линия, прослеживаемая на коротком участке, или разделяющая положительные и отрицательные остаточные аномалии с небольшой разностью аномалий: предполагаемое изменение плотности, связанное с внутренней структурой фундамента; 14 — широкая зона с угущением изолиний (большими градиентами): предполагаемый глубинный разлом

regional magnetic anomalies and their similar shape (Fig. 2, Enclosure No. 1) refer to a deep intrusion of high density and susceptibility (Pázmánd, Dinnyés). In the case of the third annular gravity anomaly (Kápolnásnyék) even though we can detect smaller magnetic anomalies, their coincidence with the gravity anomalies is not convincing. Probably we are dealing with a strongly eroded, deep volcanic formation.

Evidence of unknown anomalous bodies

The annular formation at the south-eastern corner (Sárosd) of the sketch map of results (Fig. 5, Enclosure No. 10; see also the residual anomaly on Enclosure No. 7) is due to an unknown anomalous body. The existence of greater magnetic anomalies can surely be excluded, smaller anomalies cannot be ascertained with the currently available detail of the geophysical survey.

Anomalies showing the extension of the Seregélyes Triassic dolomite horst

Between the above-mentioned deep unknown formation and the buried volcano at Dinnyés there appears in all gravity maps (see e.g. Enclosure No. 8) a long, narrow gravity maximum of NNE strike and about 10 km length. At this location the drillings hit Triassic dolomite (Seregélyes). The asymmetrical Triassic dolomite horst of elevated position can clearly be delineated by means of the gravity map.

Anomalies referring to a deep fault

The dolomite horst of Seregélyes and the east flank of the buried volcano of Dinnyés are bounded by characteristic anomalies in all gravity maps, suggesting faults. The fault starts in a N—S direction from Velence lake, then assumes a NNE—SSW direction along the Seregélyes dolomite horst. The density of the isolines representing the fault, i.e. the magnitude of the gradient, depends on the depth of the fault as well as on the density constrast across the fault. For the fault in question, the Micoene formation overlying the downthrown part is adjacent in the north to the Eocene volcanic material of relatively smaller density, in the south to the Triassic dolomite having a greater density contrast. Consequently, in the south (Seregélyes), the gardient is somewhat larger.

Anomalies referring to multiple faults and upthrusts

Starting out from the SW corner of the sketch map of results there appears an intricate system of anomalies of roughly NE strike on all gravity maps, suggesting faults and upthrusts (Enclosures Nos. 3, 6, 7 and 8). The present-day details (10—12 stations/km^2) of the survey, however, are insufficient for their more accurate mapping.

Along this intricate structure the shallow-depth Palaeozoic block (Csaják—Jenő—Sárszentmihály—Úrhida—Kőszárhegy) of complex lithologic development, known from outcrops and drillings, abruptly terminates upon contacting the Neogene basin of unknown basement.

Minimum zones referring to upthrusts

The northern rim of the above-mentioned Palaeozoic block is terminated by an EW-directed zone appearing with a gravity low of extremely large magnitude, the zone can further be followed a long way beyond the western boundary of the map. Since this relatively narrow and long minimum zone with such an extreme magnitude is practically unrivalled in Hungary, its geologic interpretation deserves special attention. A section of this minimum zone west of Csór has proved to be a multiple upthrust according to drillings and geologic studies [KÓKAY 1968]. The repetition of minimum zones also suggests that we are facing a multiple upthrust. It is thought that the other part of the minimum zone, east of Csór, should similarly be interpreted as a zone of upthrust.

Anomalies referring to basement structure

North and westwards of the Velence hills there appear characteristically NE—SW-oriented residual gravity anomalies of relatively small amplitude. North of the buried volcano of Pázmánd the elongated magnetic residual anomaly highs (Enclosure No. 9) follow the same direction. Consequently, we have to expect that the basement also contains structural elements of this direction, with the associated magmatic formations (according to the drillings: diabase) following their direction.

South-westwards of Velence lake (between the asymmetrical Seregélyes horst and the Palaeozoic block at the western side of the map) the gravity anomalies also reveal a characteristic orientation. The roughly NNE-directed anomalies are parallel with the fault bounding from the east the Seregélyes dolomite horst. The interior structure of the western Palaeozoic block is displayed by the predominantly NS- and EW-oriented gravity anomalies. According to the regional gravity anomaly map (Fig. 2, Enclosure No. 1), the gravity anomalies decrease uniformly in the westward direction, from the Seregélyes dolomite horst towards the minimum between Tác and Börgönd. This gravity "slope" — according to the few available drillings and the preliminary interpretation of seismic surveys — cannot be attributed to a gradual sinking of the Palaeozoic—Mesozoic basin floor, the change of about 15 mgal is rather thought as due to density changes within the basement.

Anomalies referring to deep faults bounding the region from the east

The Bouguer anomaly map (not included), the regional- and downward continued maps contain a characteristic high-gradient zone of N—S direction near to the eastern boundary of the area. This zone of about 40 km length appears on the residual anomaly maps with zero lines. These phenomena refer to a deep fault system (see e.g. Enclosures Nos. 1 and 8). Along this fault the basin deepens in the eastern direction, the Palaeogene and Miocene formations

become thicker. All the other geophysical methods have failed, to date, in detecting this assumed fault system.

*

The geological interpretation of the above-listed characteristic anomalies is, of course, of varying reliability. This is due to a number of facts: to the non-uniformity of the gravity and magnetic network, to their eventual sparseness in some places as compared with the depth and small size of the anomalous bodies, to the capriciously varying density contrast between these bodies and their surroundings and, lastly, to the absence of drillings — especially in the eastern and southern part of the area. The sketch map of results merely summarizes those structural elements which appear with varying degrees of reliability, in order to ease the orientation between the regions of different gravity and magnetic maps.

It is hoped that this map will be of use towards some later, integrated interpretation. It is also to be hoped that we have been able to convince others that — having some borehole data — a thorough, many-sided study of the gravity and magnetic anomalies alone significantly contributes to our understanding of the deep structures, even under the most complex geological conditions.

REFERENCES

Csörgei J., Madarasi A., Majkuth T., Márton E., Pintér A., Schönviszky L., Varga G. 1982: The regional exploration of the Velence hills. Annual Report of the Eötvös Loránd Geophysical Institute of Hungary for 1981, pp. 21—28

Dudko A., Madarasi A., Majkuth T., Pintér A., Csörgei J., Schönviszky L. 1982: Complex geophysical exploration and perspectives of an Eocene volcanic region in the Velence hills (in Russian). 27th International Geophysical Symposium, Bratislava, Czechoslovakia, 7—10 September 1982, Proceedings A, pp. 425—442

Kókay J. 1968: Theories of orogenesis confronted with Bakony Mts data (in Hungarian). Földtani Közlöny, **98,** 3—4, pp. 381—391

Madarasi A., Majkuth T., Pintér A., Verő L. 1981: The regional exploration of the Velence hills. Annual Report of the Eötvös Loránd Geophysical Institute of Hungary for 1980, pp. 27—34

Meskó A. 1966: Gravity Interpretation and Information Theory II. Smoothing and Computation of Regionals. Annales Universitatis Scientiarum Budapestinensis de Rolando Eötvös Nominatae, Sectio Geologica **10,** pp. 15—27

Meskó A. 1967: Gravity Interpretation and Information Theory III. The Method of Second Derivatives. Annales Universitatis Scientiarum Budapestinensis de Rolando Eötvös Nominatae, Sectio Geologica **11,** pp. 37—60

Meskó A. 1973: A modelling study of the detectability of density surfaces. The gravity inverse problem and the method of analytical downward continuation (in Hungarian). Manuscript, OKGT Archives Budapest

Pintér A., Stomfai R. 1974: Experiment for the determination of the local matrix transforming the Bouguer anomaly map into a depth contour map (in Hungarian). Magyar Geofizika, **15,** 5—6, pp. 169—174

Pintér A., Stomfai R. 1979: Gravitational model calculations. Geophysical Transactions, **25,** pp. 5—31

Pintér A., Szabadváry L. 1978: On the reconnaissance geophysical survey in the Velence hills and their surroundings (in Hungarian). ELGI Report, Budapest

SKEELS D. C. 1967: What is Residual Gravity? Geophysics, **32,** 5, pp. 872—875
VASADY-KOVÁCS F. 1962: Geological and geophysical researches in the Velence hills (in Hungarian). Geophysical Transactions, **11,** 1—4, pp. 119—151

Legends for the Enclosures (in microfiche)

Enclosure No. 1. Velence hills study site with regional gravity and magnetic anomalies
1 — Palaeozoic rocks on the surface; 2 — granite on the surface; 3 — metasomatite (andesite) on the surface; 4 — basement formations hit by drillings: Palaeozoic in general (Pz), granite (γ), Permian (P), Triassic (T); 5 — regional gravity anomalies (isoline spacing 1 mgal); 6 — regional magnetic highs

Enclosure No. 2. Reconnaissance magnetic (ΔZ) anomaly map for the Velence hills and the surrounding arc (isoline spacing 10 nT)

Enclosure No. 3. Residual anomaly map for the Velence hills and the surrounding area. $\sigma = 2.0\ 10^3$ kg/m^3, $s = 250$ m, $\kappa = 4$

Enclosure No. 4. Residual anomaly map for the Velence hills. $\sigma = 2.65\ 10^3$ kg/m^3, $s = 250$ m, $\kappa = 4$, 1 — granite on the surface; 2 — Palaeozoic rocks on the surface

Enclosure No. 5. Quarter-matrices of the downward continuation corresponding to different parameters, and application of these matrices along the same profile

Enclosure No. 6. Downward-continued map of the Velence hills and the surrounding area

Enclosure No. 7. Downward-continued and subsequently band-pass-filtered residual anomaly map of the Velence hills and the surrounding area

Enclosure No. 8. Twice downward-continued map of the Velence-hills and the surrounding area

Enclosure No. 9. Magnetic ΔZ residual anomalies of the area surrounding the Velence-hills

Enclosure No. 10. Sketch map of results: geological interpretation of the gravity- and magnetic anomalies
1 — Palaeozoic rocks on the surface; 2 — granite on the surface; 3 — metasomatite (andesite) on the surface; 4 — basement formations hit by drillings: Palaeozoic in general (Pz), granite (γ), Permian (P), Triassic (T); 5 — characteristic circular residual gravity anomaly containing a dense cluster of residual magnetic anomalies in its interior: assumed deep volcanic formation; 6 — coincidence of regional gravity- and magnetic anomalies: diorite intrusion; 7 — characteristic annular gravity anomaly: unknown formation; 8 — elongated, narrow residual gravity anomaly: assumed extension of the dolomite known from the Seregélyes drillings; 9 — gravity high appearing as continuation of the Palaeozoic schist outcrops surroundings the granite pluton: deep continuation of the Palaeozoic schist; 10 — elongated residual magnetic anomaly: anomalous magnetic body connected with the directions appearing on the gravity maps; 11 — magnetic anomaly connected neither to known or assumed volcanic formations, nor to structural lines: anomalous body, possibly related to local Eocene volcanism; 12 — persistent zero line separating positive and negative residual anomalies, of high values (the sign of the larger anomaly being indicated): fault or upthrust appearing with density contrast; 13 — zero line separating positive and negative residual anomalies of low values, or not traceable over larger distances: density changes presumably related to interior basement structure; 14 — characteristic high-gradient zone: presumed deep fault

GRAVITÁCIÓS ÉS FÖLDMÁGNESES ANOMÁLIÁK ÉRTELMEZÉSE BONYOLULT TEKTONIKÁJÚ TERÜLETEN (VELENCEI-HEGYSÉG)

PINTÉR Anna

A Velencei-hegység tágabb környezete pannóniai összlettel fedett síkság. A viszonylag kevés mélyfúrási adat nem elegendő a mélyszerkezet megismeréséhez. A szerző kísérletet tett különböző gravitációs és földmágneses térképváltozatokból a legfontosabb mélybeli szerkezeti elemek lehatárolására. Az összefoglaló térkép a további geofizikai- és fúrásos kutatást hivatott elősegíteni, a gravitációs és földmágneses módszertani megfontolások pedig hasznosak lehetnek a hasonló fedett területek gravitációs és földmágneses anomáliáinak értelmezésénél.

1. Bevezetés

*1.1 Földtani áttekintés**

A Budapest és a Balaton közötti, kb. 1500 km² nagyságú terület közepén levő, erősen lepusztult, mállott, környezetéből mindössze kb. 100 m-re kiemelkedő Velencei gránithegységet NyÉny-ról a túlnyomóan mezoos—karbonátos képződményekből fölépített Bakony, Vértes és a Budai-hegyvonulat (a Dunántúli-középhegység K-i része) határolja *(1. ábra)*. A Dunántúli-középhegység DK-i szárnyához tartozik a Velencei-hegység—balatonfői terület, amelyet a Polgárdi—Velencei-tó vonalában húzódó szerkezeti zóna két eltérő földtani felépítésű részre oszt.

Az É-i részen a felszínen és a túlnyomóan neogén üledékek alatt megjelenő paleozoos képződmények alkotják a középhegységi nagy vastagságú felső perm—mezozoos képződménycsoport aljzatát. A bonyolult, gyűrt, pikkelyes—takarós szerkezetekben települő összletben a Dunántúli-középhegység legteljesebb paleozoos rétegsora mutatható ki:

ordovicium	kvarcfillit;
szilur	agyagpala, aleurolitpala, homokkőpala, lidit, átalakult savanyú vulkanitok;
devon	agyagpala, aleurolitpala, kristályos mészkő, diabáz;
alsó karbon	mészkő, agyagpala, homokkőpala;
felső karbon	homokkő, konglomerátum.

Az ordovicium—alsó karbon összlet képződményei epi- és anchimetamorfózist szenvedtek. Nem metamorfok a lokális elterjedésű felső karbon képződmények és posztkinetikus jellegű a szilur-devon összletbe nyomult felső karbon velencei-hegységi gránit. A terület ÉNy-i részén felső perm vörös homokkő és triász karbonátos összlet szögkordanciával települ a paleozoikumra.

A Polgárdi—Velencei-tó vonalától D-re az ismert legidősebb képződ-

* A földtani áttekintést Horváth István (MÁFI) állította össze

mény egy fúrásban feltárt alsó perm (?) kvarcdiorit. A felső perm uralkodóan lagúnás-tengeri kifejlődésű karbonátos, evaporitos képződményekből áll, a triászt Budai-hegység típusú karbonátos összlet alkotja.

Az É-i területrészen a Velencei-hegységtől K-re és É-ra jelennek meg a felső eocén üledékek és andezites összetételű vulkáni képződmények, valamint az oligocén üledékek.

Nyugaton Úrhida D-i részén is ismeretes eocén üledékes rétegsor andezittufa betelepüléssel.

A D-i területrészen az eocén andezites szubvulkáni testek a felső perm—triász képződményekben települnek.

Idősebb neogén csak a terület ÉNy-i (Várpalota—Csór) és D-i (Tác—Börgönd) részén található.

A terület középső zónájában közvetlenül pannóniai rétegek települnek a paleogén- vagy idősebb képződményekre.

1.2 A gravitációs és a földmágneses kutatások áttekintése

A terület országos áttekintő (kb. 1 állomás/km² pontsűrűségű) graviméteres felmérése 1955-ben készült el. Az 1976-ban meginduló újabb földtani—geofizikai kutatásokat elsősorban a terület ércperspektivitása indokolta, de mivel a terület nagy része kiemelt üdülőkörzetté vált, a mélyszerkezet megismerését a hévízföltárásra irányuló igények is alátámasztották [PINTÉR, SZABADVÁRY 1978].

A nagyszerkezeti összefüggések megismeréséhez a gravitációs és a földmágneses mérések igen sok kiinduló támpontot nyújthatnak. 1976—78-ban került sor a terület áttekintő (kb 1 állomás/km²) gravitációs hálózatának sűrítésére. E kiegészítő mérések után a felmértség jelenleg átlagosan 10 állomás/km². A gravitációs anomáliaviszonyokat a *2. ábra (1. melléklet)* szemlélteti. A regionális gravitációs anomáliák mellett a regionális földmágneses ΔZ maximumokat is föltüntettük.

Az 1951—55-ben végzett országos áttekintő földmágneses mérések a terület közepén lévő Velencei-tótól ÉK-re ill. D-re igen nagy területre kiterjedő, nagy intenzitású földmágneses anomáliát jeleztek *(2. melléklet)*. Az anomáliák jellegéből következik, hogy a Velencei-hegységben (és környékén) a felszínen is megtalálható, nagy szuszceptibilitású andezit telérek mellett néhány száz méter mélységben számos nagyobb kiterjedésű ható is várható [VASADY-KOVÁCS 1962].

2. Módszertani megfontolások

2.1 A mélységbecslési próbálkozásokról

A gravitációs anomáliatérkép értelmezésének első lépéseként megkíséreltünk a mélyfúrásokból ismert mezozoos ás paleozoos kőzetek mélységértékei

és a Bouguer-anomália értékek között korrelációt keresni. Ha u.i. van korreláció, akkor az értelmezés egyszerű, a Bouguer-anomáliákból hozzávetőleges aljzat mélységtérképet lehet készíteni [Pintér, Stomfai 1974]. Ilyen térképeket a Bouguer-anomália és a szűrt gravitációs térképek segítségével gyakran készítettünk az ország különböző területeïn, s azokat a további kutatásokhoz eredményesen fel is használtuk. A Velencei-hegység környezetében azonban meg kellett állapítanunk, hogy a gravitációs anomáliák nem korrelálnak egyetlen fúrásból ismert képződményhatárral sem.

A fúrásokból ismert, harmadidőszaknál idősebb képződmények felszíne +220 m-től −350 m-ig, azaz 570 m intervallumban változik, míg ugyanezen fúrási pontokon a Bouguer-anomáliák változása 23 mgal.* Ha nagy, pl. $0{,}5 \cdot 10^3$ kg/m^3 sűrűségváltozást tételezünk fel az aljzat és a fedő között, akkor 100 m mélységváltozásnak megfelelő gravitációs anomáliaváltozás 2 mgal. Az 570 m mélységváltozás mindössze 11,4 mgal anomália változást indokolna, vagyis a tényleges 23 mgal változásnak mindössze felét magyarázhatjuk az aljzat mélységváltozásával.

A maradék rész a nagyjából homogén sűrűségű neogén összlet vastagságától — azaz az idősebb képződmények mélységváltozásától független — ennek okát tehát az aljzatnál mélyebben kell keresnünk.

Mivel a gravitációs anomáliáknak mélységtérképpé alakítása nem járt sikerrel, ezért a különböző szűrt térképeken jelentkező anomáliák egyénenkénti vizsgálatával kíséreltük meg az értelmezést.

2.2 Az alulvágó szűrésekről

A szűrések célja általában az, hogy a Bouguer-anomália térképen összevontan, elmosódottan jelentkező anomáliákat szétválassza, fölerősítse és ezáltal a mélybeli tömegeloszlásról jellegzetesebb kép álljon elő. Természetesen nem várható, hogy egy viszonylag nagy, változatos földtani fölépítésű területen egyetlen szűrővel mindenhol elérjük a kívánt hatást (szétválasztást, fölerősítést). A szűrők megválasztása egyébként mindig is nagymértékben szubjektív [Skeels 1967]. Magyarországon pl. igen jól beváltak a Meskó Attila által definiált alul- és fölülvágó szűrők [Meskó 1966, 1967]. Jelenlegi vizsgálatainkhoz is ezeket használtuk, mind a gravitációs, mind a földmágneses ΔZ térképre az átlagos kb. 300 m-es állomástávolságnál kicsit kisebb, $s = 250$ m mintavétel mellett.

A szűrőparaméterek (a levágás meredeksége és a mintavételi távolság) megválasztása meghatározza a szűrés jellegét. Meredek levágás és a ható mélységéhez, valamint vízszintes kiterjedéséhez viszonyított eléggé kis mintavételi távolság a második vertikális derivált jellegű anomáliatérképek előállításának kedvez, kevésbé meredek levágás és nagyobb mintavételi távolság maradékanomália jellegű térképek előállítását eredményezi [Pintér, Stomfai 1979]. A maradék-anomália jellegű térképek maximumai és minimumai általában jó kvalitatív kapcsolatba hozhatók a kisebb, felszínközeli hatók domborzatával. A derivált jellegű térképben a minimumok és maximumok a hatók széleit (a

* 1 mgal = 10^{-5} ms^{-2}

változások helyeit) jelzik, s így a hatók alakjával csak közvetett kapcsolatban vannak. Ezért igen fontos a szűrt térkép jellegének fölismerése. A szűrt anomáliák (10 000 adatra vonatkozó) gyakorisági görbéiből *(3. ábra)* kitűnik, hogy a szűrés eredményeként milyen jellegű térkép állt elő. Ha a szűrt térkép maradék-anomália jellegű, akkor az anomáliák nagyjából egyenlő gyakorisággal fordulnak elő, a gyakorisági görbén nincs kitüntetett tartomány (3. ábra *a.* görbe). Ha a térkép derivált jellegű (3. ábra *b.* görbe), akkor a gyakorisági görbe éles maximumot mutat a zérus érték környezetében. (A gyakorisági görbék maximuma ilyenkor általában kissé a negatív oldalra tolódik. Ennek oka az, hogy a mért maximumértékek általában relative nagyobbak, mint a mért minimumok). A kutatott terület $s=250$ m mintavétel melletti, alulvágó szűrővel szűrt térképe *(3. melléklet)* a 3. ábra *c.* görbéje szerint már kissé derivált jellegű, ezért például a térkép zérus vonalát — bizonyos fönntartásokkal — a földtani értelmezés szempontjából kitüntetett értékként kezelhetjük. A gravitációs térképek készítéséhez a $\sigma=2{,}0\ 10^3$ kg/m^3 átlagsűrűséggel korrigált Bouguer-anomália térképet használtuk föl. Ez az átlagsűrűség Magyarország nagy részén megfelel a felszíni, felszínközeli neogén (homokos, agyagos) összlet átlagsűrűségének. A Velencei-gránithegység területén azonban a sűrűség ennél nagyobb: $\sigma=2{,}65\ 10^3$ kg/m^3. Ezért a hegység területén elkészítettük a $\sigma=2{,}65\ 10^3$ kg/m^3-el számolt Bouguer-anomália térképre alapozott, alulvágó szűrővel számított térképet is *(4. melléklet)*.

2.3 Az analitikus lefelé-folytatásokról

A terület bonyolultsága miatt alul- és fölülvágó szűrő mátrixok mellett $h=s$, illetve $h=2s$ mélységre lefelé folytató szűrő mátrixokkal *(5. melléklet)* is kísérleteztünk [Meskó 1973]. Mivel az analitikus lefelé-folytatásokkal kapcsolatosan nem sok tapasztalatunk volt, néhány kísérletet végeztünk el a lefelé folytató mátrixok vizsgálatára. Több különböző paraméterű lefelé folytató mátrixot alkalmaztunk, mindegyikkel több szintre végeztük el a lefelé-folytatást. Az eredmények jól összehasonlíthatók egy szelvény mentén (5. melléklet). Az összehasonlítás legfontosabb eredménye az, hogy bár a különböző lefelé folytató mátrixokkal számított anomáliák horizontálisan ugyanott jelzik a hatók széleit, vertikális felbontásra — azaz a hatók mélységére vonatkozó becslésre — nem alkalmasak. A lefelé folytatott térképekhez tehát nem rendelhető mélységérték. A továbbiakban a lefelé folytató mátrixok közül — kifejezetten technikai megfontolások (térkép szélein fellépő kisebb területveszteség, az anomáliaértékek ábrázolhatósága) miatt — felülről a negyediket alkalmaztuk.

Mivel a Bouguer-anomália térképre alkalmazott alulvágó szűrő nem emelte ki mindenhol eléggé a kisebb anomáliákat, ezért a lefelé folytatott térképekre is alkalmaztuk az alulvágó szűrőket. Igen sok térképváltozat készült, itt azokat közöljük, amelyek — legalábbis helyenként — jellegzetes anomáliáikkal támpontot adnak az értelmezéshez. Az első lefelé folytatott térkép *(6. melléklet)* a Bouguer-anomália térképhez hasonló, de sokkal több részletet jelez. Ennek

alulvágó szűrővel készült térképváltozatát felülvágással simítottuk, azaz sávszűrést alkalmaztunk *(7. melléklet)*.

A második, ismételt lefelé-folytatás a mélyebb medenceterületek kisebb kiterjedésű és értékű anomáliáit tovább erősíti *(8. melléklet)*.

2.4 A felülvágó szűrésekről

A nagyobb kiterjedésű regionális hatók vizsgálatára a Bouguer-anomália térképre fölülvágó szűrővel számoltuk a regionális anomália térképet s erre a térképre a földmágneses ΔZ értékek maximumait is felrajzoltuk (1. melléklet). Megjegyezzük, hogy a fölülvágó szűrések értelme általában csak simítás; egyetlen egyszerű ható anomáliatérképét is föl lehet bontani bármelyik alul-, ill. fölülvágó szűrővel egy ún. maradék- és egy ún. regionális térképpé.

A regionális térképben kirajzolódó anomáliák tehát nem minden esetben jelentenek egy határozott, mélybeli (regionális) hatót. A mellékelt térképben csupán ott állíthatjuk nagy sűrűségű mélybeli hatók biztos jelenlétét, ahol a regionális gravitációs anomáliák regionális földmágneses anomáliákkal esnek egybe, természetesen az ilyen nagy sűrűségű hatók egyben nagy szuszceptibilitásúak is.

2.5 A földmágneses maradék-anomáliákról

A földmágneses maradék-anomáliákat *(9. melléklet)* a területnek csak arról a részéről készítettük el, ahol a mérési pontok távolsága átlagosan nem haladta meg a 300 m-t. (A ΔZ mérések a Velencei-tónak csak a felére terjedtek ki, így a ΔZ maradék-anomáliák megszerkesztése is csak ott volt lehetséges.)

A mágneses térképek értelmezésénél figyelembe kell venni azt a tényt, hogy a szórványos felszíni paleomágneses mérések szerint a kőzetek remanens mágnesezettsége jelentős és sokszor az indukált mágnesezettségtől eltérő (esetleg ellentétes) irányú lehet. Az is előfordulhat, hogy a kétféle mágnesezettség kompenzálja egymást és a kőzet nagy szuszceptibilitása ellenére sincs mérhető anomália. A remanens mágnesezettség helyenként túlsúlyban lehet és nagy intenzitású negatív anomáliát okozhat. Ami a felszíni hatókra vonatkozó mérési adat, azaz tény, az a mélybeli hatókra is igaz, ezért a kizárólag indukált mágnesezettséget föltételező hatószámítások adatait fenntartással kell fogadnunk, ilyet nem is végeztünk. A terület mágneses anomália-térképében a Velencei-hegység területén lévő, néhány kis kiterjedésű andezittelér kivételével a hegységtől K-re és D-re a pozitív anomáliák dominálnak. Ebből arra következtethetünk, hogy a mélybeli hatókban az indukált és remanens mágnesezettség vektoriális eredőjeként előálló pozitív mágnesezettség dominál. Ennek a ténynek a gravitációs anomáliákkal való összehasonlításnál van jelentősége. Ha a gravitációs és földmágneses anomáliákat ugyanazon kőzet (ható) okozza, akkor a földmágneses anomáliák maximumai a gravitációs térkép maximumaitól D,

DK, ill. DNy irányban eltolódva jelentkeznek a ható nagyságától, a mágnesezettség pontos irányától függő mértékben [MADARASI et al. 1981].

2.6 A földmágneses és gravitációs anomáliák kapcsolatáról

Ha a földmágneses anomáliák és a gravitációs anomáliák között kapcsolatot akarunk keresni, akkor föl kell tételeznünk, hogy a mágneses anomáliák hatói környezetüknél kisebb, vagy éppen nagyobb sűrűségűek, s ezért lokális gravitációs minimumot, vagy ellenkezőleg maximumot okoznak. A mágneses anomáliákat tehát bizonyos mértékben ÉK—É—ÉNy irányban el kell tolni úgy, hogy gravitációs maximummal vagy minimummal essenek össze [MAJKUTH et al. 1981]. Ez az eltolás természetesen nem egyértelmű. Ha föltételezzük, hogy a mágneses hatók környezetüknél valamivel kisebb sűrűségűek — tehát lokális gravitációs minimumot okoznak — akkor viszonylag kis mértékű É—ÉK (esetleg ÉNy) irányú eltolással a lefelé folytatott gravitációs térkép minimumaival esnek össze a ΔZ maradékanomáliák. Érdekes, hogy egy-egy anomáliacsoporton belül az eltolás iránya és mértéke meglehetősen egységes. Ha a földmágneses anomáliákat gondolatban nagyobb sűrűségű kőzetekhez kapcsoljuk, akkor a földmágneses maximumoknak gravitációs maximumokkal kell egybeesniök. Ez a lehetőség a lefelé folytatott és sávszűrővel szűrt gravitációs maradékanomália térképnél áll fenn, sőt az egyezés ebben az esetben jobbnak tűnik az előzőnél, de az eltolás mértéke nagyobb. Megjegyezzük, hogy a ΔZ maximumokat mindkét esetben jóval nagyobb mértékben kell e kutatási területen eltolni, mint azt az indukált mágnesezettség és az 1000—1500 m-nél általában nem nagyobbnak feltételezett hatómélység indokolná. Ez vagy nagyobb hatómélységre, vagy az indukált mágnesezettség irányát erősen befolyásoló remanens mágnesezettségre utal [MAJKUTH et al. 1981].

Igen jellegzetes viszont a regionális földmágneses és a regionális gravitációs anomáliák egybeesése Pázmándnál és Dinnyésnél. Az anomália-alakok feltűnő hasonlósága mellett mindkét esetben a regionális földmágneses maximum a gravitációs maximumtól D-i irányban eltolódva jelentkezik. Ez arra utal, hogy a mélybeli ható mágnesezettsége túlnyomóan indukált. Az eltolódás mértékéből azonban a ható pontos mélységére következtetni egyelőre nem tudunk, mert az esetleges remanens mágnesezettség irányát nem ismerjük és a hatók szélső értékei sincsenek pontosan kimérve. A nagy sűrűségű, nagy szuszceptibilitású ható kiterjedését (vízszintes méreteit) sem tudjuk pontosan megadni, csupán szubjektív megfontolásokra támaszkodhatunk.

E bizonytalanságok (hipotézisek) előkutatási fázisban elkerülhetetlenek. Ahhoz, hogy a gravitációs és földmágneses anomáliák kapcsolatát pontosabban vizsgálhassuk, mind a gravitációs, mind a földmágneses anomáliák részletes fölmérése, szélsőérték-helyeinek pontos ismerete szükséges. (Ebben az esetben a gravitációs térképek megfelelő átalakításával olyan pszeudomágneses térkép lenne készíthető, amely már alkalmas a földmágneses anomáliákkal való konkrét egyezés megállapításához).

2.7 Egy egyszerű gravitációs modellszámításról

A gravitációs anomáliák értelmezésénél nagyon fontos továbbá, hogy figyelembe vegyük azokat az egyszerű modellszámításokat, amelyeket akár kis zsebszámológéppel is könnyen elvégezhetünk. Ilyen egyszerű számítási eredményt mutat pl. a *4. ábra*. Mint látható, általában a legnagyobb változás értéke (a derivált anomália zérus helye) jelzi a vető helyét. Azt kell továbbá észrevennünk, hogy jellegzetesen más az anomáliakép akkor, ha a nagyobb és kisebb sűrűségű kőzetek helyzetét egy vető mentén felcseréljük (4. ábra 3. *a*. görbe helyett 3 *b*. *c*. görbe). A természetben sokkal gyakoribb eset az, hogy a nagy szélsőértékű gravitációs maradék-anomália-maximum mellett viszonylag kisebb szélsőértékű maradék-anomália-minimum alakul ki (*a* görbe). A maximum—minimum átmenet ilyenkor olyan, hogy a maximumhoz közelebb gyorsabb a változás. A vizsgált terület közelítőleg derivált jellegű szűrt térképein azonban néhol a viszonylag kis maximumértékek mellett igen nagy szélsőértékű minimumokat találunk. Ezekben az esetekben a gradiens a minimum közelében nagy. Ilyen esetben olyan földtani szituációt kell elképzelnünk, amely a 4. ábra *c* görbéjéhez tartozó modellnek felelhet meg. (A 3. ábra *c* görbéje szerint a derivált jellegű görbékre vonatkozó megállapítások közelítő jelleggel kutatási területünkön érvényesnek vehetők).

2.8 A gravitációs térképek izovonalainak szerkesztéséről

A gravitációs térképek izovonalait általában úgy szerkesztjük — kényelmi és egyszerűsítési szempontok miatt — hogy az izovonalak azokat a mgal értékeket kössék össze, ahol a mgal érték egész szám (pl. 10, 11, 12 mgal) vagy annak fele, negyede, tizede (pl. 0,25, 0,50, 0,75 mgal). Ez azonban nem mindig kedvező, mert egy más, (nem a fenti kerek) számválasztásnál az anomália rajzolata kissé megváltozna, s ezáltal az anomália-alak jellegzetesebbé válna. Számítógép segítségével mód van arra, hogy különböző értékű izovonalakból térképsorozatot szerkesszünk, s az anomália-alakra esetleg a mozaikszerűen összerakott térképváltozatból következtessünk.

3. A módszertani megfontolások alapján levonható földtani következtetések

Az előzőekben kifejtett módszertani megfontolások alapján az ismertetett térképekben az alábbi jellegzetességeket kerestük:

a) vannak-e hosszabb szakaszon lényeges irányváltozás nélkül futó, párhuzamos anomáliavonalak (a maradék-anomália térképen a zérus vonalak). Ezek u.i. nagy valószínűséggel a sűrűségkülönbséggel is kapcsolatos szerkezeti elemek (vetők, föltolódások) körülbelüli helyét jelölik ki;

b) fölismerhetők-e jellegzetes (kerek, hosszan elnyúló, gyűrűs stb.) anomália-alakok, amelyekből a ható alakjára és közvetve mibenlétére következtethetünk;

c) láthatók-e a térképen jellegzetes maximum—minimum átmenetek, vagy igen nagy minimum értékek, amelyek a szerkezeti vonalak menti tömegeloszlásról adnak képet;

d) föllépnek-e nagyobb területre kiterjedő jellegzetes anomália irányítottságok, változnak-e ezek részterületenként? Ebből u.i. esetleg az aljzat belső szerkezetére következtethetünk;

e) van-e kapcsolat a földmágneses és a gravitációs anomáliák között, azaz nagy szuszceptibilitású vulkáni eredetű kőzetekkel kapcsolatosak-e a gravitációs anomáliák;

f) van-e kapcsolat a felszíni (azaz a geológiai térképből ismert) nagyobb sűrűségű kőzetek és a környezetükben mért anomáliák között, azaz követhetők-e a felszíni kibúvások a fedett területrészeken.

A legfontosabb gravitációs és földmágneses anomáliákat olyan jelkulccsal láttuk el, amely kifejezi az anomáliás jellegét, és egyben utal annak lehetséges, földtani jelentésére *(5. ábra* ill. *10. melléklet)*. Ezen az összefoglaló eredménytérképen feltüntettük a terület legjellegzetesebb anomália-irányait, az alulvágó szűrőkkel számított anomáliatérképek zérusvonalai alapján. A különböző térképek zérus vonalainak egy része jó közelítéssel egybeesik (kisebb eltérések a kerekítésekből és a szerkesztésből is adódnak). Azokat a vonalszakaszokat, amelyek két, vagy három térképen egybeesnek, vastag vonallal jelöltük. Úgy véljük, hogy ezek ott fordulnak elő, ahol olyan nagy a sűrűségváltozás, hogy az a kisebb (haránt-, vagy egyéb irányú) sűrűségváltozások hatását elnyomja. A vonalak két oldalán előjel jelzi, hogy a zérus vonal mentén a pozitív vagy a negatív anomália szélsőértéke nagyobb-e. (Itt utalunk a 4. ábrára, amely világosan mutatja, hogy a zérus vonalak a szerkezeti elem jellegétől függően eltolódnak. Csak függőleges vető esetén fut a zérus vonal pontosan vető fölött).

Vékonyabb vonallal jelöltük azokat a nulla vonalakat, amelyek ugyancsak egy-egy térképben jelentkeznek, de vagy folytatását jelentik a vastag vonalaknak, vagy pedig jellegzetes irányítottságot mutatnak egy-egy területrészen.

Az összefoglaló térképen feltüntettük a jellegzetes gravitációs anomália-alakzatokat is, jelezve, hogy van-e kapcsolatuk földmágneses anomáliákkal; föltüntettük továbbá azokat a jellegzetes földmágneses maradék-anomáliákat, amelyek nem kapcsolódnak gravitációs anomália-alakzatokhoz. Ahol a fúrások, vagy kibúvások alapján a gravitációs maximumokat konkrét földtani képződményként értelmezhettük, ott ezt is jelöltük.

A gravitációs anomáliáknak az előzőekben fölsorolt jellegzetességei alapján tehát a Velencei-hegységben és tágabb környezetében a következő — mélybeli sűrűségeloszlással kapcsolatos — szerkezeti elemek jelölhetők ki (5. ábra, 10. melléklet):

A Velencei-hegység szerkezeti elemeire utaló anomáliák

A Velencei-hegység gránitplutonját félkörívben egy kb. 1 km széles maradék-anomália minimum-sáv veszi körül (4. melléklet). E minimum-sávot É-on és ÉNy-on több pozitív gravitációs maradék-anomália övezi. Ezek részben a felszínen lévő, a gránitnál idősebb, paleozoos palakibúvások területére esnek, kézenfekvő tehát a maradék-anomália-maximumokat a palák eltemetett folytatásaként értelmezni. A minimum-sávot a gránit és az idősebb paleozoikum tektonikus érintkezési zónájaként foghatjuk föl. Magát a gránitplutont több sugárirányú repedés (gravitációs maradék-anomália minimum) osztja nagyjából három részre. A Velencei-hegységet DK-ről egy (a Velencei-tó csapásával egyező) ÉK—DNy irányú szerkezeti elem (vető, eltolódás) határolja le. Ez az elem legjobban a 3. és 6. melléklet gravitációs anomália képében látható.

Eltemetett vulkáni képződményekre utaló anomáliák

A gravitációs maradék-anomáliák jellegzetes kör, illetve körgyűrű alakja és a mágneses maradék-anomáliák eloszlása alapján a Velencei-hegységtőlK-re, valamint a Velencei-tótól D-re és K-re három mélybeli vulkáni képződmény tételezhető fel (3, 6, 8. és 9. melléklet). Két esetben a regionális gravitációs és regionális mágneses anomáliák egybeesése és alakjuknak hasonlósága alapján (2. ábra, 1. melléklet) mélybeli, nagy sűrűségű és nagy szuszceptibilitású intruzióra is következtethetünk (Pázmánd, Dinnyés). A harmadik gyűrű alakú gravitációs anomáliánál (Kápolnásnyék) kisebb földmágneses anomáliák kimutathatók ugyan, de egybeesésük a gravitációs anomáliákkal nem jellegzetes. Itt valószínűleg erősen lepusztult, mélyebb vulkáni képződményről van szó.

Ismeretlen határa utaló anomáliák

Az eredménytérkép (5. ábra, 10. melléklet) DK-i sarkában (Sárosd) látható gyűrű alakú képződmény (7. mellékleten látható maradék-anomália) határa ismeretlen. Itt nagyobb földmágneses anomáliák biztosan nincsenek (kisebb anomáliák kimutatásához pedig a jelenlegi fölmértség nem elegendő).

A seregélyesi triász dolomit sasbérc kiterjedésére utaló anomáliák

A fenti ismeretlen mélybeli képződmény és a dinnyési eltemetett vulkán között valamennyi gravitációs térképben (pl. 8. melléklet) hosszú, keskeny, ÉÉK csapású, kb. 10 km hosszú gravitációs maximum látható. A fúrások itt triász dolomit aljzatot értek (Seregélyes). Az emelt helyzetű aszimmetrikus triász dolomit sasbérc a gravitációs térkép alapján jól körülhatárolható.

Mélybeli vetőre utaló anomáliák

A seregélyesi dolomit sasbérc, valamint a dinnyési eltemetett vulkán K-i oldalát valamennyi gravitációs térképben jól kirajzolódó, vetőre utaló anomáliák zárják le. A vető a Velencei-tótól kiindulva ÉD irányú, majd a seregélyesi dolomit sasbérc mentén ÉÉK-DDNy irányt vesz fel. A vetőkre utaló izovonalak sűrűsége, azaz a gradiens nagysága a vető mélységétől, valamint a vető két oldalán lévő képződmények sűrűségkülönbségétől függ. Az említett vető esetében É-on a viszonylag kisebb sűrűségű eocén vulkáni képződmény, D-en a nagyobb sűrűségkülönbséget jelentő triász dolomit érintkezik a levetett rész fölötti miocén öszlettel. Ezért a gradiens D-en (Seregélyesnél) valamivel nagyobb.

Többszörös vetőkre és feltolódásokra utaló anomáliák

Az eredménytérkép DNy-i sarkából kiindulóan kb. ÉK csapású, bonyolult, vetőkre és feltolódásokra utaló anomáliák láthatók valamennyi gravitációs térképen (3., 6., 7., 8. melléklet). Pontos kimutatásukhoz a jelenlegi fölmértség (10—12 állomás/km) azonban nem elegendő.

E bonyolult szerkezet mentén a felszíni kibúvásokból és fúrásokból ismert, változatos kőzettani kifejlődésű, kis mélységű paleozoos blokk (Csaják—Jenő—Sárszentmihály—Úrhida—Kőszárhegy) hirtelen lehatárolódik, ismeretlen aljzatú neogén medencével érintkezik.

Föltolódásra utaló minimumzónák

Az említett paleozoos blokk É-i peremét igen nagy gravitációs minimumértékkel jelentkező, K—Ny irányú zóna zárja le, amely a térkép Ny-i határán túl még igen hosszan nyomozható. Ilyen viszonylag keskeny és hosszú, de nagy szélsőértékű minimumzóna Magyarország területén csaknem egyedülálló jelenség, földtani értelmezése külön figyelmet érdemel. E minimumzónának Csórtól Ny-ra lévő szakasza a fúrások és a geológiai vizsgálatok szerint többszörös föltolódás [Kókay 1968]. A minimumzónák ismétlődése is többszörös föltolódásra enged következtetni itt. Föltehetően ugyanígy föltolódási zónaként kell értelmezni a minimumzónának Csórtól K-re lévő szakaszát is.

A medencealjzat szerkezetére utaló anomáliák

Viszonylag kis anplitúdójú, de jellegzetes ÉK—DNy orientációjú gravitációs maradék-anomáliák jelentkeznek a Velencei-hegységtől É-ra és Ny-ra. A pázmándi eltemetett vulkántól É-ra a hosszan elnyúlt földmágneses maradékanomália maximumok (9. melléklet) is ugyanezt az irányt követik. A medence-

aljzatban tehát ilyen irányú szerkezeti elemekre, s e szerkezeti elemek irányát követő magmás képződményekre (a fúrások szerint diabázra) kell számitanunk e területen. A Velencei-tótól DNy-ra (a seregélyesi aszimmetrikus sasbérc és a térkép Ny-i szélén lévő paleozoos blokk között) szintén jellegzetes a gravitációs anomáliák orientációja. A kb. ÉÉK irányítottságú anomáliák párhuzamosak a seregélyesi dolomitszirtet K-ről lezáró vetővel. A Ny-i paleozoos blokk belső szerkezetére túlnyomóan ÉD és KNy irányú gravitációs anomáliák utalnak.

A regionális gravitációs anomáliatérkép (2. ábra, 1. melléklet) szerint a seregélyesi dolomit sasbérctől Ny-i irányban a gravitációs anomáliák egyenletesen csökkennek a Tác—Börgönd közötti minimumig. Ezt a gravitációs „lejtőt" — néhány fúrás és a szeizmikus mérések előzetes értékelése alapján — nem az ismeretlen kifejlődésű paleozoos—mezozoos medencealjzat fokozatos mélybe süllyedése okozza. A kb. 15 mgal anomáliaváltozás túlnyomórészt a medencealjzaton belüli sűrűségváltozásra vezethető vissza.

A területet K-ről lezáró, mélybeli törésre utaló anomáliák

Az itt nem közölt Bouguer-anomália térképen, a mellékelt regionális- és a két lefelé folytatott anomália térképen izovonal-sűrűsödéssel, a mellékelt maradék-anomália térképeken pedig zérus vonalakkal jelentkezik a terület K-i határán egy mélybeli törésre utaló anomália-rendszer (pl. 1. és 8. melléklet). E csaknem 40 km hosszú, nagy gradiensekkel jelentkező, széles sáv mentén K-i irányban a medence elmélyül, a paleogén és a miocén összlet kivastagszik. E feltételezett törés kimutatása más geofizikai módszerekkel eddig nem járt sikerrel.

*

A fölsorolt jellegzetes anomáliák földtani értelmezése természetesen különböző megbízhatóságú. Ennek számos oka van: a gravitációs és földmágneses mérési hálózat egyenetlensége, néhol a hatók mélységéhez és kis kiterjedéséhez viszonyított ritkasága, a hatóknak környezetükhöz viszonyított nagyon változó sűrűségkülönbségük, a medencealjzaton belüli sűrűségváltozások stb. mellett a mélyfúrások hiánya, különösen a terület K-i és D-i részén. Az eredménytérkép csupán összefoglalja azokat a szerkezeti elemeket, amelyek különböző megbízhatósággal jelentkeznek, azért, hogy megkönnyítse a tájékozódást a sok különböző gravitációs és földmágneses térkép között. Tulajdonképpen vitaalapot szolgáltat egy későbbi komplex értelmezéshez. Egyben bizonyítja, hogy már néhány mélyfúrás ismeretében a gravitációs és a földmágneses anomáliák sokoldalú vizsgálata komoly eredményeket szolgáltat a mélyszerkezet megismeréséhez, még bonyolult földtani felépítésű területen is.

A mikrofilmen mellékelt ábrák magyarázata

1. melléklet. A Velencei-hegységi kutatási terület a regionális gravitációs és földmágneses anomáliákkal
1 — paleozoikum a felszínen; 2 — gránit a felszínen; 3 — metaszomatit (andezit) a felszínen; 4 — mélyfúrásban elért paleozoikum általában (Pz), gránit (γ), perm (P), triász (T); 5 — regionális gravitációs anomáliák (értékköz 1 mgal); 6 — földmágneses ΔZ értékek regionális maximumai

2. melléklet. A Velencei-hegység és tágabb környezetének áttekintő földmágneses (ΔZ) anomália-térképe (értékköz 10 nT)

3. melléklet. A Velencei-hegység és tágabb környezetének maradék-anomália térképe.
$\sigma = 2{,}0 \cdot 10^3$ kg/m^3; $s = 250$ m; $\kappa = 4$

4. melléklet. A Velencei-hegység maradék-anomália térképe. $\sigma = 2{,}65 \cdot 10^3$ kg/m^3; $s = 250$ m; $\kappa = 4$
1 — gránit a felszínen; 2 — paleozoikum a felszínen

5. melléklet. Különböző paraméterű lefelé folytató negyed mátrixok és a mátrixok alkalmazása ugyanazon szelvény mentén

6. melléklet. A Velencei-hegység és tágabb környezetének lefelé folytatott térképe

7. melléklet. A Velencei-hegység és tágabb környezetének lefelé folytatott, majd sávszűrővel szűrt maradék-anomália térképe

8. melléklet. A Velencei-hegység és tágabb környezetének kétszeresen lefelé folytatott térképe

9. melléklet. A Velencei-hegység környezetének földmágneses ΔZ maradék-anomáliái

10. melléklet. A gravitációs és földmágneses anomáliák földtani értelmezése
1 — paleozoikum a felszínen; 2 — gránit a felszínen; 3 — metaszomatit (andezit) a felszínen; 4 — fúrásban elért paleozoikum általában (Pz), gránit (γ), perm (P) és triász (T) képződmény; 5 — jellegzetes kör alakú gravitációs maradék-anomália, amelynek területén a földmágneses maradék-anomáliák sűrűsödnek: föltételezett mélybeli vulkáni képződmény; 6 — a regionális gravitációs és földmágneses anomáliák egybeesése: diorit intruzió; 7 — jellegzetes gyűrű alakú gravitációs anomália: ismeretlen képződmény; 8 — hosszan elnyúlt, keskeny gravitációs maradék-anomália: a seregélyesi fúrásokból ismert dolomit feltételezett elterjedése; 9 — a gránit-plutont övező felszíni paleozoos palakibúvások folytatásaként látható gravitációs maximum: a paleozoos pala mélybeli folytatása; 10 — hosszan elnyúlt mágneses maradék-anomália: a gravitációs térképekben jelentkező irányokhoz kapcsolódó földmágneses ható; 11 — az ismert (ill. feltételezett) vulkáni képződményekhez nem tartozó és nem szerkezeti vonalhoz kapcsolódó földmágneses anomália: föltételezhetően lokális eocén vulkanizmussal kapcsolatos ható; 12 — viszonylag nagy anomália-különbséggel jelentkező pozitív és negatív maradék-anomáliát elválasztó, hosszan nyomozható zérus vonal, a relatíve nagyobb anomáliaérték előjelének föltüntetésével: sűrűségkülönbséggel jelentkező vető vagy feltolódás; 13 — kisebb anomália-különbségű pozitív és negatív maradék-anomáliákat elválasztó, vagy rövidebb szakaszon nyomozható zérusvonal: feltételezhetően az aljzat belső szerkezetével összefüggő sűrűségváltozás; 14 — izovonal-sűrűsödéssel (nagy gradiensekkel) jelentkező széles zóna: föltételezhető mélybeli törés

А. ПИНТЕР

ИНТЕРПРЕТАЦИЯ ГРАВИТАЦИОННЫХ И ГЕОМАГНИТНЫХ АНОМАЛИЙ В РАЙОНАХ СО СЛОЖНОЙ ТЕКТОНИКОЙ (ГОРЫ ВЕЛЕНЦЕ)

Широкое окружение гор Веленце представляет собой равнину, покрытую паннонской толщей. Относительное небольшое количество данных бурения является недостаточным для выявнения глубинной структуры. Автором сделана попытка оконтурить важнейшие элементы глубинных структур по вариантам карт силы тяжести и геомагнетизма. Сводная карта может способствовать дальнейшим работам по геофизике и бурению, а методические рассуждения по гравиметрии и геомагнетизму могут оказаться полезными при интерпретации гравитационных и геомагнитных аномалий подобных покрытых районов.

GEOPHYSICAL TRANSACTIONS 1983
Vol. 29. No. 4. pp. 297—330

INTERPRETATION OF COMPLEX RESISTIVITY AND DIELECTRIC DATA PART I

W. H. PELTON[1], W. R. SILL[2], B. D. SMITH[3]

Dielectric spectra and complex resistivity spectra are closely related through the general theory of relaxation. It is possible to group a great many simple models which have been proposed for IP or dielectric phenomena into three relaxation "families". We have examined the behavior in the frequency domain, in the time domain, and in the distribution function domain of several of the more common relaxation models.

As part of our organization of the models into groups and as part of our examination of the relationships between different models, we have created three generalized expressions which describe a very broad range of relaxational behavior. However, not often is it possible to determine all the parameters of the more general models from observed data. The most useful model, we have found, is the simple Cole—Cole model, which merely describes a symmetric peak in a plot of log phase versus log frequency, or a symmetric "bump" in a plot of the imaginary versus the real part of the transfer function.

d: complex resistivity, frequency domain, Cole—Cole model

1. Introduction

In the past few years, geophysicists concerned with measuring the electrical properties of rocks have been stimulated by developments in two somewhat different areas of research. The first of these involves mining exploration where portable field equipment has been developed to measure induced polarization response at a number of frequencies or decay times [VAN VOORHIS et al. 1973, HALLOF 1974]. The additional spectral information is being used in an attempt to discriminate between different types of polarizable materials [ZONGE 1972, PELTON et al. 1973, ZONGE and WYNN 1975, KATSUBE 1975], to predict more accurately the concentration of metallic mineralization [GRISSEMAN 1971; SILL and DEWITT 1976], and to remove inductive electromagnetic coupling response from IP data [HALLOF 1974, WYNN and ZONGE 1975, PELTON et al. 1978].

The second area of recent activity in rock electrical measurements involves study of the complex dielectric constant of lunar rocks and soils returned by the Apollo manned space program [OLHOEFT et al. 1974]. The results of these measurements are intended to aid the remote sensing of the solar system by

[1] Phoenix Geophysics Limited, Willowdale, Ontario, Canada
[2] Departme. of Geology and Geophysics, University of Utah, Salt Lake City, Utah, USA
[3] United States Geological Survey, Denver, Colorado, USA
Manuscript received: 22. 7. 1983

characterizing the dielectric relaxation phenomena and its dependence on mineralogical composition, as well as the dependence of the relaxation parameters on other physical variables, such as temperature [SAINT-AMANT and STRANGWAY 1970].

Although the two research areas may appear rather diverse since they involve consideration of different physical processes, they are actually very closely related through the general theory of linear relaxation response [SHUEY and JOHNSON 1973]. This close relationship is demonstrated by the result that the most promising mathematical model currently being used to describe the bulk electrochemical polarization of mineralized rocks [MADDEN and CANTWELL 1967, PELTON et al. 1973] was originally introduced by researchers concerned solely with dielectric relaxation [COLE and COLE 1941].

While progress has been made in acquiring accurate complex resistivity and dielectric data over a larger frequency range, less has been accomplished regarding the analysis of these spectra. FRASER et al. [1964] categorized conductivity spectra by the terms "concave-up" and "concave-down" and ZONGE and WYNN [1975] make the distinction between type A, B, and C response based on the slope of a Cole—Cole plot. Both methods are capable of indicating very gross features in the data; however, in order to characterize subtle changes in complex resistivity spectra with variable grain size or sulfide concentration [GRISSEMAN 1971] or to describe variations in dielectric data due to increasing temperature [SAINT-AMANT and STRANGWAY 1970], it is essential to develop a quantitative rather than a qualitative description of spectra. This requires adoption of some mathematical model and a method for determining model parameters from spectral data.

The purpose of this paper is

— to summarize briefly the essential requirements of relaxation models for complex resistivity and dielectric behavior,

— to examine closely the behavior in the frequency and time domains of various models which have been suggested for electrical relaxation in rocks,

— to investigate the differences and interrelationships between these models,

— to describe a ridge regression inversion technique for determining the optimum mathematical model fitting various complex resistivity and dielectric data, and

— to illustrate some applications of the inversion scheme, including selection of an appropriate model, quantitative evaluation of various spectra and transformation between the frequency domain and the time domain.

2. Complex resistivity and complex dielectric constant

For low current density ($J < 10^{-2}$ A/m^2) and constant temperature, pressure and composition, it is observed that the relationship between current den-

sity, $\underline{J}$, and electric field, $\underline{E}$, in rocks is linear. This allows the relation between $\underline{E}$ and $\underline{J}$ to be expressed by a constant of proportionality. If the rock sample is large enough to be considered homogeneous, the constant is usually considered to be independent of position. In the general case the constant is a tensor quantity, but for many practical measurements, rock materials are approximated as isotropic and the constant reduces to a scalar.

We now make the distinction between "conduction current", $\underline{J}_c$, carried by charges which are free to move distances larger than the order of atomic dimensions and "displacement current", $\underline{J}_d$, which involves reorientation of bound charge over distances which are of the order of angstroms [FULLER and WARD 1970]. Maxwell's second equation may be written

$$\nabla \times \underline{H} = \underline{J}_c + \underline{J}_d \tag{1}$$

where

$$\underline{J}_d = \frac{\partial}{\partial t} \underline{D} \tag{2}$$

is the displacement current. Resistivity, ρ, is now defined by the linear relation between conduction current density and electric field,

$$\underline{E} = \rho \underline{J}_c \tag{3}$$

The resistivity can be considered entirely real only if the relation between $\underline{J}_c$ and $\underline{E}$ is completely independent of time. However, it is possible to describe much more general, time-dependent relationships between $\underline{J}_c$ and $\underline{E}$ considering ρ to be a complex function of frequency. We note that if $\underline{E}$ is related to $\underline{J}_c$ by any linear operator with time-invariant parameters (e.g. integrodifferential operator with constant coefficients) then when $\underline{J}_c$ is of the form $e^{i\omega t}$, $\underline{E}$ is of the form $\lambda(\omega)e^{i\omega t}$. In other words, complex exponential functions are eigenfunctions of linear time-invariant operators and the complex constant of proportionality, $\lambda(\omega)$, is the eigenvalue for the particular frequency, ω, being considered [PAPOULIS 1962 p. 84]. Thus resistivity may be considered a complex function of frequency describing the eigenvalues at all frequencies for the linear operator relationship between $\underline{J}_c$ and $\underline{E}$. Conversely, if the relationship between $\underline{J}_c$ and $\underline{E}$ is unknown, we may attemp to measure $\rho(\omega)$ over the frequency range of interest and thereby deduce the relationship.

In a similar manner we can consider complex permittivity, $\varepsilon(\omega)$, as describing the linear operator relation between electric field, $\underline{E}$ dielectric displacement $\underline{D}$,

$$\underline{D}(\omega) = \varepsilon(\omega)\underline{E}(\omega) \tag{4}$$

or alternatively, we may divide $\varepsilon(\omega)$ by a constant value, ε_0, the permittivity of free space, and examine $K(\omega) = \varepsilon(\omega)/\varepsilon_0$, the complex dielectric constant.

The relationship between displacement current density, $\underline{J}_d$, and electric field, $\underline{E}$, is now obtained by differentiating $\underline{D}(t)$ with respect to time, resulting in

$$\underline{J}_A(\omega) = i\omega\varepsilon(\omega)\underline{E}(\omega) \tag{5}$$

for $e^{i\omega t}$ time dependence. And we have, in general, for Maxwell's second equation in the frequency domain

$$\underline{J}_T(\omega) = [1/\rho(\omega) + i\omega\varepsilon(\omega)]\underline{E}(\omega) \tag{6}$$

where

$$\underline{J}_T(\omega) = \nabla \times \underline{H}(\omega) \tag{7}$$

is the total current density.

Since all conventional electrical measurements are limited to monitoring directly or indirectly $\underline{J}_T$ and $\underline{E}$, there is some ambiguity in dividing the real and imaginary parts of $[1/\rho(\omega) + i\omega\varepsilon(\omega)]$ between real and imaginary resistivity and between real and imaginary permittivity. As has been demonstrated by some researchers, it is possible to completely omit out-of-phase or imaginary resistivity and to attribute the phase lag between $\underline{J}_T(\omega)$ and $\underline{E}(\omega)$ in mineralized rocks at low frequency as entirely due to the permittivity. If this is done, the dielectric constant must be considered larger than 10^8 to produce phase angles of 10 milliradians in 100 Ωm material at 10^{-2} Hz. Physically, this requires that charge be separated by distances of the order of centimeters rather than of the order of angstroms. We believe that charge which is able to travel such large distances is more appropriately labelled "free" as opposed to "bound", and that the phenomena which give rise to such polarization behavior are more correctly called complex resistivity phenomena rather than complex dielectric phenomena. In this regard we are in full agreement with FULLER and WARD [1970] that the interpretation of rock electrical properties in terms of abnormally large dielectric constants is both unnecessary and undesirable.

By making the distinction between free and bound charge and by limiting bound charge to displacements of the order of angstroms, we effectively restrict the magnitude of the dielectric constant to values approximately between 1.0 and 80. Thus if we are interested solely in measuring the electrochemical polarization of wet, mineralized rocks we may usually ignore the effect of displacement currents if the frequency range is limited to less than 10^4 or 10^5 Hz. For example, the error in phase due to a dielectric constant of 35 for a rock resistivity of 100 Ωm is approximately 20 milliradians at 10^5 Hz and only 2 milliradians at 10^4 Hz. For lower resistivities the error is proportionally lower. If processes involving only displacement currents are of interest, we attempt to decrease the effect of conduction currents by carrying out measurements on thoroughly dry rocks at high frequencies, so that the error term, $1/i\omega\rho(\omega)$, in the measurement of $\varepsilon(\omega)$ is minimized. Alternatively, if it is not possible to reduce these errors to insignificantly low levels, both $\rho(\omega)$ and $\varepsilon(\omega)$ may be included in the forward model. We can then attempt to determine parameters for both of the functions through simultaneous inversion.

3. Linear system theory

Time invariance

In order to give meaning to the terms "complex resistivity" and "complex permittivity" we have assumed that the electrical properties of rocks may be described by parameters which remain constant over the measurement time scale. This condition of time invariance poses restrictions on the form of the linear operator relation between input, $F(t)$, and output, $G(t)$. For the models we will be considering the relation can be described by

$$q(D_t)G(t) = F(t) \tag{8}$$

where D_t denotes differentiation with respect to time and $q(x)$ is a rational or transcendental expression with constant coefficients.

Transfer function

If the Laplace transform is applied to (8), and $F(0)=0$, the result is

$$q(s)g(s) = f(s) \tag{9}$$

where s is the transform variable.

The term,

$$h(s) = \frac{1}{q(s)} \tag{10}$$

is the transfer function and relates the transform of $F(t)$ to the transform of $G(t)$.

We will define the Fourier transform by

$$f(\omega) = \int_{-\infty}^{\infty} F(t)e^{-i\omega t}\,dt. \tag{11}$$

Then if we are dealing with causal inputs and with linear, time-invariant, causal systems, the transfer function in the Fourier transform or frequency domain is simply $h(\omega)$ where $i\omega$ is substituted for s.

Causality

The condition of causality requires that the output $G(t)$ always be zero for $t<0$ if the input $F(t)$ is zero for $t<0$. Thus the impulse response, $H(t)=G(t)$, when $F(t)=\delta(t)$, must be zero for $t<0$. In general, the output, $G(t)$, of a linear, time-invariant system is obtained by convolving the input, $F(t)$, with the Green's function or impulse response of the system,

$$G(t) = \int_{-\infty}^{\infty} F(t-t_1)H(t_1)\,dt_1. \tag{12}$$

However, for causal inputs and causal systems, since $F(t)=0$ and $H(t)=0$ for $t<0$ the convolution integral reduces to

$$G(t) = \int_{0}^{t} F(t-t_1)H(t_1)\,dt_1. \tag{13}$$

Causality also places restrictions on $h(\omega)$, the transfer function or spectrum of $H(t)$,

$$h(\omega) = \int_{-\infty}^{\infty} H(t)e^{-i\omega t}\,dt. \tag{14}$$

Since $H(t)=0$ for $t<0$, the real and imaginary parts of $h(\omega)$ must be Hilbert transform pairs [BRACEWELL 1965, p. 272]. This requirement actually provides an independent check on the quality of field and laboratory measurements. If the real and imaginary parts are not Hilbert transform pairs, either the measurement system is defective or the current density is so large that non-linear effects are created and linear system theory can no longer be applied.

Closely related to the idea of causality is another constraint which we will loosely call "no time delay". By invoking causality we only prevent the impulse response from "occurring" before $t=0$; we say nothing about how long it may be delayed after $t=0$. A delay could be introduced physically by a finite propagation time or artificially by lack of synchronization between receiver and transmitter clocks; however both these effects might be treated more appropriately as measurement difficulties and thus be excluded from transfer functions which attempt to model electrical properties.

Stability

An additional common property of most physical systems is that of stability. This requires that the output be bounded if the input is bounded. We find that this condition applies to all rock electrical measurements. If, for example, the input is a current step-function, the measured electric field cannot rise to infinity; it must be limited to some finite value at large times. This requirement is equivalent to the absolute integrability of the impulse response [PAPOULIS 1962, p. 85]

$$\int_{-\infty}^{\infty} |H(t)|\,dt < \infty \tag{15}$$

Simple transfer functions which do not satisfy this requirement are ones which have singularities at the origin. A resistivity transfer function having $(i\omega)^{-c}$ behavior $(0<c\leqq 1)$ near $\omega=0$ will have an impulse response which behaves as t^{c-1} for large time. The integral given in (15) diverges, and we note that the step function response is indeed unbounded as $t\to\infty$ (it tends to infinity as t^c).

If we wish to require similarly that the output be bounded at $t=0$ (for a bounded input), we must also rule out singularities in the transfer function at $\omega=\infty$. An example would be a conductivity transfer function which has $(i\omega)^c$ behavior $(0<c<1)$ as $\omega\to\infty$. The step function response for this transfer function behaves as t^{-c} for small t and is consequently unbounded as $t\to 0$.

Since conductivity is the reciprocal of resistivity, this suggests that both resistivity and conductivity transfer functions should have finite, non-zero asymptotes at high and low frequency. These requirements are necessary to prevent unbounded response to simple step-function current or voltage excitation.

Relaxation

We can put further constraints on the behavior of the transfer function between its low and high frequency asymptotes by noting that rocks are passive elements which exhibit only relaxation behavior in response to electrical stimuli. By "passive" we mean that rocks do not generate their own output, and by "relaxation behavior" we observe that the lowest resonance frequency is around 10^{13} Hz—far above the frequency range of interest in geophysical exploration.

A thorough mathematical description of relaxation has been given by SHUEY and JOHNSON [1973]. Their postulate of "pure relaxation" restricts all the singularities of relaxation transfer functions to lie only on the positive imaginary axis of the complex frequency plane (for our definition of the Fourier transform). They further make the distinction between resistivity and conductivity relaxation, where the former describes the voltage response to a current input and the latter describes the current response to a voltage input. These two relaxation transfer functions are quite different in form. We note that if

$$h(\omega) = |h(\omega)|\, e^{i\Phi(\omega)} \tag{16}$$

where $|h(\omega)|$ is the amplitude and $\Phi(\omega)$ is the phase, then the amplitude of the resistivity transfer function for mineralized rocks is a decreasing function of frequency, whereas the amplitude of the conductivity transfer function is an increasing function of frequency. Since we observe that $|\rho(\omega)|$ and $|\varepsilon(\omega)|$ are both decreasing functions of frequency we will attempt to deal exclusively with relaxation models which produce this type of amplitude behavior *(Figure 1)*.

One way of specifying such a relaxation model is to require that the distribution function, i.e. the inverse Laplace transform of the impulse response, be entirely positive. With this final requirement we are assured that $|h(\omega)|$ will be a monotonically decreasing non-negative function of frequency and that $H(t)$ will be a monotonically decreasing non-negative function of time for $t>0$. Since the step-function response, $U(t)$, is obtained by integrating $H(t)$,

$$U(t) = \int_0^t H(\lambda)\, d\lambda, \tag{17}$$

it must be a monotonically increasing function. The negative step-function response,

$$V(t) = 1 - U(t), \tag{18}$$

is then monotonically decreasing and we are consistent in relating this type of relaxation model only to those processes which produce "decay" behavior.

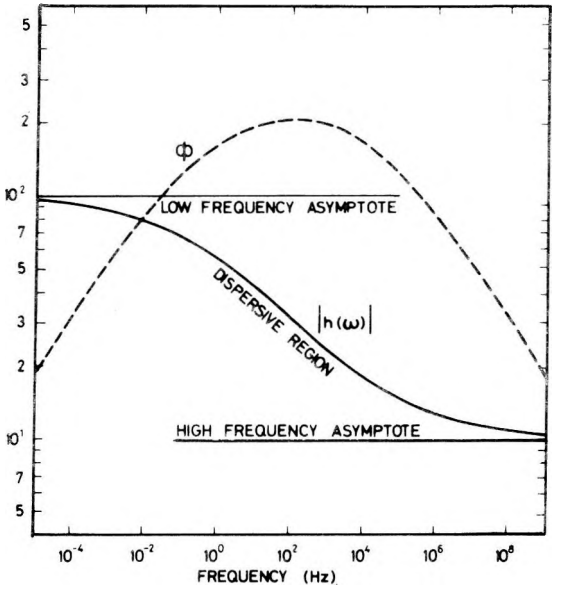

Fig. 1. Typical relaxation transfer function

1. ábra. Jellegzetes relaxációs átviteli függvény

Рис. 1 Характерная функция релаксиционной передачи

4. Equivalent circuits

A linear, time-invariant system may be concisely described by its transfer function, $h(\omega)$, impulse response,, $H(t)$, negative step-function response, $V(t)$, or linear operator, $q(D_t)$, since all are uniquely interrelated. An alternative, popular method of describing these systems is by means of an equivalent circuit. The circuit representation may provide additional insight into the physical processes taking place. However, such descriptions are inherently non-unique: we may choose either series or parallel combinations of components which result in the same transfer function. This ambiguity is clearly illustrated by *Figure 2.* The three equivalent circuits appear distinctly different, yet all these have the same mathematical expression for the impedance transfer function:

$$h(\omega) = R\left[1 - m\left(1 - \frac{1}{1 + (i\omega\tau)^c}\right)\right]. \tag{19}$$

From complete spectral measurements of the impedance of the equivalent circuit we can determine only four parameters, R, m, τ, and c, whereas the equivalent circuit given in Figure 2/c has five variables: R_0, R_1, R_2 X and c (circuits 2/*a* and 2/*b* are merely specific examples of 2/*c* for $R_2 = \infty$ or $R_0 = \infty$). Thus, in this simple example we are faced with the fundamental ambiguity of a system of four equations with five unknowns.

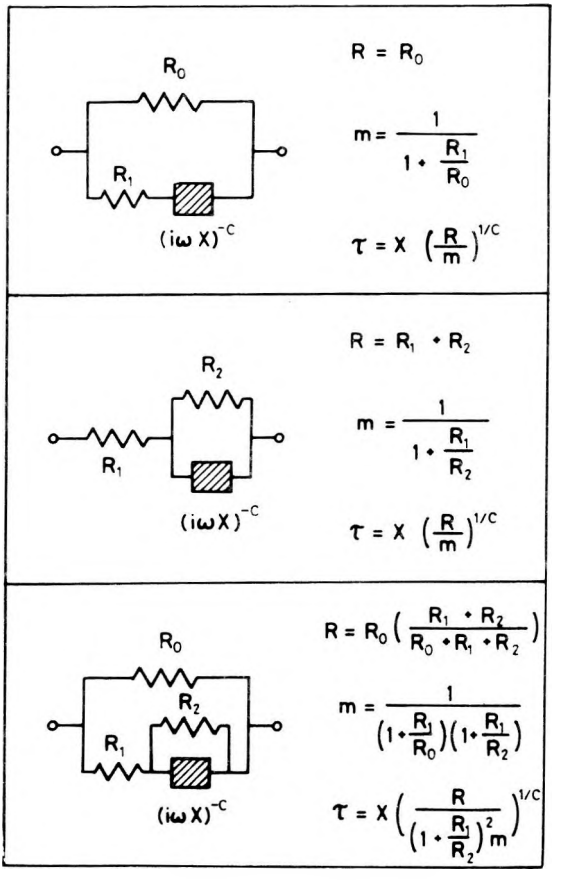

Fig. 2. Three different equivalent circuits giving the same Cole—Cole relaxation response

2. ábra. Három különböző ekvivalens áramkör, amely ugyanazt a Cole—Cole relaxációs választ adja

Рис. 2. Три различные эквивалентные схемы, дающие одинаковый релаксационный ответ типа Кол—Кол

Unless we specify the type of input and output, there is even further ambiguity in the choice of components for an equivalent circuit having a specific mathematical expression for the transfer function. For example, we may choose to discuss only equivalent circuits which have current as input, voltage as output and complex impedance as the transfer function. The models then closely simulate IP phenomena where the input is conduction current density, $\underline{J}_c(\omega)$, the output is electric field, $\underline{E}(\omega)$, and the transfer function is complex resistivity, $\rho(\omega)$. In order to obtain the desired type of relaxational behavior with this input and output we are restricted to using resistances and capacitance-type elements. Using inductances and resistances produces conductivity-type relaxation, and using both capacitances and inductances as well as resistances provides two energy storage mechanisms, which in turn results in some form of resonant behavior: either underdamped, critically-damped or overdamped. All of these types of resonance arise from transfer functions which have singularities off the positive imaginary axis of the complex plane.

Alternatively, we may choose to consider equivalent circuits which more closely approximate dielectric behavior. Since the input in this case is electric field, $\underline{E}(\omega)$, the output is displacement, $\underline{D}(\omega)$, and the transfer function is complex permittivity, $\varepsilon(\omega)$, it is more common to postulate equivalent circuits which have voltage as input, charge density as output, and complex capacitance as the transfer function [DANIEL 1967]. If we again restrict our choice of components to only resistances and capacitances the result is an equivalent circuit whose transfer function (complex capacitance), has poles only on the positive imaginary axis, and whose amplitude is a monotonically decreasing function of frequency. It turns out, however, that the roles of capacitance and resistance are exactly reversed. When considering impedance, i.e. complex resistance, a circuit composed of only a single resistance is frequency-independent and the impulse response is a delta function. Addition of at least one capacitance is required for frequency-dependent behavior. Exactly the converse is true when considering complex capacitance. It is necessary to add a resistance to the single capacitance in order to simulate a "lossy dielectric" and thus create frequency-dependent behavior.

With these considerations in mind we will later discuss only the first type of equivalent circuit model for relaxation: that which has current for the input, voltage for the output and complex impedance for the transfer function. The mathematical models we develop in this manner will be equally applicable to both complex resistivity and complex permittivity since both are relaxation transfer functions whose amplitude is a monotonically decreasing function of frequency. Once the expression for the transfer function is obtained using standard circuit impedance analysis techniques, we may if desired, obtain the conventional "complex permittivity" equivalent circuit for dielectric behavior by replacing all resistors with capacitors and all capacitors with resistors.

5. Relaxation models

All the mathematical models which meet our requirements of causality, stability, and relaxation share three main features concerning the amplitude of the transfer function. As illustrated by Figure 1 there is a low frequency asymptote, a dispersive region and a high frequency asymptote. The dispersive region can be considered as centered around a typical frequency or, alternatively, the step function response can be related to a particular time or time constant, τ. From the scaling property of Fourier transforms we know that a dispersion which occurs at low frequencies is characterized by a large time constant.

The asymptotic behavior of the amplitude can be described by two additional parameters. If the low frequency asymptote has the value R then the high frequency asymptote must have the value $R(1-m)$, where $0<m\leqq 1$, since the amplitude is a monotonically decreasing non-negative function. This dimensionless quantity, m, determines the discontinuity at the origin for the time domain response. It is readily shown from the initial and final value theorems for Laplace transforms [WAIT 1958, HALLOF 1963] that for a negative step function,

$$m = V_s/V_p, \tag{20}$$

where V_s is the output at $t=0^+$ and V_p is the output at $t=0^-$. SEIGEL [1959], in discussing the IP relaxation, gave the name "chargeability" to this fundamental parameter, and KELLER and FRISCHKNECHT [1966] stress its importance in the description of induced polarization behavior.

Cole—Cole family of models

There are several quite different mathematical models which have been proposed to describe resistivity and dielectric spectra. We have attempted in *Figure 3* to place these models in three major groups. Probably the most important group, and one we will discuss first, is the Cole—Cole family of models.

Cole—Cole model

The relaxation model having a transfer function with the form:

$$h(\omega) = R\left[1 - m\left(1 - \frac{1}{1+(i\omega\tau)^c}\right)\right] \tag{21}$$

was originally proposed by COLE and COLE [1941] to describe empirically the spectra of various observed dielectric data. In order to present their data Cole and Cole chose to represent the real and imaginary parts of the measured

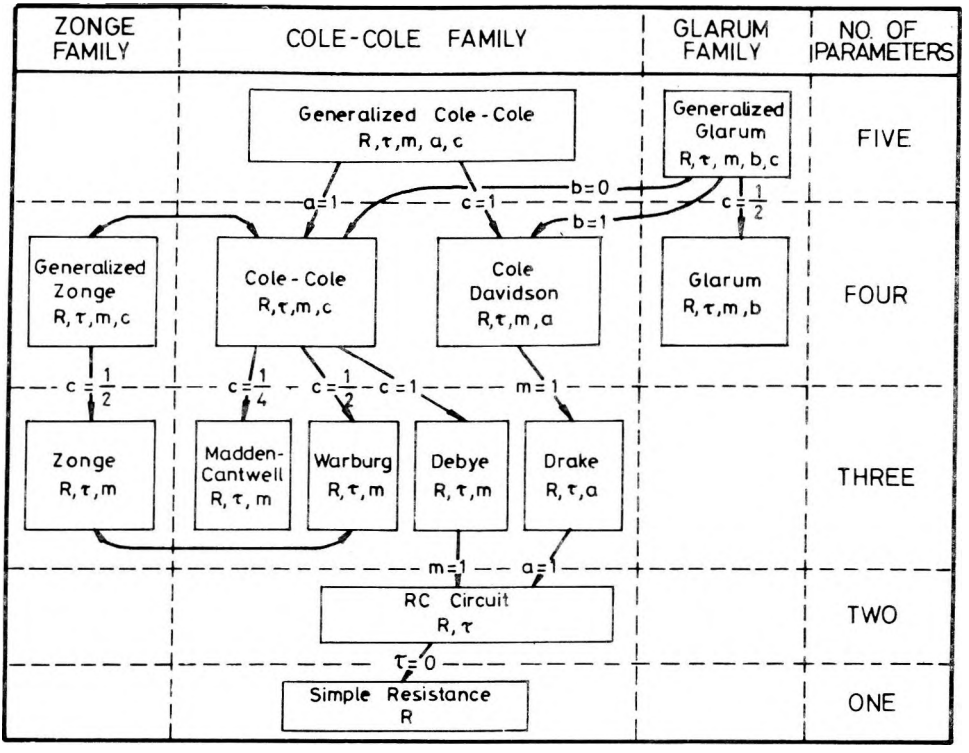

Fig. 3. Relationships between the different relaxation models

3. ábra. Összefüggések a különböző relaxációs modellek között

Рис. 3. Соотношения разных релаксационных моделей

transfer function at each frequency, by points in the complex plane. Such plots now bear their name and are extensively used to display dielectric data [DANIEL 1967, HILL et al. 1969]. The same method of presentation has been used by KATSUBE [1975] and ZONGE and WYNN [1975] to display complex resistivity data. With this method of presentation a Cole—Cole relaxation appears as circular arc with its center either on or below the real axis of the complex plane *(Figure 4)*.

An alternative method of presentation which we have tended to adopt in this paper, is to plot the amplitude and phase of the transfer function versus frequency on a double logarithmic scale. This type of plot strongly differentiates relaxations with small time constants from those with larger time constants. In addition, the asymptotic slopes of the phase lag provide very useful information on the type of relaxation and the frequency dependence of the relaxation. In this type of plot a Cole—Cole relaxation appears as a symmetrical phase angle

peak whose negative and positive asymptotic slopes are both exactly equal to the frequency dependence, c, given in (21). The frequency at which the phase angle peak occurs

$$f_p = \frac{1}{2\pi\tau(1-m)^{1/2c}}, \tag{22}$$

is inversely proportional to the time constant, τ. Thus if the time constant is large the peak occurs at low frequency. Several phase angle plots of the Cole—Cole model for $c = 0.25$, $\tau = 1/2\pi$ and various values of the chargeability,

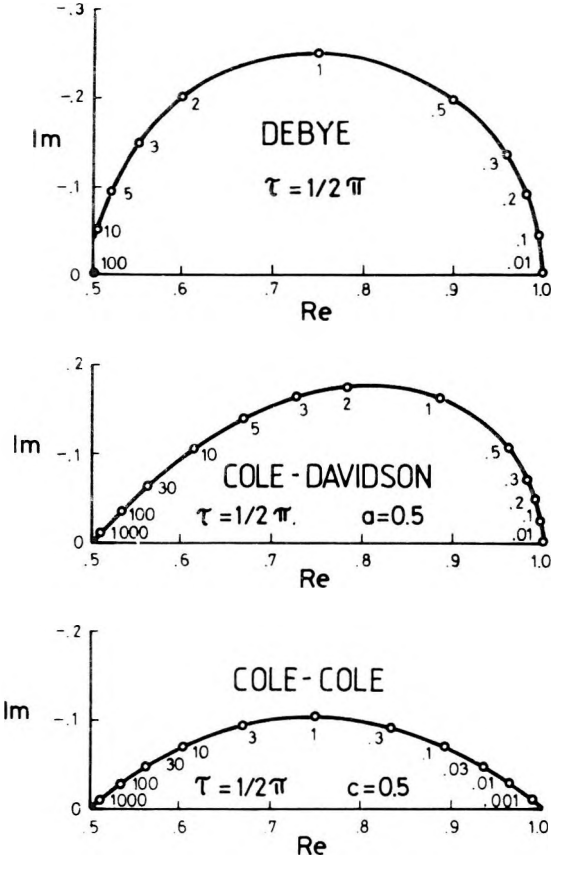

Fig. 4. Cole—Cole plots of three common relaxation models

4. ábra. Három általánosan használt relaxációs modell Cole—Cole diagramja

Рис. 4. Диаграмма Кол—Кол трех общеприменяемых релаксационных моделей

m, are shown in *Figure 5*. Increasing chargeability increases the phase angle. In the limit where $m = 1.0$, the phase angle levels off to an asymptote of $c\pi/2$. Almost all measured materials, however, have a chargeability less than 1.0 so that the phase angle plot shows at least one prominent peak.

The amplitude of the transfer function for the Cole—Cole model, when plotted on a double logarithmic scale, also exhibits symmetry, but in this case the symmetry is odd instead of even. Where the phase angle reaches a maximum, the amplitude has its maximum negative slope. At high frequency the amplitude has an asymptote of $R(1-m)$, whereas at low frequency the asymptote is simply R. In contrast, the phase angle depends only on m, τ and c, and is completely independent of R.

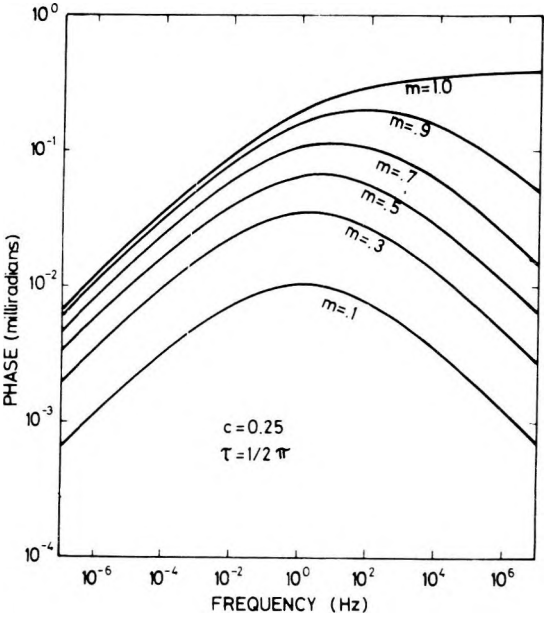

Fig. 5. Phase angle curves for a typical Cole—Cole model

5. ábra. Egy jellegzetes Cole—Cole modell fázisgörbéi

Рис. 5. Фазовая характеристика типической модели Кол—Кол

Although the Cole—Cole model was originally developed to aid in the analysis of dielectric phenomena, it has been found that complex resistivity measurements of mineralized rock in the laboratory [MADDEN and CANTWELL 1967] and in-situ [PELTON et al. 1977] closely conform to this relaxation model. Attempts to simulate electrical conduction in small sections of mineralized rock result in equivalent circuits which tend to resemble those in Figure 2 and, indeed, all of these circuits have Cole—Cole relaxation behavior.

Time domain behavior of the Cole—Cole model

Although perhaps most research into the complex resistivity of mineralized rocks is now being done in the frequency domain, much of the earlier research focussed on the IP decay, or measurements in the time domain. Since the IP decay was found to be slower than exponential [WAIT 1959, KELLER and FRISCHKNECHT 1966] several different mathematical formulations have been advanced to describe this decay, culminating in quite complex decay formulas appearing in the Russian literature [KOMAROV 1965]. Induced polarization measurements can be made in the time domain, but in order to determine accurately the true relaxational behavior, measurements must be closely spaced immediately after the start of the decay and must extend to large times. If measurements over several decades are desired, this necessitates a variable sampling rate. There are also additional computational difficulties introduced by a finite, instead of an infinite, charging time and by the finite time window required for each reading.

Measurements in the frequency domain, on the other hand, can be made reasonably easily over the eight decade range from 10^{-3} Hz to 10^{+5} Hz, and, as long as each measurement is made under steady state conditions, there are no comparable computational difficulties in the data analysis. Many such measurements have been made in the frequency domain and indicate that the Cole—Cole model often fits complex resistivity data very well. The question remains, however, what is the form of the Cole—Cole model in the time domain?

Assuming for the moment that $R = 1.0$, $m = 1.0$, and $\tau = 1.0$, the Cole—Cole transfer function is

$$h(\omega) = \frac{1}{1 + (i\omega)^c}. \tag{23}$$

Since $h(\omega)$ is the Fourier transform of the impulse response, $h(t)$, we will attempt an inverse Fourier transformation of

$$h(\omega) + (i\omega)^c h(\omega) = 1. \tag{24}$$

This can be accomplished easily only if $c = 1.0$, in which case

$$H(t) + D_t^1 \cdot H(t) = \delta(t) \tag{25}$$

is the transformed equation. We have used $\delta(t)$ to denote the delta function and D_t^1 to denote the operation of taking the first derivative with respect to time. It is now trivial to solve this differential equation for the natural response or impulse response of the system,

$$H(t) = e^{-t}. \tag{26}$$

However, for the Cole—Cole model in general, we have $0 < c \leqq 1$, thus the differential equation is

$$H(t) + D_t^c \cdot H(t) = \delta(t) \tag{27}$$

where D_t^c denotes the operation of taking a fractional derivative.

Although fractional derivatives are perhaps novel to the geophysical literature, they have a long history. Some of the more prominent investigators were Leibniz [1695], Euler [1730], Lagrange [1772], Laplace [1812], Fourier [1822], Abel [1823], Liouville [1832], De Morgan [1842], Riemann [1847], Heaviside [1892], Bromwich [1919], Erdélyi [1939], Courant [1961], and Oldham and Spanier [1974]. The last reference is a complete book on the subject of fractional derivatives and integrals, and it documents all the earlier references as well as many others which we will not attempt to include here.

The only property of the operator, D_t^c, which we require in this paper, is that

$$D_t^c \cdot \frac{t^k}{\Gamma(1+k)} = \frac{t^{k-c}}{\Gamma(1+k-c)} \tag{28}$$

where $\Gamma(x)$ is the gamma function and c is any real number, positive or negative (although we only use $0 < c \leqq 1$). Using this property and knowledge of the behavior of $1/\Gamma(1+x)$ we can immediately write down the solution to (27)

$$H(t) = \sum_{n=1}^{\infty} \frac{(-1)^{n+1} t^{-1+nc}}{\Gamma(nc)}. \tag{29}$$

The behavior of $1/\Gamma(1+x)$ is important, in that we must know where its first zero occurs. As shown in *Figure 6* this first zero occurs at $x = -1$, and is responsible for the fact that the first derivative of a constant is zero. That is,

$$D_t^c \cdot t^0 = 0, \tag{30}$$

when $c = 1$. In general, the derivative of a constant is

$$D_t^c \cdot t^0 = \frac{t^{-c}}{\Gamma(1-c)} \tag{31}$$

and, as shown in Figure 6, the result is equal to zero only when c is a positive integer.

We now readily see that

$$D_t^c \cdot \sum_{n=1}^{\infty} \frac{(-1)^{n+1} t^{-1+nc}}{\Gamma(nc)} = -\sum_{n=1}^{\infty} \frac{(-1)^{n+1} t^{-1+nc}}{\Gamma(nc)}. \tag{32}$$

In other words the operator maps each term into the next lower term (neglecting a sign change) except for the lowest term which becomes zero since $1/\Gamma(0) = 0$. Also, from (32) we see that (29) is the solution (within a multiplicative constant) of the homogeneous equation

$$H(t) + D_t^c \cdot H(t) = 0 \tag{33}$$

and is therefore the natural response or impulse response of the system.

To obtain the step function response we merely integrate each term in (29)

$$U(t) = \int_0^t h(\lambda)\, d\lambda = \sum_{n=1}^{\infty} \frac{(-1)^{n+1} t^{nc}}{\Gamma(1+nc)} \tag{34}$$

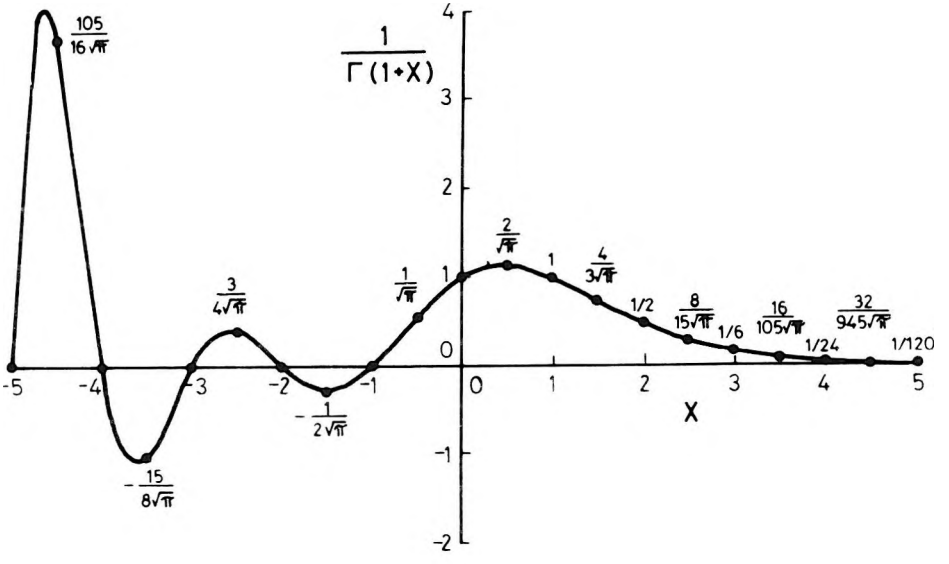

Fig. 6. Plot of $1/\Gamma(1+x)$

6. ábra. Az $1/\Gamma(1+x)$ függvény

Рис. 6. Функция $1/\Gamma(1+x)$

and subtract from 1.0 to obtain the step function decay

$$V(t) = 1 - U(t) = \sum_{n=0}^{\infty} \frac{(-1)^n t^{nc}}{\Gamma(1+nc)}. \tag{35}$$

We pause for a moment to inspect (35) and note that for $c = 1.0$

$$V(t) = \sum_{n=0}^{\infty} \frac{(-1)^n t^n}{\Gamma(1+n)} = e^{-t} \tag{36}$$

since $\Gamma(1+n) = n!$ The other special case for which the series corresponds to commonly known functions, is $c = 0.5$; then

$$V(t) = \sum_{n=0}^{\infty} \frac{(-1)^n t^{n/2}}{\Gamma(1+n/2)} = e^t \operatorname{erfc} t^{1/2}, \tag{37}$$

where erfc x denotes the complementary error function [ABRAMOWITZ and STEGUN 1972, p. 297].

The series in (35) is rapidly convergent for small t, but convergence is very poor for $c < 1.0$ and $t > 2\pi$. An approximate solution in this region for the particular case $c = 0.25$ has been obtained by MADDEN and CANTWELL [1967] but the derivation is approximate, lengthy, and limited to that particular case.

To obtain a general solution, we start again at the beginning and examine the Laplace transform form of (23),

$$h(s) = \frac{1}{1+s^c}. \tag{38}$$

For large t, frequency, and therefore s^c, is small; therefore we might consider expanding (38) as follows.

$$h(s) = 1 - s^c + s^{2c} - s^{3c} + \ldots \tag{39}$$

We cannot perform the inverse Laplace transform on this series conveniently so we divide by s to obtain the transform of the step function response

$$u(s) = \frac{h(s)}{s} = s^{-1} - s^{c-1} + s^{2c-1} - s^{3c-1} + \ldots \tag{40}$$

Now since

$$L^{-1}\{s^{-a}\} = \frac{t^{a-1}}{\Gamma(a)} \tag{41}$$

we might believe that, if an inverse Laplace transform for (40) exists, it is given by

$$U(t) = 1 - \frac{t^{-c}}{\Gamma(1-c)} + \frac{t^{-2c}}{\Gamma(1-2c)} - \frac{t^{-3c}}{\Gamma(1-3c)} + \ldots =$$

$$= 1 - \sum_{n=1}^{\infty} \frac{(-1)^{n+1} t^{-nc}}{\Gamma(1-nc)}, \tag{42}$$

and therefore,

$$V(t) = \sum_{n=1}^{\infty} \frac{(-1)^{n+1} t^{-nc}}{\Gamma(1-nc)} \tag{43}$$

This series does indeed converge for $t > 2\pi$ and we have used it along with (35) to construct the Cole—Cole decay curves for $c = 0.125$, $c = 0.25$, and $c = 0.5$ shown in *Figure 7*. The impulse response, $H(t)$, for $t > 2\pi$ may be derived simply by taking just the first derivative of (42)

$$H(t) = D_t^1 U(t) = \sum_{n=1}^{\infty} \frac{(-1)^n t^{-1-nc}}{\Gamma(-nc)}. \tag{44}$$

If we now return to the general expression for the Cole—Cole model (21) where we have not specified $R = 1.0$, $m = 1.0$, and $\tau = 1.0$, we can use the scaling property of the Fourier transform and our earlier considerations of discontinuities produced by m, to write down the general time domain forms

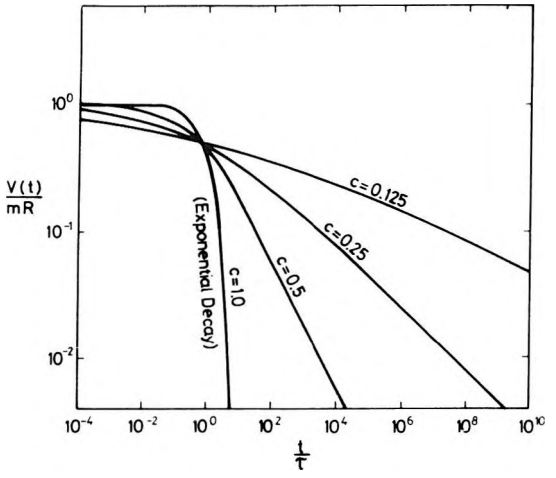

Fig. 7. Cole—Cole step function decay curves

7. ábra. Időtartománybeli Cole—Cole lecsengési görbék

Рис. 7. Кривые затухания Кол—Кол во временном диапазоне

$$H(t) = R\frac{m}{\tau}\sum_{n=1}^{\infty}\frac{(-1)^{n+1}\left(\frac{t}{\tau}\right)^{-1+nc}}{\Gamma(nc)} \tag{45}$$

$$U(t) = R\left[1 - m\sum_{n=1}^{\infty}\frac{(-1)^{n}\left(\frac{t}{\tau}\right)^{nc}}{\Gamma(1+nc)}\right] \tag{46}$$

$$V(t) = Rm\sum_{n=1}^{\infty}\frac{(-1)^{n}\left(\frac{t}{\tau}\right)^{nc}}{\Gamma(1+nc)} \tag{47}$$

for $0 < t/\tau \leqq 2\pi$, and

$$H(t) = R\frac{m}{\tau}\sum_{n=1}^{\infty}\frac{(-1)^{n}\left(\frac{t}{\tau}\right)^{-1-nc}}{\Gamma(-nc)} \tag{48}$$

$$U(t) = R\left[1 - m\sum_{n=1}^{\infty}\frac{(-1)^{n+1}\left(\frac{t}{\tau}\right)^{-nc}}{\Gamma(-nc)}\right] \tag{49}$$

$$V(t) = Rm\sum_{n=1}^{\infty}\frac{(-1)^{n+1}\left(\frac{t}{\tau}\right)^{-nc}}{\Gamma(1-nc)} \tag{50}$$

for $t/\tau > 2\pi$.

For very large t, only the first term containing t is important and the step function response asymptotes to

$$U(t) \sim R\left[1 - m\frac{\left(\frac{t}{\tau}\right)^{-c}}{\Gamma(1-c)}\right] \tag{51}$$

When $m = 1.0$, $\tau = 1/2\pi$ and $c = 1/4$, (51) becomes

$$U(t) \sim R\left[1 - \frac{t^{-1/4}}{1.94}\right] \tag{52}$$

which compares with the

$$U(t) \sim R\left[1 - \frac{t^{-1/4}}{1.78}\right] \tag{53}$$

obtained by MADDEN and CANTWELL [1967] after several approximations.

An important point to note, however, is that this asymptotic behavior is not reached until t/τ is very large. The approximation for the $c = 1/4$ decay,

$$V(t) = \frac{Rm\left(\frac{t}{\tau}\right)^{-1/4}}{\Gamma(1-1/4)}, \tag{54}$$

is not within 25% until $t > 100\tau$. Also important is the fact that the chargeability, m, is never exactly equal to 1.0 as assumed in the approximation by MADDEN and CANTWELL [1967]. For natural earth materials, and for typical field IP measurements, m is usually substantially less than 1.0.

The final, and perhaps most important point, is that the IP step function response is extremely long and drawn out. In-situ studies of mineralized rocks [PELTON et al. 1976] indicate that the response closely approximates a Cole—Cole relaxation with $c = 1/4$ and τ ranging from microseconds to hundreds of seconds. It is apparent from Figure 7 that for $t < \tau/2$ the IP response reaches less than 1/2 its true step function value. Thus the typical 2 second switching times used in conventional time domain IP measurements may result in decay curves which bear little resemblance to the true step function decay, particularly for rocks which have a long time constant. The effects of switching may be readily calculated by adding and subtracting the step function responses due to the positive and negative steps comprising the waveform. For an infinite series of steps, convergence can be hastened by averaging the result due to a positive starting step with that of a negative starting step.

The prominent deviations from the true step function decay response (calculated from a Cole—Cole model with $c = 0.5$) caused by the sequential switching or 50% duty cycle used in conventional time domain IP measurements are illustrated in *Figure 8/a*. Not only is the shape of decay curve distorted, but the observed chargeability,

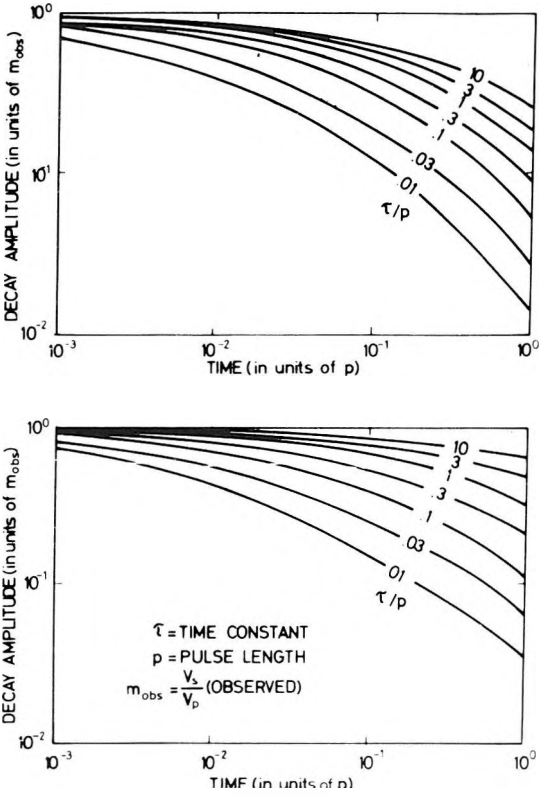

Fig. 8. Warburg model decay curves corrected for *a)* sequential switching; *b)* alternate switching

8. ábra. A Warburg-modell lecsengési görbéi *a)* a szokásos GP jelalakra korrigálva; *b)* pólusváltásos jelalakra korrigálva

Рис. 8. Кривые затухания модели Варбург *a)* Для обыкновенной формы сигнала ВП после исправления; *b)* Для формы сигнала с переменой полюса после исправления

$$m_{\text{obs}} = \frac{V_s}{V_p} \text{ (observed)}, \tag{55}$$

is much less than the true chargeability of the material, particularly when the ratio of the time constant to the pulse length is large *(Figure 9)*.

This reduction in the observed chargeability, although still appreciable, is substantially less for alternate switching or 100% duty cycle *(Figure 8/b)* as opposed to sequential switching. Also, since the switching is from positive directly to negative instead of positive to off, the primary voltage V_p is twice as large. As a result, the observed secondary voltage can be four times as large for alternate switching as for sequential switching. This combined with the fact that twice as many waveforms are measured in the same time period, presents a

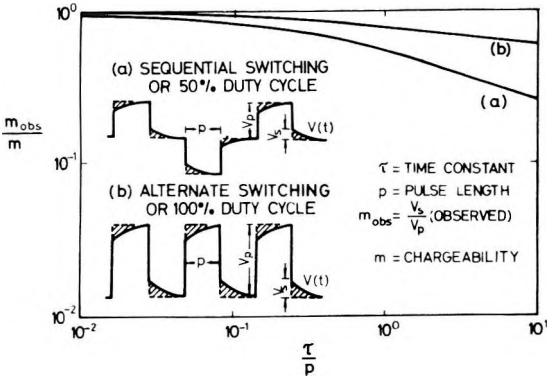

Fig. 9. Decrease in observed chargeability as a function of time constant

9. ábra. A mérhető töltethetőség csökkenése az időállandó függvényében

Рис. 9. Убывание измеряемой зарядимости в зависимости от постоянной времени

persuasive argument for using a 100% duty cycle. The main reason for use of a 50% duty cycle in the past, is that it is difficult to control precisely the transmitter waveform, thus measurements while the transmitter was always on (100% duty cycle) were often more inaccurate due to this additional source of noise.

Cole—Davidson model

The next member of the Cole—Cole family of models which we will discuss was proposed by DAVIDSON and COLE [1951] after a study of the dielectric properties of glycerine. They found that the imaginary versus real plot of $K(\omega)$ was not circular, but skewed as shown in Figure 4, and that the complex dielectric constant more closely fitted the model,

$$h(\omega) = R\left[1 - m\left(1 - \frac{1}{(1 + i\omega\tau)^a}\right)\right], \tag{56}$$

where $0 < a \leqq 1$.

A special case of this same relaxation model was discussed by VAN VOORHIS et al. [1973] in their analysis of in-situ complex resistivity data obtained over porphyry copper mineralization. When the chargeability, m, is equal to 1.0, (56) takes the form,

$$h(\omega) = \frac{R}{(1 + i\omega\tau)^a}, \tag{57}$$

which they have called the Drake model.

Time domain behavior of the Cole—Davidson model

Several difficulties become more obvious if the Drake model is used to describe IP behavior in the time domain. Since $m = 1.0$, it suggests that there is no discontinuity in the IP decay and that $V_s = V_p$. This does not agree with most time domain observations of the IP phenomena [KELLER and FRISCHKNECHT 1966, KOMAROV 1965, SAUCK and SUMNER 1967].

In addition, the low frequency and high frequency phase angle asymptotic slopes (on a double logarithmic plot) are $+1$ and $-a$, respectively. Thus we might expect that the Cole—Davidson decay will have behavior similar to that of a Cole—Cole model with frequency dependence $c = a$ for small t and $c = 1.0$ for large t. In other words, we might expect the Cole—Davidson decay to be approximately that of a negative exponential for large times. Again, this prediction is not in agreement with the majority of the time domain observations.

To solve for the behavior of the Cole—Davidson model in the time domain we assume for the moment that $R = 1.0$, $m = 1.0$ and $\tau = 1.0$; then the Laplace transform form of the transfer function given in (56) is

$$h(s) = \frac{1}{(1+s)^a} \tag{58}$$

and the inverse Laplace transform or impulse response of the system obtained from tables [KORN and KORN 1968, p. 917] is

$$H(t) = \frac{t^{a-1}e^{-t}}{\Gamma(a)}. \tag{59}$$

We now integrate to find that the step function response

$$U(t) = \frac{1}{\Gamma(a)} \int_0^t \lambda^{a-1} e^{-\lambda}\, d\lambda = \frac{\gamma(a, t)}{\Gamma(a)} \tag{60}$$

is expressed quite simply in terms of the incomplete gamma function, $\gamma(a, t)$. This expression may be evaluated from tables of the chi-square probability function, $P(\chi^2 \mid \nu)$, since

$$\frac{\gamma(a, t)}{\Gamma(a)} = P(2t \mid 2a), \tag{61}$$

[ABRAMOWITZ and STEGUN 1972, p. 914] or we can use the series expansion for $\gamma(a, t)$ [ABRAMOWITZ and STEGUN 1972, p. 262—263] to obtain

$$U(t) = e^{-t} \sum_{n=0}^{\infty} \frac{t^{a+n}}{\Gamma(a+n+1)} \tag{62}$$

and, for large t,

$$U(t) \sim 1 - \frac{t^{a-1}e^{-t}}{\Gamma(a)}\left[1 + \frac{a-1}{t} + \frac{(a-1)(a-2)}{t^2} + \ldots\right] \tag{63}$$

From (62) we see that

$$V(t) \sim 1 - \frac{t^a}{\Gamma(a+1)} \tag{64}$$

as $t \to 0$ and from (63) we see that

$$V(t) \sim \frac{t^{a-1}e^{-t}}{\Gamma(a)} \tag{65}$$

is dominated by negative exponential behavior as $t \to \infty$. Thus we were quite correct in our original expectation that for small t the Cole—Davidson decay would be similar to that of a Cole—Cole decay with frequency dependence, a, and that for large t the decay would be similar to that of a Cole—Cole model with $c = 1.0$ (i.e. a negative exponential decay).

As a final note we may discard our original assumption that $R = 1.0$, $m = 1.0$, and $\tau = 1.0$, to obtain the general time domain forms for $H(t)$, $U(t)$ and $V(t)$. This merely involves substitution of t/τ for t, incorporation of appropriate discontinuities introduced by the chargeability, and multiplication by R, after the same procedure used to obtain the general time domain forms for the Cole—Cole model.

Relationships within the Cole—Cole family

The reason that we have grouped the Cole—Cole and Cole—Davidson models together into one family is that there is one general model,

$$h(\omega) = R\left[1 - m\left(1 - \frac{1}{(1 + (i\omega\tau)^c)^a}\right)\right], \tag{66}$$

which includes both of the above as a special case. For lack of a better name, we call this model the generalized Cole—Cole relaxation. The model is asymmetric when displayed on a Cole—Cole plot or when presented as amplitude and phase on a double logarithmic frequency plot. Since the low and high frequency phase angle asymptotic slopes are $+c$ and $-ac$, respectively, we expect that for large t the step function decay for this model will be similar to that of a Cole—Cole model with frequency dependence, c, and that for small t the decay will be similar to that of a Cole—Cole model with frequency dependence, ac.

We may determine expressions for the time domain response of the generalized Cole—Cole model (when $R = 1.0$, $m = 1.0$, and $\tau = 1.0$) by applying the binomial expansion to

$$h(s) = (1 + s^c)^{-a} \tag{67}$$

for small s (large t), and to

$$h(s) = s^{-ca}(1+s^{-c})^{-a} \tag{68}$$

for large s (small t). The resulting decay expressions are

$$V(t) = 1 - \sum_{n=0}^{\infty} \frac{(-1)^n \Gamma(a+n) t^{c(a+n)}}{\Gamma(a)\Gamma(1+n)\Gamma(1+ca+cn)} \tag{69}$$

for small t, and

$$V(t) = \sum_{n=1}^{\infty} \frac{(-1)^{n+1} \Gamma(a+n) t^{-nc}}{\Gamma(a)\Gamma(1+n)\Gamma(1-nc)} \tag{70}$$

for large t.

As illustrated in Figure 3, the generalized Cole—Cole model becomes the Cole—Davidson model when $c=1$ and becomes the Cole—Cole model when $a=1$. We have already mentioned that the Drake model is the special case of the Cole—Davidson model when $m=1$. In addition, we have singled out three special cases of the Cole—Cole model. The case, $c=0.25$, we have called the Madden—Cantwell model after the investigations of MADDEN and CANTWELL [1967]. The case $c=0.5$ we have called the Warburg model after the $(i\omega)^{-1/2}$ behavior of the Warburg impedance. And finally, the case $c=1.0$ corresponds to the common Debye dielectric relaxation. The Debye model further reduces to the relaxation of a simple two-component RC circuit if $m=1$. Likewise, the Drake model reduces to the RC circuit if $a=1$. The ultimate simplification comes about as the time constant, τ, of the RC circuit goes to zero. The transfer function, $h(\omega)$, is then just a simple constant, R.

Glarum family of models

Another, quite different approach, was used by GLARUM [1960] to obtain a general model which results in Cole—Cole and Cole—Davidson relaxations as special cases. The defect diffusion model he proposed results in a distribution function,

$$A(k) = \frac{k\tau}{\pi(k\tau-b)^{1/2}(k\tau-b+1)}. \tag{71}$$

Since the distribution function $A(k)$ is just the inverse Laplace transform of the impulse response [SHUEY an JOHNSON 1973], we need to transform (71) once to get $H(t)$ and then once again to get $h(s)$. Finally, we substitute $i\omega$ for s and allow for arbitrary R and m to obtain the frequency domain response

$$h(\omega) = R\left[1 - m\left(1 - \frac{(b+i\omega\tau)^{1/2}+b}{(b+i\omega\tau)^{1/2}+b+i\omega\tau}\right)\right] \tag{72}$$

We now see that for $b=0$ (72) becomes the Cole—Cole model with $c=0.5$ and that for $b=1$ (72) becomes the Cole—Davidson model with $a=0.5$.

The same comparison may be made by first obtaining $A(k)$ for the Cole—Cole and Cole—Davidson models. To accomplish this we could inverse Laplace transform $h(s)$ to obtain $H(t)$ and then attempt to inverse Laplace transform $H(t)$ to obtain $A(k)$. However, the series forms we obtained for the Cole—Cole and Cole—Davidson impulse responses are not particularly simple expressions to inverse transform. An alternative method for obtaining $A(k)$ from $h(\omega)$ is described by SHUEY and JOHNSON [1973]. For our definition of the Fourier transform (Shuey and Johnson use the less common $+i$ transform), $A(k)$ is given by

$$A(k) = \frac{1}{\pi} \operatorname{Im}[h(-k)]. \tag{73}$$

In other words, we simply substitute $-k$ for $i\omega$ in $h(\omega)$ and take $1/\pi$ times the imaginary part. Proceeding in this manner, we obtain

$$\frac{A(k)}{mR} = \frac{\frac{1}{\pi} \sin \pi c}{(k\tau)^{-c} + 2 \cos \pi c + (k\tau)^{c}} \tag{74}$$

for the Cole—Cole model, and

$$\frac{A(k)}{mR} = \frac{\frac{1}{\pi} \sin \pi a}{(k\tau - 1)^{a}} \tag{75}$$

for the Cole—Davidson model.

Again we see that specifying $b=0$ in (71) results in a Cole—Cole model with $c=0.5$, and that choosing $b=1$ results in a Cole—Davidson model with $a=0.5$. This relationship among the distribution functions for the Cole—Cole, Cole—Davidson and Glarum models is perhaps more clearly illustrated in *Figure 10*, where we have plotted the various $A(k)/mR$ on a double logarithmic scale. In this plot the Cole—Cole distribution is symmetric about its center at $k=1/\tau$. Since a single Debye relaxation (corresponding to $e^{-t/\tau}$ decay in the time domain) would be represented on this plot by a delta function at $k=1/\tau$, we see that an alternate way of envisioning the Cole—Cole model is as a continuous distribution of Debye relaxations with varying time constants centered (on a logarithmic plot) at $k=1/\tau$. Thus the parameter, τ, which we have constantly used in referring to the Cole—Cole model takes on additional significance. It refers to the main relaxation time, when the Cole—Cole model is considered as a sum of Debye relaxations.

Similarly, we note that $A(k)$ is directly proportional to the chargeability parameter, m. Varying the magnitude of m does not change the shape of $A(k)$

(on a double logarithmic scale) it merely shifts the curve up or down, appropriately increasing or decreasing the contribution from all Debye components in unison. Thus we see that there was good reason for the original choice of m as a fundamental parameter describing the magnitude of the IP effect [SEIGEL 1959, KELLER and FRISCHKNECHT 1966].

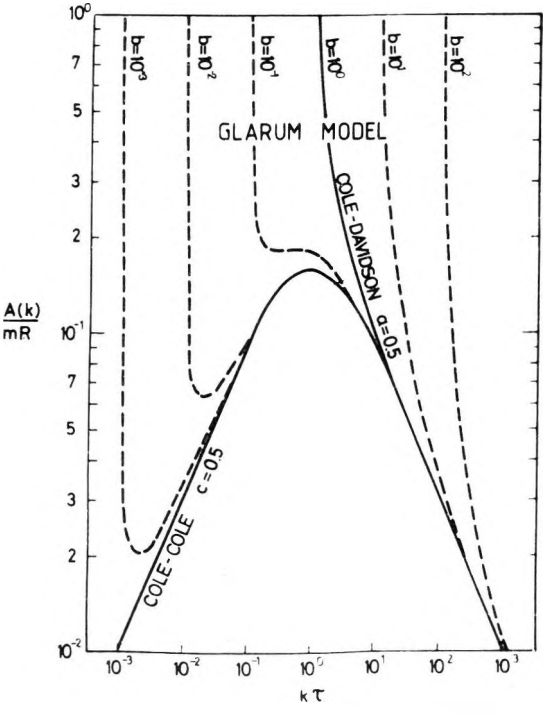

Fig. 10. Plots of the distribution function, $A(k)$, for the Glarum model

10. ábra. A Glarum-modell $A(k)$ eloszlásfüggvénye

Рис. 10. Функция распределения $A(k)$ для модели Гларум

The third parameter, c, of the Cole—Cole distribution, also plays an important role; it varies the width of the symmetric distribution. Low values of c characterize a very broad distribution, whereas high values characterize a sharp, peaked distribution. In the limit $c = 1$, the distribution is a delta function.

The Cole—Davidson distribution function is not symmetric. It has a singularity at $k = 1/\tau$ and is zero for $k < 1/\tau$. For large k (high frequency or short time) $A(k)$ has the same asymptotic behavior as that of the Cole—Cole model,

$$\frac{A(k)}{mR} \sim \frac{\frac{1}{\pi}\sin \pi a}{(k\tau)^a} \tag{76}$$

when $c = a$. This provides one additional route for arriving at our earlier conclusion that the time domain behavior for the Cole—Cole and Cole—Davidson models was the same for small t. Also, since $A(k)$ is zero for $k < 1/\tau$ we might expect Debye (or negative exponential) behavior in the time domain for large t, as again, we previously found.

The distribution function for the Glarum model, as we have seen in Figure 10, interpolates between that of a Cole—Cole distribution with $c=0.5$ and a Cole—Davidson distribution with $a=0.5$. Since $A(k)$ is zero for $k\tau<b$, one way of viewing a Glarum distribution with $b<1$, is as basically a Cole—Cole distribution which lacks relaxations having decay times longer than τ/b. When $b=1$ the Glarum distribution is exactly the same as that of a Cole—Davidson distribution with $a=0.5$. However, we can also have $b>1$. As b increases in magnitude the distribution becomes more sharply peaked and eventually tends to that of a Debye (delta function) distribution with a single relaxation time of τ/b.

Actually, this latter transition, between the Cole—Davidson distribution with $a=0.5$ and the Debye distribution ($a=1.0$) was the feature of the model of most interest to GLARUM [1960]. As long as one ignores both the extreme high frequency and low frequency behavior, it is possible to vary b so that the Glarum model behaves as an approximate Cole—Davidson model with arbitrary

$$a \cong \frac{b^{1/2}}{1+b^{1/2}}. \tag{77}$$

However, this relationship is exact only for $b=1$ and $b \gg 1$.

If we truly wish to have the Cole—Davidson model with arbitrary a as a special case of a more general model, we must modify (71) so that the distribution function becomes

$$\frac{A(k)}{mR} = \frac{\frac{1}{\pi}\sin \pi c}{(k\tau-b)^c[1+(1-b)(k\tau)^{-2c}(1+2(k\tau)^c \cos \pi c)]}. \tag{78}$$

Then, indeed, we see that (78) is equal to (74) when $b=0$, and equal to (75) when $b=1$. The $h(\omega)$ for this generalized Glarum model is simply

$$h(\omega) = \left[1-m\left(1-\frac{(b+i\omega\tau)^c+b}{(b+i\omega\tau)^c+(b+i\omega\tau)^{2c}}\right)\right] \tag{79}$$

and the impulse response (when $R=1.0$, $m=1.0$, and $\tau=1.0$) is

$$H(t) = e^{-bt}\left[b\frac{t^{c-1}}{\Gamma(c)}+(1-b)\sum_{n=1}^{\infty}\frac{(-1)^{n+1}t^{-1+nc}}{\Gamma(nc)}\right]. \tag{80}$$

Zonge family of models

The last group of relaxation models which we will attempt to discuss arises quite naturally from considering the impedance of transmission lines or infinite series of electrical components. One attempt to simulate the IP relaxation with a long series of resistors and capacitors is described by DOLAN [1967]. Another

approach by BRACEWELL [1965] demonstrates that analysis of the impedance of an infinite resistive—capacitive line (*Figure 11/a*) results in the diffusion equation and consequent Warburg impedance behavior.

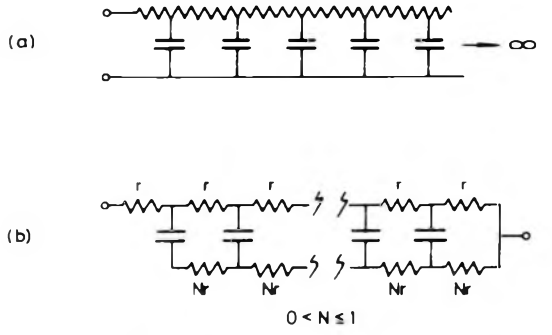

Fig. 11. Resistive—capacitive lines which produce
a) Warburg impedance response; *b)* Zonge model response

11. ábra. R—C vonalak
a) Warburg impedanciának megfelelő válaszfüggvénnyel; *b)* Zonge modellnek megfelelő valaszfüggvénnyel

Рис. 11. Линии R—C, которые дают ответ, соответствующий
a) импедансу Варбург; *b)* модели Зонг

The main relaxation model we will discuss here, however, arises from the impedance analysis by ZONGE [1972] of the transmission line shown in *Figure 11/b*. The impedance he obtains for this line has the form,

$$h(\omega) = R\left[1 - m\left(1 - \frac{\tanh \theta}{\theta}\right)\right], \tag{81}$$

where

$$R = h(0),$$

$$m = \frac{1}{1+N},$$

and

$$\theta = \left(i\omega C \frac{R}{m}\right)^{1/2}.$$

In an attempt to simulate the IP behavior of mineralized rocks he suggests that the capacitances in Figure 11/b be replaced by Warburg elements with impedance,

$$Z(\omega) = (i\omega X)^{-1/2}, \tag{82}$$

so that

$$\theta = \left((i\omega X)^{1/2} \frac{R}{m}\right)^{1/2}. \tag{83}$$

The resulting transfer function for $0 < m < 1$ has low and high frequency phase angle asymptotic slopes (on a double logarithmic plot) of $1/2$ and $-1/4$ respectively.

If we allow the elements to have arbitrary frequency dependence, c, then the expression for the impedance becomes

$$h(\omega) = R\left[1 - m\left(1 - \frac{\tanh\,(i\omega\tau)^{c/2}}{(i\omega\tau)^{c/2}}\right)\right], \tag{84}$$

where

$$\tau = X\left(\frac{R}{m}\right)^{1/c}. \tag{85}$$

A main characteristic of this general model is that the phase angle curves, on a double logarithmic frequency plot, are asymmetric and that the high frequency asymptotic slope is always $-1/2$ times the low frequency asymptotic slope.

In the time domain we would expect the generalized Zonge model to behave as a Cole—Cole model with frequency dependence, c, for large t, and as a Cole—Cole model with frequency dependence, $c/2$ for small t. The actual time domain expression for the generalized Zonge model (when $R = 1.0$, $m = 1.0$, and $\tau = 1.0$) may be obtained from

$$u(s) = \frac{\tanh\, s^c}{s^{c+1}} \tag{85}$$

by using the series expansion for the hyperbolic tangent [ABRAMOWITZ and STEGUN 1972, p. 85], and inverse transforming term by term. We obtain, for small t,

$$U(t) = \sum_{n=1}^{\infty} \frac{2^{2n}(2^{2n}-1)B_{2n}t^{-2(n-1)c}}{\Gamma(1+2n)\Gamma(1-2(n-1)c)}, \tag{87}$$

where B_k is the k^{th} Bernoulli number [ABRAMOWITZ and STEGUN 1972, p. 810].

6. Discussion of the forward problem

We now conclude our consideration of the forward problem formulation for electrical relaxation in rocks. We have perhaps accomplished the first three of the five main objectives of this paper, namely 1) to summarize the essential features of mathematical models which may be considered appropriate for complex resistivity and dielectric relaxation, 2) to examine both the frequency domain and time domain behavior of various proposed models, and 3) to investigate the relationships between the models. The list of relaxation models we have considered is by no means exhaustive, but we have dealt with many of the proposed models which have relatively simple behavior in the frequency and

time domains. In addition, we have generalized three of the models so that they have flexibility to describe a wide range of relaxational behavior.

As shown in Figure 3 all three generalized models are related to the simple Cole—Cole model, and may be distinguished from the Cole—Cole model only by asymmetry in the phase angle peak. As we will attempt to show in the second part of this paper, it is difficult enough, even with measurements over eight decades of frequency, to determine confidently the fundamental parameters characterizing the location, width and magnitude of the peak, let alone any additional parameters describing slight asymmetry in the peak. These slight differences are difficult to detect mainly because many observed spectra have additional relaxations occurring at higher or lower frequency which obscure at least one of the phase angle asymptotes. As a result, it is usually not feasible to resolve models much more complex than the Cole—Cole model, and thus the Cole—Cole model, by default, is very often used to describe complex resistivity and dielectric data.

For ease of reference in the latter part of this paper, we have summarized and numbered in *Table 1* the relaxation models that we have discussed. As well as providing the formula for $h(\omega)$ in the table we have also given the phase angle asymptotic slopes. When compared with those of the appropriate Cole—Cole model these slopes predict the asymptotic time domain behavior of the models. More accurate comparison of time domain data with theoretical relaxation models requires consideration of the transmitter switching history and compensation for effects introduced by the finite time window used in sampling the receiver voltage.

Table I

SIMPLE RELAXATION MODELS			LOG Φ ASYMPTOTIC SLOPES	
NO.	NAME	$h(\omega)$	$\omega \to 0$	$\omega \to \infty$
0	Simple Resistance	R	0	0
1	RC Circuit	$R\left[\frac{1}{1+i\omega\tau}\right]$	1	0
2	Drake	$R\left[\frac{1}{1+i\omega\tau}\right]^a$	1	0
3	Debye	$R\left[1-m\left(1-\frac{1}{1+i\omega\tau}\right)\right]$	1	-1
4	Warburg	$R\left[1-m\left(1-\frac{1}{1+(i\omega\tau)^{1/2}}\right)\right]$	1/2	$-1/2$
5	Madden—Cantwell	$R\left[1-m\left(1-\frac{1}{1+(i\omega\tau)^{1/4}}\right)\right]$	1/4	$-1/4$
6	Zonge	$R\left[1-m\left(1-\frac{\tanh(i\omega\tau)^{1/4}}{(i\omega\tau)^{1/4}}\right)\right]$	1/2	$-1/4$
7	Generalized Zonge	$R\left[1-m\left(1-\frac{\tanh(i\omega\tau)^{c/2}}{(i\omega\tau)^{c/2}}\right)\right]$	c	$-c/2$
8	Cole—Cole	$R\left[1-m\left(1-\frac{1}{1+(i\omega\tau)^c}\right)\right]$	c	$-c$
9	Cole—Davidson	$R\left[1-m\left(1-\frac{1}{(1+i\omega\tau)^a}\right)\right]$	1	$-a$
10	Generalized Cole—Cole	$R\left[1-m\left(1-\frac{1}{(1+(i\omega\tau)^c)^a}\right)\right]$	c	$-ac$
11	Glarum	$R\left[1-m\left(1-\frac{(b+i\omega\tau)^{1/2}+b}{(b+i\omega\tau)^{1/2}+b+i\omega\tau}\right)\right]$	1	$-1/2$
12	Generalized Glarum	$R\left[1-m\left(1-\frac{(b+i\omega\tau)^c+b}{(b+i\omega\tau)^c+(b+i\omega\tau)^{2c}}\right)\right]$	1	$-c$

1. táblázat. Egyszerű relaxációs modellek

Таблица 1. Простые релаксационные модели

REFERENCES

ABRAMOWITZ M., and STEGUN I. A. 1972: Handbook of mathematical functions. New York, Dover Publications, Inc., 1045. p.

BRACEWELL R. 1965: The Fourier transform and its applications. New York, McGraw-Hill Book Co., Inc., 381. p.

COLE K. S., COLE R. H. 1941: Dispersion and absorption in dielectrics. J. Chem. Phys., **9,** pp. 341—351.

DANIEL V. V. 1967: Dielectric relaxation. New York, Academic Press, 281. p.

DAVIDSON D. W., COLE R. H. 1950: Dielectric relaxation in glycerine. J. Chem. Phys., **18,** p. 1417

DOLAN W. M. 1967. Considerations concerning measurement standards and design of pulsed IP equipment — part I, in Proceedings of the symposium on induced electrical polarization. University of California at Berkeley, pp. 2—16

FULLER B. D., WARD S. H. 1970: Linear system description of the electrical parameters of rocks. IEEE Trans. Geoscience Electronics, GE—**8**, pp. 7—18

FRASER D. C., KEEVIL N. B. JR., WARD S. H. 1964: Conductivity spectra of rocks from the Craigmont ore environment. Geophysics, **29,** pp. 832—847

GLARUM S. H. 1960: Dielectric relaxation of isoamyl bromide. J. Chem. Phys., **33,** 3, pp. 639—643

GRISSEMAN C. 1971: Examination of the frequency dependent conductivity of ore-containing rock on artificial models. Scientific Report No. 2, Electronics Laboratory, University of Innsbruck, Austria

HALLOF P. G. 1963: A study of the usefulness of the various parameters employed in the variable frequency IP method. Paper presented at the 33rd Annual International SEG Meeting in New Orleans, Louisiana

HALLOF P. G. 1974: The IP phase measurement and inductive coupling. Geophysics, **39,** pp. 650—665

HILL N. E., VAUGHAN W. E., PRICE A. H., DAVIES M. 1969: Dielectric properties and molecular behavior. New York, Van Nostrand Reinhold Co., 480. p.

KATSUBE T. J. 1975: Electrical characteristics of serpentinites. Paper presented at the 45th Annual International SEG Meeting, October 13, in Denver, Colorado

KELLER G. V., FRISCHKNECHT F. C. 1966: Electrical methods in geophysical prospecting. New York, Pergamon Press, 517. p.

KOMAROV V. A. 1965: Time characteristics of induced polarization. Methods and Technology of Prospecting, No. 43, VITR

KORN G. A., KORN T. M. 1968: Mathematical handbook for scientists and engineers. New York, McGraw-Hill Book Co., Inc., 1130. p.

MADDEN T. R., CANTWELL T. 1967: Induced polarization, a review, in Mining Geophysics, Vol. II. Tulsa, SEG, pp. 373—400

OLDHAM K. B., SPANIER J. 1974: The fractional calculus. New York, Academic Press, 234. p.

OLHOEFT G. R., FRISILLO A. L., STRANGWAY D. W. 1974: Electrical properties of lunar soil sample 15301, 38. Jour. Geophysical Res., **79,** pp. 1599—1604

PAPOULIS A. 1962: The Fourier integral and its applications. McGraw-Hill Book Co., 318. p.

PELTON W. H., SMITH R. J., HALLOF P. G. 1973: Parameters to describe second-order IP effects in the frequency domain. Toronto, McPhar Geophysics, Ltd., 21. p.

PELTON W. H., WARD S. H., HALLOF P. G., SILL W. R., NELSON P. H. 1976: In-situ complex resistivity studies of North-American mineral deposits. Paper presented at the 46th Annual International SEG Meeting, October 26, in Houston, Texas

PELTON W. H., WARD S. H., HALLOF P. G., SILL W. R., NELSON P. H. 1978: Mineral discrimination and removal of inductive coupling with multifrequency IP. Geophysics, **43,** pp. 588—609

SAINT-AMANT M., STRANGWAY D. W. 1970: Dielectric properties of dry, geologic materials. Geophysics, **35,** pp. 624—645

SAUCK W. A., SUMNER J. S. F. 1967: Laboratory experiments in induced polarization. Paper presented at the 37th Annual International SEG Meeting, November 1, in Oklahoma City, Oklahoma

SEIGEL H. O. 1959: Mathematical formulation and type curves for induced polarization. Geophysics, **24,** pp. 547—565

Shuey R. T., Johnson M. 1973: On the phenomenology of electrical relaxation in rocks. Geophysics, **38,** pp. 37—48
Sill W. R., Dewitt G. W. 1976: Parametric studies of IP spectra. Paper presented at the 46th Annual International SEG Meeting, October 26, in Houston, Texas
Van Voorhis G. D., Nelson P. H., Drake T. L. 1973: Complex resistivity spectra of porphyry copper mineralization. Geophysics, **38,** pp. 49—60
Wait J. R. 1958: Discussion on "A theoretical study of induced electrical polarization". Geophysics, **23,** pp. 144—153
Wait J. R. 1959: Overvoltage research and geophysical applications. New York, Pergamon Press, 158. p.
Wynn J. C., Zonge K. L. 1975: EM coupling, its intrinsic value, its removal and the cultural coupling problem. Geophysics, **40,** 5, pp. 831—851
Zonge K. L. 1972: Electrical properties of rocks as applied to geophysical prospecting. Ph. D. thesis, University of Arizona, 156. p.
Zonge K. L., Wynn J. C. 1975: Recent advances and applications in complex resistivity measurements. Geophysics, **40,** pp. 851—864

KOMPLEX ELLENÁLLÁS- ÉS DIELEKTROMOS ADATOK ÉRTELMEZÉSE — I. RÉSZ

W. H. PELTON, W. R. SILL, B. D. SMITH

A dielektromos spektrumok és a komplex ellenállás spektrumok között szoros kapcsolatot teremt az általános relaxációs elmélet. A gerjesztett polarizáció vagy a dielektromos jelenség leírására javasolt sok egyszerű modellt három relaxációs „családba" lehet osztani. A legáltalánosabb relaxációs modellek közül néhánynak megvizsgáltuk a viselkedését a frekvencia, idő és eloszlási függvény tartományban.

A modellek csoportokba rendezésének és a különböző modellek közti összefüggések vizsgálatának eredményeképp három általánosított kifejezéshez jutottunk, amelyek a relaxációs viselkedés igen széles tartományát írják le. Gyakran azonban nem lehet az általánosabb modell valamennyi paraméterét meghatározni a mért adatokból. Leghasználhatóbbnak az egyszerű Cole—Cole modellt találtuk, amely egy szimmetrikus csúcsot ad, ha a fázis logaritmusát ábrázoljuk a frekvencia logaritmusának függvényében, vagy pedig egy szimmetrikus „púpot", ha az átviteli függvény valós részét ábrázoljuk a képzetes rész függvényében.

ИНТЕРПРЕТАЦИЯ ДАННЫХ О КОМПЛЕКСНЫХ СПЕКТРАХ СОПРОТИВЛЕНИЯ И ДИЭЛЕКТРИЧЕСКИХ СПЕКТРАХ ЧАСТЬ I

В. Г. ПЕЛТОН, В. Р. СИЛ, Б. Д. СМИТ

Теория общей релаксации создает тесную связь между диэлектрическими спектрами и комплексными спектрами сопротивления. Много простых моделей, предлагаемых для описания вызванной поляризации или диэлектрического явления, могут быть разделены на три «семейства» релаксации. Из наиболее общих моделей релаксации поведение некоторых было изучено в диапазонах частоты, времени и функции распределения.

В результате организации моделей в группах и изучения отношений между разными моделями были получены три обобщенных выражения, которые описывают очень широкий диапазон релаксационного поведения. По замеренным данным, однако, часто нельзя определять все параметры общей модели. Самой полезной нашлась простая модель Кол-Кол, которая дает симметричный пик, если логарифм фазы изображается в зависимости от логарифма частоты, или симметричных «горбик», если истинная часть функции передачи изображается в зависимости от мнимой части.

GEOPHYSICAL TRANSACTIONS 1983
Vol. 29. No. 4. pp. 331—344

POSSIBILITIES OF THE FOCUSED-FIELD SURFACE GEOELECTRIC METHOD

Pál EGERSZEGI*

The paper investigates the possible applications of the focused-field method. It is shown that, with some restrictions, the method can be used for the detection of tectonic disturbances from the surface, for a more accurate determination of the specific resistivity of the basement and for obtaining almost distortion-free sounding curves in geologically disturbed areas. In mines the focused-field method should be utilized with appropriate modifications.

d: geoelectric methods, mining geophysics, resistivity measurements

1. Introduction

In 1962 the Geophysical Department of the Technical University of Heavy Industry and the Hungarian Oil and Gas Trust filed a patent on the application of the focused current well logging technique on the surface and in mines. The theoretical foundations of the method were reported by CSÓKÁS [1963], the possible fields of application by the present author [1965, 1967, 1980, 1982]. This article, based on the results of the investigations to date, gives a summarized evaluation of the application of the method on the surface and in mines.

2. Focused-current sounding

The focused-field method is based on the principle of the Laterolog 7[*] of borehole geophysics; that is, it applies a focusing electric circuit besides the measuring circuit to ensure that the measuring current should propagate perpendicularly to the surface down to a depth depending on the electrode spread. The penetration depth of the geoelectric method is thus increased. In the focusing circuit the current strength is adjusted by means of the "guard" electrodes M and M', placed in the close vicinity of the current electrode A_0 in the centre of the spread. The strength of the focusing current should be changed until the potential difference between electrodes M, M' becomes zero. The focusing current is introduced symmetrically with respect to electrode A_0 at two or more sides. As an example, *Fig. 1* shows an arrangement with four focusing electrodes.

[*] Trademark of Schlumberger Ltd

* Borsod Coal Mines, Miskolc, Kazinczy utca 19. H-3525, Hungary
Manuscript received: June 6, 1983

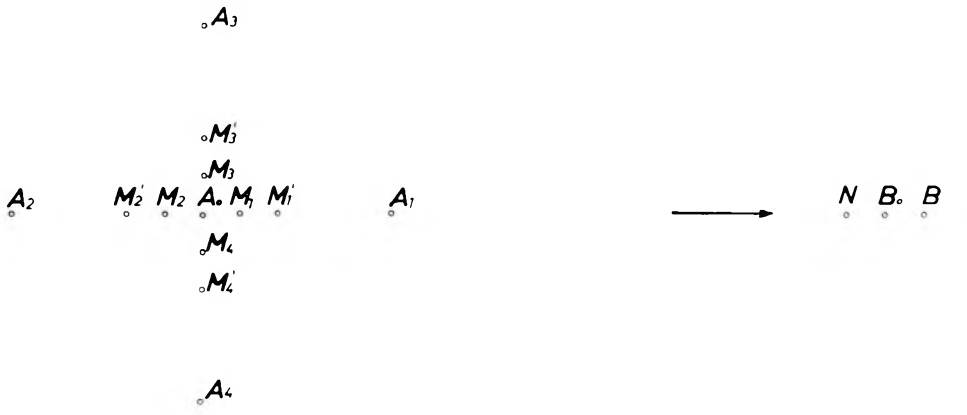

Fig. 1. Electrode arrangement with four focusing electrodes (A_1, A_2, A_3, A_4)

1. ábra. Négyterelős elektróda-elrendezés

Рис. 1. Установка электродов с четырьмя фокусирующими электродами

The execution of the measurement requires special instrumentation. The focusing- and measuring currents, which have identical signal form, frequency and phase, are provided by two low-frequency current generators.

The measuring unit contains, besides the measuring amplifiers, a control amplifier which can reduce to practically nil the voltage difference across the electrode pair MM' by adjusting the focusing current.

During measurements the symmetry should always be ensured, that is, the contact resistances of the 2 or 4 electrodes should be equal. This can be achieved by the proper driving in of the electrodes and by changing a resistance connected in series.

Either the measurements are performed with short-circuited guard electrodes M, M' when we determine a single specific resistivity with a given adjustment of the focusing current, or we separately set in four directions the zero potential difference between the guard electrodes M, M' and obtain four values for the focusing current and four corresponding values for the specific resistivity. In the latter case, the determination of the proper values of the focusing current and of the specific resistivity should be carried out as described in Section 4.

If in focused-current sounding the guard electrodes M and M' are short-circuited, the measuring current "beam" perpendicular to the surface will apparently be symmetric. In reality, this "beam" will no longer be symmetric if there occurs any lateral resistivity change within a circle of radius $2\overline{A_0A}$. Indeed, in this case we had to use in each direction focused currents of different strengths in order to provide the zero potential difference between the guard electrodes. Instead of this we apply only an average focusing field strength because of the

short-circuited guard electrodes, i.e. the measuring "current beam" is left asymmetric.

Upon inspecting the equation of apparent specific resistivity

$$\frac{R_a}{R_1} = C[U_{A_0M} + \eta_i(U_{A_1M} + U_{A_2M})], \tag{1}$$

where U is the potential at measuring electrode M due to the respective current electrode, η_i the focused current ratio in the inhomogeneous half-space (the quotient of the strength of the focusing current and of the measuring current), R_1 the specific resistivity of the upper layer and C is a constant, we find that the value of the measured specific resistivity strongly depends on the value of η_i.

The value η_h computed for homogeneous half-space, and the effect of the resistivity contrasts on η_i, strongly depend on the so-called spread quotient (n)

$$n = \frac{A_0A}{A_0O}$$

where O denotes the midpoint between the guard electrodes. With increasing values of n, η_h increases, and similarly increases the critical depth for which the density of the measuring current becomes negligibly small, i.e. "penetration" increases. At the same time, the change of the measuring current density with depth has a relative extremum, this results in a maximum in the η_i function for a focused-current sounding and, consequently, the sounding curve becomes more complex. As an example, we present two sounding curves with two focusing electrodes, fot the two-layer case; for $k = 1.0$ and $k = -0.98$, respectively

(Fig. 2). (Here $k = \frac{R_2 - R_1}{R_2 + R_1}$ where R_1, R_2 are the resistivities of the upper and lower layers, respectively.)

Processing of the measured data can be done in two ways. In the computation of the apparent specific resistivity

$$R_a = K\frac{U_{A_0M}}{I_0} \tag{2}$$

the value of K is

— either computed from η_h referring to the homogeneous half-space; in this case we get a curve (R_a) that is highly sensitive to any changes;
— or it is computed from η_i corresponding to the inhomogeneous half-space, which results in a nicely smoothed but less sensitive R_a curve; in its interpretation the η_i curve should be taken into consideration *(Fig. 3.)*.

Figure 4 shows a field a sounding curve computed by the second method. For the sake of comparison the curve measured by the gradient arrangement is also plotted.

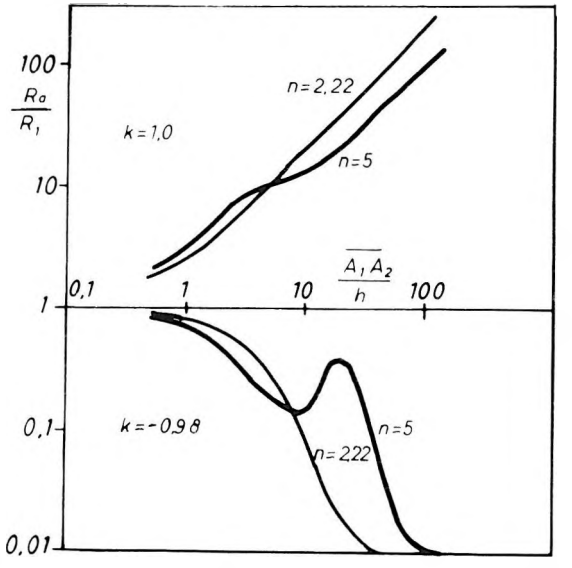

Fig. 2. Theoretical sounding curves for two focusing electrodes

2. ábra. Kétterelős elméleti szondázási görbék

Рис. 2. Теоретические кривые зондирования с двумя фокусирующими электродами

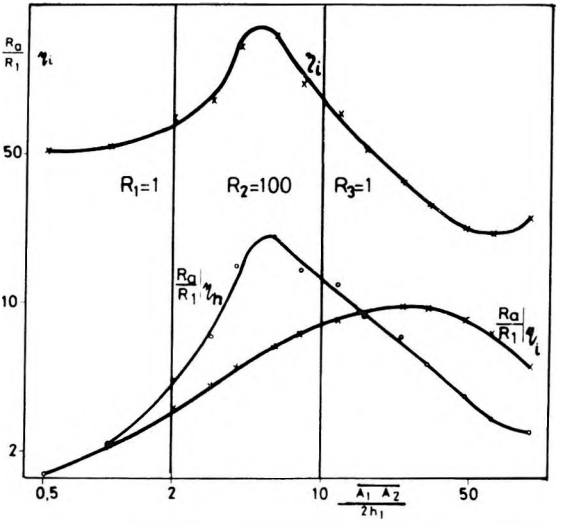

Fig. 3. Dependence of focused-field curves on the method of computation of configurational factor *K*. (Research Report of the Geophysical Dept. of the University of Heavy Industries, Miskolc, Hungary)

3. ábra. Terelő áramú görbék lefutása a *K* konfigurációs faktor számításától függően (NME Geofizikai Tanszék, Miskolc kutatási jelentése)

Рис. 3. Зависимость формы кривых фокусированного поля от способа вычисления фактора конфигурации *K* (По отчету об исследованиях Кафедры геофизики Технического университета по тяжелой промышленности, г. Мишкольц, ВНР)

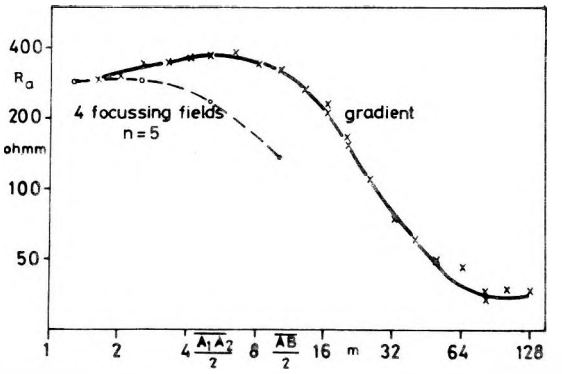

Fig. 4. A recorded 4-focusing-electrode sounding curve. (Research Report of the Geophysical Dept. of the University of Heavy Industries, Miskolc, Hungary)

4. ábra. Terepen mért 4-terelös szondázási görbe (NME Geofizikai Tanszék, Miskolc kutatási jelentése)

Рис. 4. Зарегистрированная в полевых условиях кривая зондирования с четырьмя фокусирующими электродами (По отчету об исследованиях Кафедры геофизики Технического университета по тяжелой промышленности, г. Мишколц, ВНР)

In the focused-field sounding method three basic points should be kept in mind for the proper selection of the spread quotient and of the number of electrodes:

— "penetration" should be maximum;
— interpretation of the sounding curves should be as simple as possible;
— the effect of the lateral resisitivity changes should be minimized.

3. Study of "penetration"

In the study of "penetration" we have made use of the results of ROY and APPARAO [1971] and SZARANIEC [1971]. ROY and APPARAO defined the "depth of penetration" as that particular depth wherefrom a thin horizontal layer exerts a maximal effect on the signal measured at the surface. SZARANIEC [1971] introduced the concept of "effective spread length": in the two-layered case with a resistivity contrast $k = +1.0$ or $k \sim -1.0$ this can be expressed as the ratio of the depth of the layer boundary to the spread length, taken at the intersection of the tangent to the steep part of the curve with the straight line $R_a/R_1 = 1$.

For some widely used arrangements *(Fig. 5)* these quantities are compiled in *Table I* and *II*.

From the point of view of penetration, the arrangement with four focusing electrodes of great spread quotient is advantageous. At the same time, if we study the behaviour of the sounding curves, the arrangement with two focusing electrodes and of spread quotient $n = 2.22$ seems to be the most appropriate [EGERSZEGI 1980]. In this latter arrangement for positive resistivity contrasts the "penetration" is four times as much as for the gradient arrangement, while the shape of the curves is the same as in a gradient arrangement.

Table I.

Arrangement	Wenner	Gradient	Potential	Modified unipole	2-focusing-electrode $n=5$
Penetration depth	$0.11AB$	$0.125AB$	$0.35AM$	$0.175A_1A_2$	$0.135A_1A_2$

Table II.

Arrangement		Wenner	Gradient	Potential	Modified unipole	2-focusing-electrode		4-focusing-electrode	
						$n=2.22$	$n=5$	$n=2.22$	$n=5$
Effective spread length	$k=1$	$0.47AB$	$0.5AB$	$5.7AM$	$2.85A_1A_2$	left $2.1A_1A_2$	$2.8A_1A_2$	left $2.1A_1A_2$	$2.8A_1A_2$
						right $2.1A_1A_2$	$1.1A_1A_2$	right $5.7A_1A_2$	$8.5A_1A_2$
	$k=-0.98$	$0.25AB$	$0.3AB$	$1.0AM$	$0.5A_1A_2$	left $\sim 0.3A_1A_2$	$\sim 0.43A_1A_2$	left $\sim 0.42A_1A_2$	$\sim 0.56A_1A_2$
						right $\sim 0.3A_1A_2$	$\sim 0.06A_1A_2$	right $\sim 0.42A_1A_2$	$\sim 0.06A_1A_2$

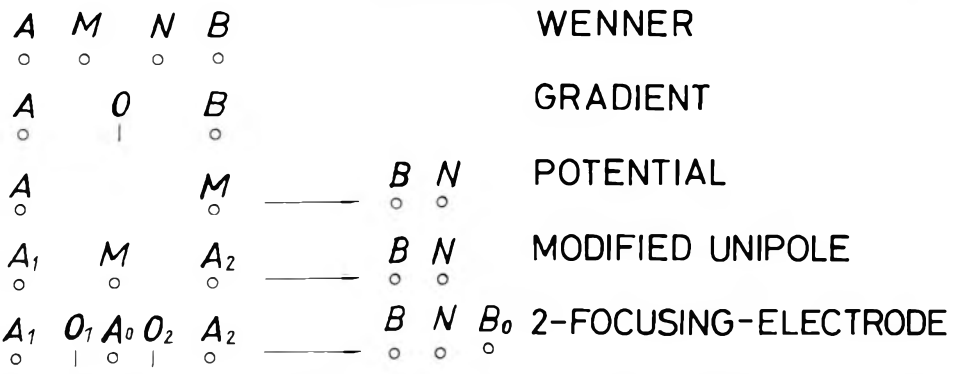

Fig. 5. Electrode arrangements *5. ábra.* Elektróda-elrendezések *Рис. 5.* Установки электродов

In the case of a positive resistivity contrast the focused-current sounding has a further advantage over the gradient arrangement: it yields a fair resolution even for contrasts as high as $R_2/R_1 > 100$; that is, it differentiates between the different high resistivity basement formations [EGERSZEGI 1980].

All the advantages listed in favour of the focused-current sounding also apply to the potential arrangement: it has a great "penetration" and a high resolution power for large positive resistivity contrasts.

4. Study of the "lateral effect"

As already mentioned, the focused-field sounding method is very sensitive to the lateral resistivity changes within a circle of radius $2\overline{AA_0}$ [EGERSZEGI 1965]. This effect can most easily be demonstrated by a 4-focusing-electrode arrangement if we do not short-circuit the guard electrodes and separately satisfy the condition $\Delta U = 0$ in the different directions. In the case of a lateral effect, the condition $\Delta U = 0$ is satisfied for different η_i values in different directions, as illustrated in *Fig. 6* for the arrangement shown in *Fig. 7*.

During the computations we changed the value of the spread quotient n, the distance d of the centre of the spread from the boundary of contrast $k = 0.9$, and the value of φ; that is, the angle made by the direction through the guard electrodes and the normal of the contrast boundary (Fig. 7).

The general relationship reads as

$$\eta(\varphi) = \frac{f_1(n, n') + kpf_2(n, n', p, \varphi)}{f_3(n, n') + kpf_4(n, n', p, \varphi)} \tag{3}$$

where $p = \overline{A_0A}/d$, the functions f_1 and f_3 refer to the homogeneous half-space,

$$\eta_h = \frac{f_1(n, n')}{f_3(n, n')} \tag{4}$$

while the functions f_2 and f_4 are the changes due to the inhomogeneity. Functions f_2 and f_4 assume both positive and negative values with changing φ. The

equation implies that this change has the greater amplitude, the greater the value of k. The curves of Fig. 6 however, imply that the amplitude also increases with increasing values of p and n. These considerations show, similarly to above, that in order to reduce the lateral effect one should use an arrangement of small spread quotient ($n = 2.22$) in the case of focused-current measurements. Distortions due to the lateral effect cannot be checked unless an arrangement of four focusing electrodes is used.

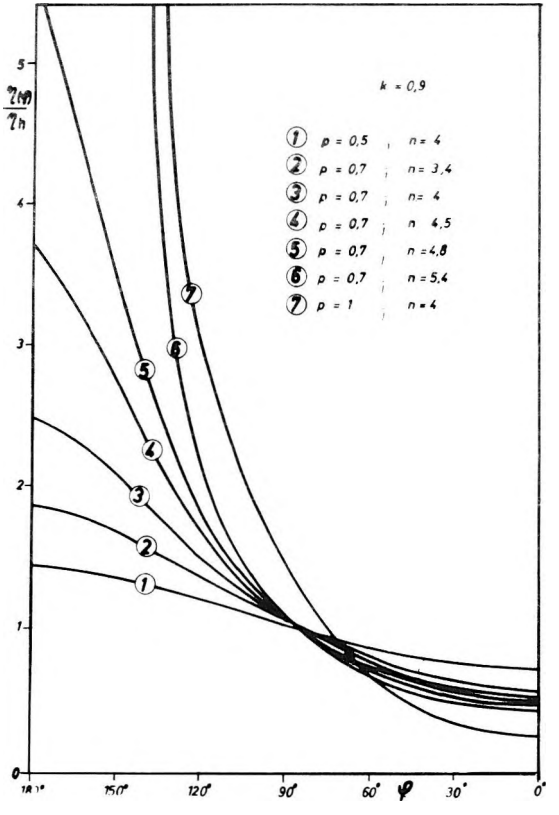

Fig. 6. Variation of η_i as function of the vertical layer boundary and of the relative position of the guard electrode pair ($p = \overline{A_0A}/d$)

6. ábra. η_i változása a vertikális réteghatár és a figyelőelektróda-pár egymáshoz képesti helyzetének függvényében ($p = \overline{A_0A}/d$)

Рис. 6. Изменение η_i в зависимости от вертикального раздела и взаимного положения пары наблюдательных электродов ($p = \overline{A_0A}/d$)

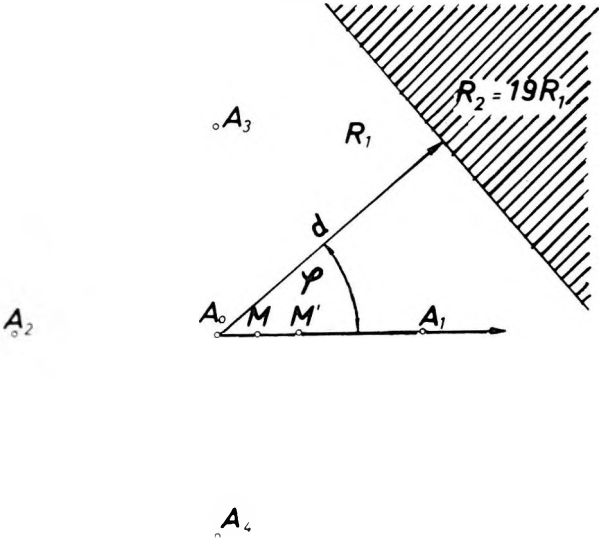

Fig. 7. Relative position of vertical layer boundary with respect to the 4-focusing-electrode spread

7. ábra. Vertikális réteghatár helyzete a négyterelős teritéshez viszonyítva

Рис. 7. Положение вертикального раздела по отношению к установке с четырьмя фокусирующими электродами

Figure 8 presents a field example for the determination of η_i and R_a for the separate setting of the zero potential difference between the guard electrodes in the four directions. The determination is based on an observation drawn from Fig. 6, *viz.* the η value free from lateral effects should be read off around the midpoint between the maximum and the minimum.

In conclusion, it can be stated that for the focused-field surface sounding a 2-focusing arrangement of spread quotient $n = 2.22$ should be used, with occasional measurements with a 4-focusing arrangement for checking purposes.

5. Focused-field profiling

It is quite another situation if we are concerned with the detection of the lateral step-like resistivity change (due to a fault). In this case, the condition $\Delta U = 0$ should be set in at least 4 directions, or we could also use two 4-focusing arrangements rotated by 45° with respect to each other. The spread quotient should also be increased, an optimal choice being $n = 5$. In this case we can also obtain a negative η value for $\varphi = 180°$ which makes the localization of the maximum and minimum more reliable. $\eta(\varphi)$ increases from $+0$ to $+\infty$, then further, from $-\infty$ to -0; that is, the negative η of small absolute modulus will yield the maximum. The exact tracing of the maximum and minimum is very important since this provides the direction of the normal erected to the vertical layer boundary of positive resistivity contrast.

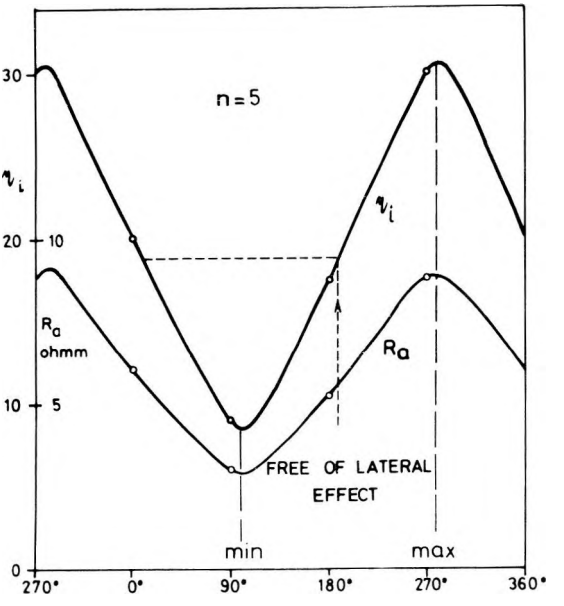

Fig. 8. Variation of η_i and R_a as functions of the position of the guard electrodes (field example)

8. ábra. η_i és R_a változása a figyelőelektródák helyzetének függvényében (terepi példa)

Рис. 8. Изменения η_i и R_i в зависимости от положения наблюдательных электродов (пример полевой работы)

The sensitivity to asymmetry of the focused-current arrangement can be utilized by separately setting the condition $\Delta U = 0$ in each direction [EGERSZEGI 1982], as is usually done in focused-current profiling. This accentuates the effect of lateral resistivity changes. In the case of a 2-focusing-electrode arrangement, if the spread direction is perpendicular to the vertical layer boundary, two values should be distinguished. η_π refers to the case where, approaching the resistivity contrast the straight line normal to the boundary and the line across the guard electrodes form an angle of 180°, η_0 to the case when this angle is 0°.

The variation of η_π in the case of focused-current profiling is shown in *Fig. 9.* The curves were computed for different spread quotients and spread lengths. The left-hand-side of the figure is linearly scaled in order to plot the negative values, the right-hand-side is logarithmic so that values less than one can more clearly be seen.

Figure 9 illustrates that in certain cases, due to the large asymmetry, the value of η can also be negative and it tends to zero from the negative side.

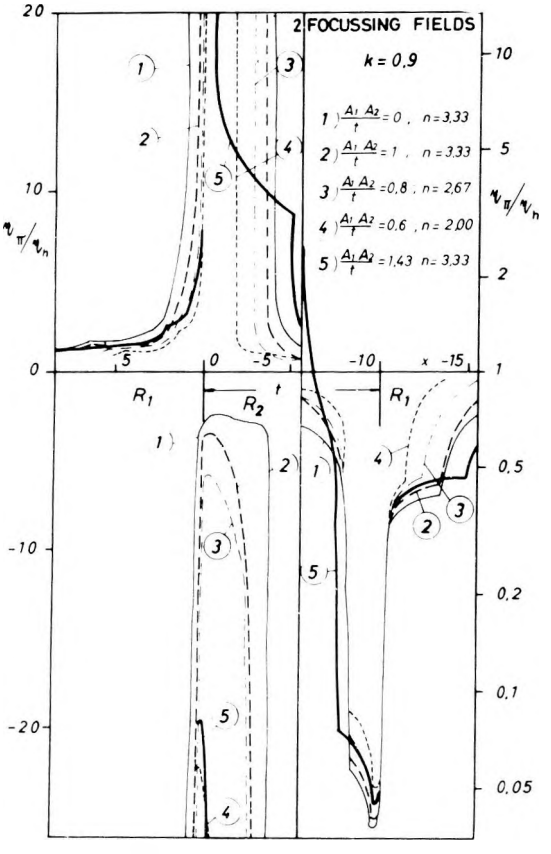

Fig. 9. Variation of η_π along the profile ($k = 0.9$)

9. ábra. η_π szelvénymenti változása ($k = 0.9$)

Рис. 9. Изменение η_π по профилю ($\kappa = 0.9$)

6. Application of "compensating circuit method" in mines

In the focused-current arrangement—for positive resistivity contrasts and if we do not take into account the distant electrodes—we get a relatively large "penetration" as compared with spread length. This seems ideal for in-mine applications where there is a quite small surface available for measurements but the electrodes B, B_0 and N can be placed far apart along the drifts. With a 2-focusing-electrode arrangement there is no obstacle to planting the electrodes in the drifts — the only problem is that a bidirectional focusing is not sufficient for measuring the whole field. On the other hand, a 4-focusing arrangement can be realized only in a restricted manner which is certainly not satisfactory in spite of the relatively large "penetration".

In mines it is advisable to substitute the focused-current arrangement by the so-called compensating circuit technique [EGERSZEGI 1979]. This is applicable in the first place in coal seams where the effect of the embedding layers can be reduced by focusing the measuring current or by compensating for the potential change due to the surrounding layers in order to get more unambiguous and accurate results. This solution utilizes the favourable properties of the potential and focused-current arrangements by means of variable spread quotients so that the compensating current strength cannot be adjusted by means of guard electrodes but some other procedure should be applied. The electrode arrangement is shown in *Fig. 10*. During sounding the compensating electrodes A and the measuring electrode M are moving such a way that the ratio l/A_0M is kept constant.

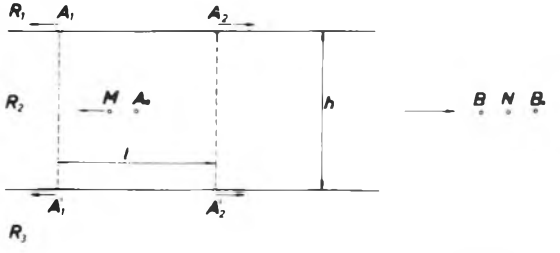

Fig. 10. Electrode arrangement with compensating circuit

10. ábra. Kompenzáló áramkörös elektróda-elrendezés

Рис. 10. Расположение электродов с компенсирующей схемой

The measuring current I_0 causes a potential

$$U_{M_i} = U_{M_h} + U_{M\Delta}\,, \tag{5}$$

at electrode M, where U_{M_h} is the potential that would be measured over an infinitely thick layer of specific resistivity R_2. The task of the compensating circuit is to produce a potential at electrode M having the same magnitude but the opposite sign as that of $U_{M\Delta}$:

$$U_{M_k} = -U_{M\Delta}$$

$$U_{Mk} = \frac{R_2 I_0}{2\pi A_0 M}\, y f(R_1, R_2, R_3, u), \tag{6}$$

where

$$u = \frac{2A_0M}{h} \quad \text{and} \quad y = \frac{I_1}{I_0}$$

and h is the thickness of the coal seam [EGERSZEGI 1979]. I_1 is the strength of the current introduced from the side of specific resistivity R through current electrodes A_1 and A_2:

$$I_3 = I_1 \frac{R_1}{R_3}$$

where the indices 1, 2 and 3 refer to the overlying layer, to the coal seam and to the underlying layer, respectively. By means of Eqs. (5) and (6) we can establish a relationship between k and U_{M_i} for known values of the resistivities R_1, R_2, R_3 and for a given value of u (see *Fig. 11* for the case $R_1 = R_3 = 9R_2$, $u = 1/3$). By means of this relationship we can set the compensating current strength to this initial value of u. For other u values y can be computed by means of Eq. (6) *(Fig. 12)*, and we have to set this computed value during the measurement. For actual measurements, focused-current instruments have to be developed.

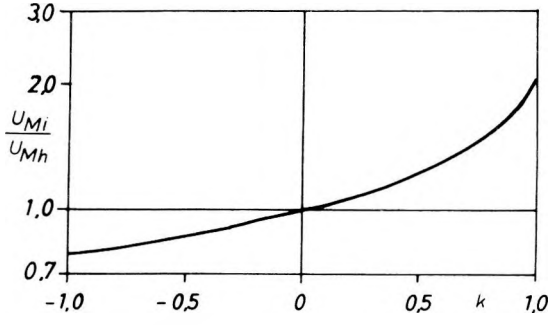

Fig. 11. Potential U_{M_i} as function of resistivity contrast (k)

11. ábra. U_{M_i} potenciál az ellenállás-kontraszt (k) függvényében

Рис. 11. Потенциал U_{M_i} в зависимости от контраста сопротивлений (κ)

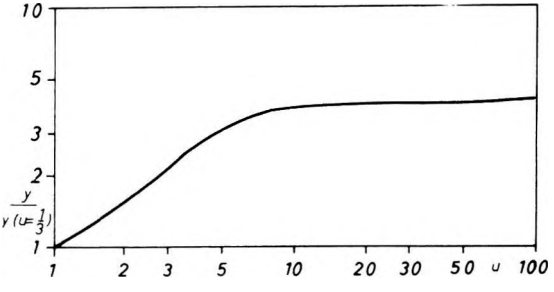

Fig. 12. Compensating/measuring current ratio (y) as function of spread length (u)

12. ábra. Kompenzáló- és mérőáram hányados (y) a terítési távolság (u) függvényében

Рис. 12. Отношение компенсирующего и измерительного токов (y) в зависимости от расстановки электродов (u)

7. Conclusions

It can be concluded that the focused-field method should be applied mainly in special cases.

In geoelectric measurements such a case is encountered if, for a positive resistivity contrast, a very large "penetration depth" is necessary compared with spread length or we have to determine the specific resistivity of the high resistivity basement. It is advisable to carry out the geoelectric sounding by a 4-focusing-current arrangement if the sounding curves indicate distortions due to lateral resistivity changes. In such cases the disturbing effects should be determined and eliminated.

In geoelectric profiling the high sensitivity of the method to asymmetry is advantageous for the detection of eventual faults. When measuring in mines the results should be made more accurate and unambiguous by the compensating circuit technique specially tailored to the surfaces available for measurements.

REFERENCES

Csókás J. 1963: A focused-field geoelectrical method. Acta Technica, **43,** 3—4, pp. 437—451

Egerszegi P. 1965: Detection of lateral inhomogeneities and the elimination of their effect in the focused-field method (in Hungarian). Magyar Geofizika, **6,** 2—4, pp. 9—12

Egerszegi P. 1967: A critical study of the geoelectric specific resistivity methods of different arrangement (in Hungarian). Magyar Geofizika, **8,** 2—3, pp. 92—99

Egerszegi P. 1979: Application of in-mine geoelectric measurements in mining engineering practice (in Hungarian). Magyar Geofizika, **20,** 6, pp. 228—238

Egerszegi P. 1980: The effect of electrode spacing and of the application of two circuits in geoelectric sounding (in Hungarian). Magyar Geofizika, **21,** 5, pp. 185—192

Egerszegi P. 1982: Asymmetry-sensitivity of different electrode arrangements (in Hungarian). Magyar Geofizika, **23,** 5—6, pp. 219—229

Roy A., Apparao A. 1971: Depth of investigation in direct current methods. Geophysics, **36,** 5, pp. 943—959

Szaraniec E. 1971: An effective array spacing for electrical sounding curves. Geophysics, **36,** 2, pp. 358—362

A FELSZÍNI TERELŐÁRAMOS MÓDSZER LEHETŐSÉGEI

EGERSZEGI PÁL

A tanulmány a két áramkör alkalmazásának lehetőségeit vizsgálva megállapítja, hogy a módszer korlátozottan alkalmazható tektonikai zavarok felszíni kimutatására, az alaphegység fajlagos ellenállásának pontosabb meghatározására, valamint nagyon zavart területen közel zavarmentes szondázási görbe felvételére. Bányában csak módosított formában alkalmazható a két áramkörös eljárás.

ВОЗМОЖНОСТИ НАЗЕМНОГО МЕТОДА ФОКУСИРОВАННОГО ПОЛЯ

П. ЭГЕРСЕГИ

В результате рассмотрения возможностей метода фокусированного поля в работе отмечается, что данный метод может в ограниченной мере применяться для выявления тектонических нарушений с дневной поверхности, более точного определения удельного сопротивления фундамента, а также для записи почти свободной от помех кривой в шумных районах. В шахтах метод фокусированного поля может найти применение только в видоизменённой форме.

GEOPHYSICAL TRANSACTIONS 1983
Vol. 29. No. 4. pp. 345-361

TIME DOMAIN IP EQUIPMENT AND METHOD FOR SOURCE DISCRIMINATION

József CSÖRGEI, András ERKEL, László VERŐ*

New results in IP have been presented mostly in the frequency domain with a short comment on the time domain. Data processing and interpretation problems of time domain laboratory and field measurements performed by a broad-band digital tape recorder are discussed here. A brief technical description of the equipment is given, followed by the data processing method based on the Marquardt algorithm. Decay curves measured in a very wide time interval are approximated by the sum of exponential terms. Distributions of amplitudes and time constants for laboratory and field measurements are presented. Measurements performed on rock samples and on geologically controlled sources serve as a basis for interpretation. The method may also permit removal of EM coupling.

d: IP method, time domain, curve shape analysis

1. Introduction

In recent years it has become quite obvious to geophysicists working on the time domain IP that the shape of decay curves could yield information on different physical and material parameters of mineralization or, in other words: different types of sources (sulphide or graphite) produce different decay curves. It is obviously unsatisfactory to compare the curves and declare that "this is similar to that, the other is different". Moreover a qualitative comparison is by no means simple. It is made difficult by the fact that decay curves have no characteristic points, like minima or maxima. Attempts have been made to transform these characterless curves into easily comparable secondary curves by mathematical methods. One of these methods is the differentiation of the decay curves [KOMAROV et al. 1979]. It has been demonstrated by laboratory measurements that the derivatives have a maximum and that the maximum can be found at different moments for different rocks (see *Fig. 1*). The rock samples were chosen in such a way that they could be characterized by only one type of mineralization, e.g. disseminated. Because of this the application of the method under field conditions is not so effective because ore bodies are mainly of mixed type, consequently the derivative of the measured curves ($\tilde{P}$) may have two or more rather uncertain maxima. The measurement itself is cumbersome, the decay curves need to be recorded over a very long period of time and the derivatives, measured or calculated, are very noisy.

There are two different ways for decay curve shape analysis:

i. A theoretical physical—chemical model ought to be found so that the

* Eötvös Loránd Geophysical Institute of Hungary, POB 35, Budapest, H—1440
Paper read at the 43rd Meeting of the European Association of Exploration Geophysicists, Venice, May 1981

very complex induced polarization phenomena can be described completely and so that the values of parameters of the theoretical model can be determined from field data. In this case parameters have a direct physical meaning.

ii. The other possibility is to describe mathematically the shape of decay curves by a certain number of parameters having no physical meaning.

The first of these seems to be more attractive, promising a direct solution for the main task, i.e. source discrimination. Wong's theoretical work do establish a good physical—chemical model for IP [WONG 1979]. It contains, however, a number of parameters. Wong's model and other models using slightly different approaches can be reduced to the Cole—Cole impedance formulation, widely used in the interpretation of complex resistivity data [PELTON et al. 1978]. The computation of the decay curves on the basis of the Cole—Cole model runs into difficulties. The inverse problem, i.e. the determination of the Cole—Cole parameters from time domain IP data is an even more complicated task. Although it is possible to relate the Cole—Cole parameters theoretically to physical properties of rocks, this procedure needs an empirical basis too.

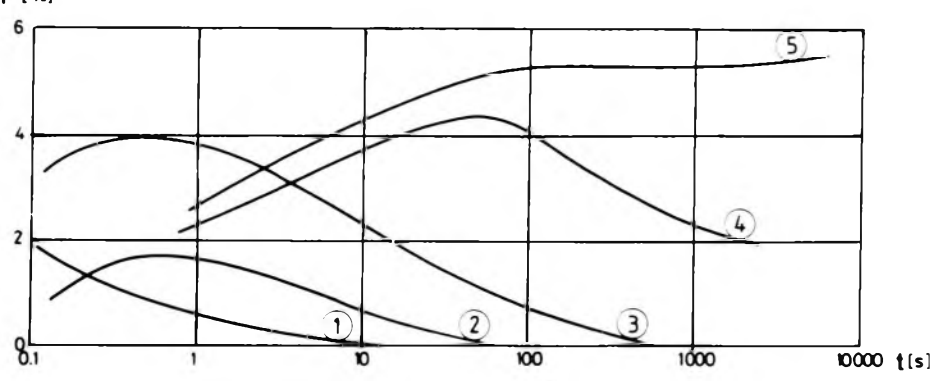

Fig. 1. Time derivatives of decay curves ($\tilde{P}$) measured on rock samples
1 — loose rocks; 2 — barren crystalline rocks; 3 — rocks with fine dissemination of sulphide, graphite and other electrically conductive minerals; 4 — disseminated sulphide ore; 5 — massive ore, veins

1. ábra. Kőzetmintákon mért lecsengési görbék idő szerinti deriváltjai ($\tilde{P}$)
1 — laza kőzet; 2 — kristályos kőzetek, ércmentes; 3 — kőzetek finoman hintett szulfidokkal, grafittal vagy más elektromosan jól vezető ásványokkal; 4 — hintett szulfidos érc; 5 — masszív érc, érctelérek

Рис. 1. Производные замеренных на образцах пород кривых затухания по времени ($\tilde{P}$)
1 — рыхлая порода; 2 — кристаллические породы без руды; 3 — породы с мелко вкрапленными сульфидами, графитом или другими электрически хорошо проводящими минералами; 4 — вкрапленная сульфидная руда; 5 — рудное тело, жилы

Because of the above features, our choice is the second of the two, viz. the pure, as much as possible simple mathematical representation of measured time domain IP data and the experimental determination of the dependence of mathematical parameters on mineralization types.

Mathematically speaking, decay curves are monotonically decreasing functions to be approximated by polynomial or exponential terms, among others. Returning to the well-known formula of WAIT [1959] we suppose that measured apparent polarizability values (P_t) can be described by using the expression

$$P_t = w_0 + \sum_{i=1}^{N} w_i \exp(-t/\tau_i) \tag{1}$$

where w_0 is a constant
w_i, τ_i are the exponential parameters
t is the time after current turn-off
N is the number of exponential terms.

Our aim is to get the so-called dynamic parameters (common name for w_0, w_i and τ_i).

Recently, computer programs based on the Marquardt algorithm have successfully been applied to solve different inversion problems. We have had good results in using the method for obtaining dynamic parameters. The only problem is the need for a relatively large computer memory if many data are used. But we have to use very many data, because we are working in a very wide time interval and more than 10 data/decade are necessary for good approximation. If we have 100—150 data and we are looking for 5—6 exponential terms, that is, 11—13 parameters, a computer of about 60 kbyte memory needs to be used (e.g. HP 9845).

2. The equipment

The equipment used in field and laboratory measurements is a four-channel digital tape recorder. Only certain technical data are mentioned in order to make distinction between the well-known instruments and our equipment.

— The sampling time series is quasi-logarithmic

$$t_{kj} = 2^k(1 + 0.1j)t_{00} \tag{2}$$

where t_{kj} is the sampling time of serial number kj
k is an integer, can be set between 0 and 13, to determine the length of the current-on and current-off intervals
j is an integer between 0 and 9
t_{00} is the first sampling time (128 ms).

— The ohmic portion of the primary voltage is bucked out by a D/A converter, therefore the remaining part can be measured in the same dynamic range as the secondary voltage.

— The dynamic range of the main 12-bit A/D converter is set automatically according to the signal level by means of binary gain setting

$$\varepsilon_s = 2^{s-1}\ \mu\text{V/bit} \tag{3}$$

and $s = 1, 2, \ldots, 6$.

— The number of measured decay curves of opposite sign is always greater than 3 (on average 8—10).

3. Data processing method

Processing of measured data takes place in two steps. The first step is a weighted averaging

$$\bar{U}_{kj} = \frac{1}{M-2} \sum_{m=2}^{M-1} \frac{U_{kj}^{m-1} - 2U_{kj}^{m} + U_{kj}^{m+1}}{4} \tag{4}$$

where $\bar{U}_{kj}$ is the weighted mean value of the voltage at t_{kj}

M is the total number of the recorded impulses

m is serial number of impulses, $2 \leqq m \leqq M-1$, impulse $m-1$ and $m+1$ have the same, impulse m the opposite polarity.

The next step is the determination of the dynamic parameters. These parameters can be determined by several methods. Probably the most simple of these is to compare the decay curves with precalculated "master curves" [HALVERSON et al. 1981]. The limits are the same as experienced in the similar interpretation of vertical electric soundings. Another method which is quite often applied is the so-called factoring. The advantage of the method is the small memory requirement easily met by programmable calculators. Its main drawback is the necessity for interactivity and subjective decisions. We ourselves used this method for several years [ERKEL, 1979]. There is, however, a further deficiency, viz. the constant which is generally present in the data cannot be determined in such a way. The processing of the decay curves of about 100 data was very time-consuming even though only a part of data was used simultaneously (samples of constant sampling rate) and there was no proof whether the approximation was the best possible or not. In possession of computers of larger memory we have turned to the computation of dynamic parameters by means of the Marquardt algorithm [MARQUARDT 1963]. Our computer program itself is the modified version of W. E. Ball's Fortran program translated to Enhanced Basic of Hewlett–Packard.

The main program has different input possibilities depending on the type of tasks. We first needed to check the parameters obtained by the interactive method. To do this we had a fairly good initial guess and expected only small changes of parameters. We then processed about 20 curves by the new program, in most cases there was in fact only a small difference between the parameter sets (less than 10%), and the number of parameters remained the same. The main task is, however, the processing of new, unprocessed data. In this case, of course, we had no initial guess and we practically did not limit the possible intervals for dynamic parameters. After performing several experiments it was found that there was no need for initial guesses, only the number of parameters was to be determined (up to 21). Initial guesses for amplitudes and time constants were calculated from the first sample, the sampling interval and

number of terms (only for curves without EM coupling), since the Marquardt algorithm provides a rapid convergence even in case of a poor initial guess. The sum of the squared differences between measured and calculated values (Φ) decreased by orders of magnitude during the first iterations, the parameters changed significantly too. After that both the sum and parameters changed only slightly as shown in *Fig. 2.* During the processing of decay curves disturbed by EM coupling or noise the demand came up to limit the interval of allowed changes. Without these limitations the parameters reached unreal values, time constants became much longer than the sampling interval, amplitudes became greater by orders of magnitude than the measured values. Such parameters are considered as unreal because of mathematical and not physical reasons; moreover the parameters did not show the same trend of change as mentioned before.

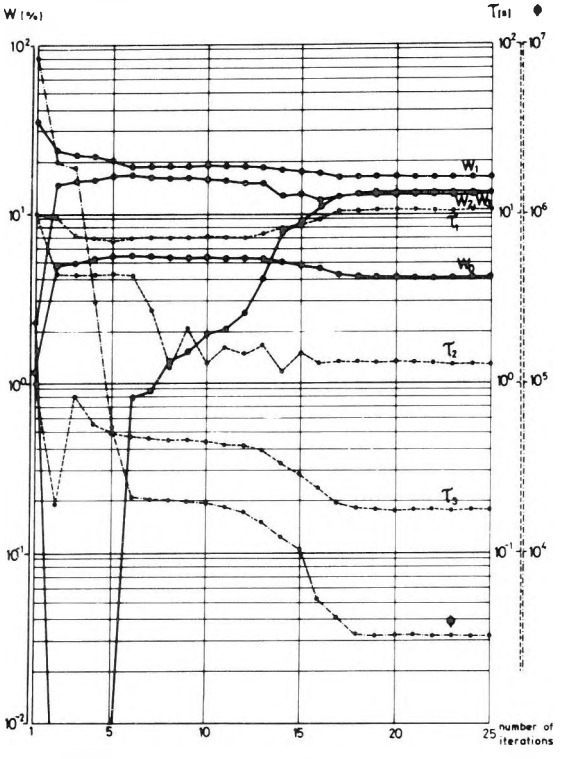

Fig. 2. Change of dynamic parameters (w_i, τ_i) and Φ during the iteration process

2. ábra. A dinamikus paraméterek (w_i, τi) és Φ változása az iterációs folyamat során

Рис. 2. Изменение динамических параметров (w_i, τ_i) и Φ в итерационном процессе

Almost every parameter changed significantly in every iteration on the one hand, Φ remained unchanged on the other hand. To approximate measured values closer than the measuring error has no practical meaning. An obvious choice would be to calculate the scattering or standard deviation of samples

belonging to the same moment, to average them in order to get a limit and stop the program if the averaged difference between measured and calculated values falls within this limit. We carried out some experiments on noisy curves and the method worked well, but not on curves with strong EM coupling. The processing of such curves requires the direct limitation of parameters; later we shall return to this problem.

We are in the middle of experiments concerning every step of data processing. For the time being stacking, digital filtering and computation of exponential parameters are carried out separately, with the possibility of software changes, but for our final aim—a microprocessor controlled system—a complete and many times checked processing system is needed.

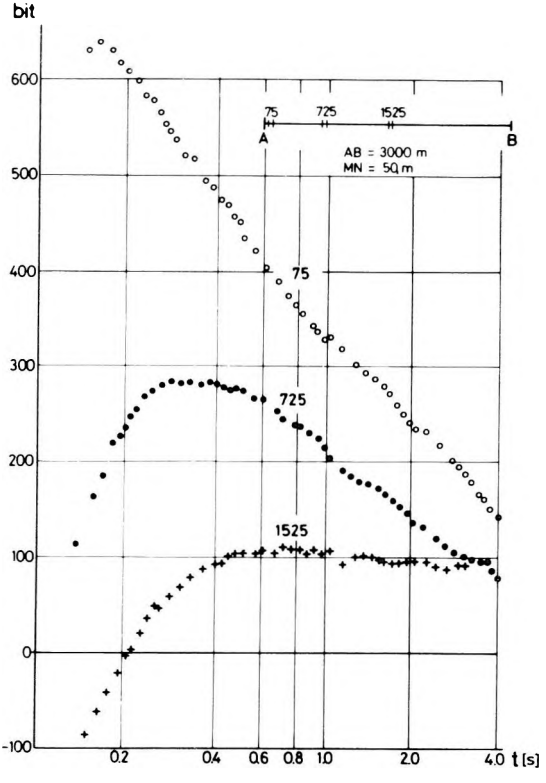

Fig. 3. Decay curves measured with long current bipole (gradient array). Apparent resistivity is about 50 Ωm along the profile

3. ábra. Hosszú áramdipóllal mért lecsengési görbék (gradiens elrendezés). A látszólagos ellenállás 50 Ωm körül van a szelvény mentén

Рис. 3. Кривые затухание, измеренные с длинним токовым диполем (градиентная установка). Кажущееся сопротивление составляет ок. 50 Ωм по профилю

4. Proper choice of the number of exponential terms

First we would like to demonstrate what kind of approximation can be made if the signal-to-noise ratio is similar to that shown in *Fig. 3*. We have found that the already mentioned difference between measured and calculated values (δ_{kj}) can best be used to characterize the approximation. It could be characterized by one number too, namely by Φ, but the distribution of δ_{kj} yields very important information. Therefore the final printout of computer processing—besides the dynamic parameters, of course—contains the plot of δ_{kj} and Φ. Two printouts are shown in *Fig. 4/a* and *b*. The very systematic, almost sine wave pattern of δ_{kj} (in logarithmic time scale) is surprising. In connection with this phenomenon the basic question concerning the decision on the number of terms necessary for the best approximation, will be discussed.

As in many other cases we have to make a compromise. Obviously the greater the number of components the better the approximation. But our aim is to use a minimum number of components. A possible solution is to start with

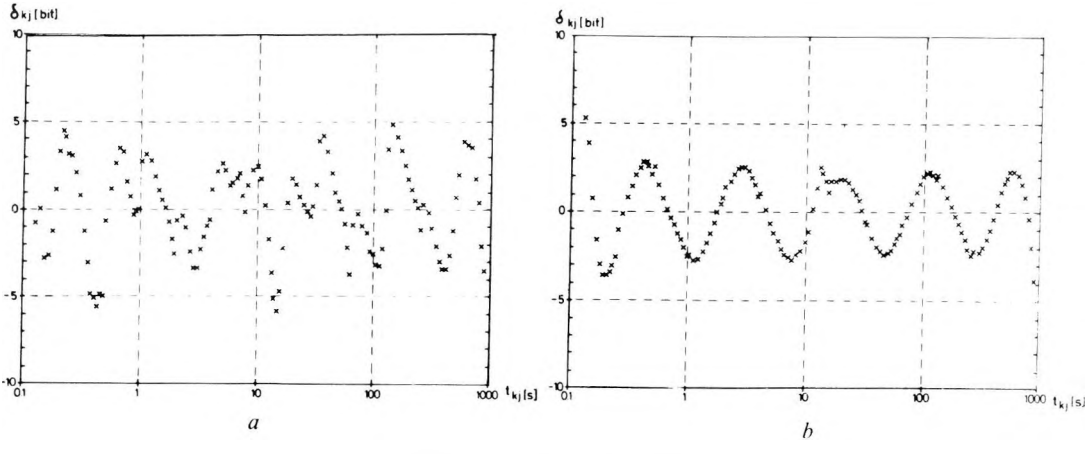

Fig. 4. Final printout of data processing
Dynamic parameters
4. ábra. Az adatfeldolgozás végeredménye
Dinamikus paraméterek

Рис. 4. Окончательный результат обработки материалов
Динамические параметры

a) $w_0 = 0.06\%$
$w_1 = 0.48\%$ $\tau_1 = -526.3$ s
$w_2 = 0.48\%$ $\tau_2 = -83.3$ s $\Phi = 810$
$w_3 = 0.37\%$ $\tau_3 = -13.51$ s
$w_4 = 0.29\%$ $\tau_4 = -2.60$ s
$w_5 = 0.34\%$ $\tau_5 = -0.035$ s

$\sum_{i=0}^{5} w_i = 2.02\%$

b) $w_0 = 0.52\%$
$w_1 = 2.18\%$ $\tau_1 = -344.8$ s
$w_2 = 1.67\%$ $\tau_2 = -50.0$ s $\Phi = 480$
$w_3 = 1.42\%$ $\tau_3 = -7.81$ s
$w_4 = 1.31\%$ $\tau_4 = -1.614$ s
$w_5 = 1.56\%$ $\tau_5 = -0.165$ s

$\sum_{i=0}^{5} w_i = 8.66\%$

only one exponential component, then to increase the number of components (N in equation 1) step by step and in the meantime to follow with attention the change of Φ and the distribution of δ_{kj}. So far as Φ can be decreased significantly by increasing N this procedure is worth being continued and finally the differences must show a randomly scattered pattern (taking into consideration the smoothing effect of the digital filtering, i.e. weighted averaging). In the course of increasing N the distribution of δ_{kj} many times displayed a pattern similar to that shown in *Fig. 4/b* It is certain it was not noise. The reason was that we did not allow enough components, but used just one less—and this bears emphasizing. The use of more components is unnecessary. This is shown in *Fig. 5.* Three components are not enough because of systematic error; four components offer the best solution; the use of $N=6$ is excessive giving an approximation which is by no means better. We have found a fairly good test for deciding the optimum number of exponential terms.

For fully automatic data processing it is easier to formulate the process in the opposite way, i.e. to start with maximum of N and to decrease it step by

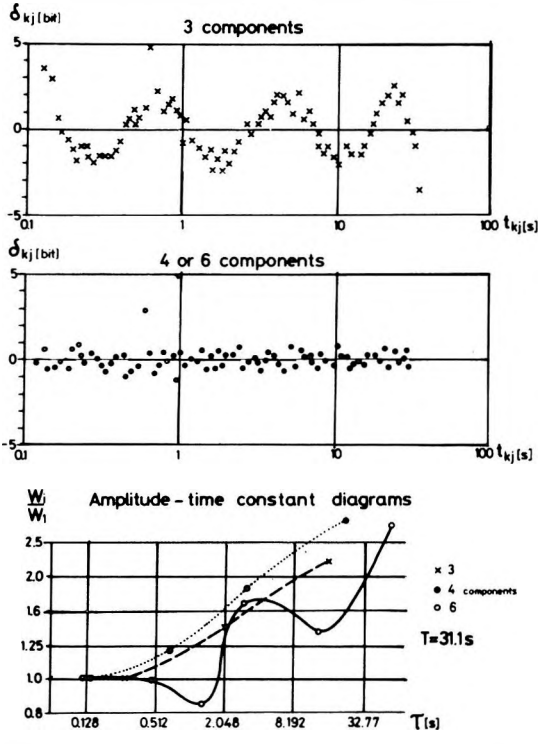

Fig. 5. Distributions of δ_{kj} and the normalized amplitude—time constant diagrams for approximations by different numbers of components

5. ábra. δ_{kj} eloszlása és a normált amplitudó—időállandó diagramok különböző számú komponenssel való közelítés esetén

Рис. 5. Распределение δ_{kj} и диаграммы нормированная амплитуда—постоянная времени при аппроксимации различным количеством составляющих

step. If Φ increases by less than 10% (or 5% or 1%) during the successive iterations one or more components could be deleted

a) the term having a time constant shorter than $t_{00}/5$,

b) terms with time constants whose ratio is less than 1.6 can be drawn together (the limit depends on the accuracy of the equipment)

c) the term having a time constant longer than 10 times the sampling interval (its amplitude is added to the constant).

The iteration process is carried on using the reduced N, Φ and the distribution of δ_{kj} should be checked again to decide whether the reduction of N was correct or not. The criteria are the same: the trend of Φ and the pattern of δ_{kj}.

5. Basis of interpretation

It is well-known that ZONGE and HUGHES [1981] have divided the Cole—Cole diagrams into three basic groups *A*, *B* and *C*, representing decreasing, horizontal and increasing types. We have arranged a similar grouping of amplitude—time constant distributions. Having a non-physical model it is obvious that amplitudes and time constants have no direct physical meaning. The distribution of amplitudes, however, is different for different sources. As the sum of w_i, i.e. the exponential amplitudes normalized to the primary signal—the apparent polarizability with 0 second delay time—sometimes yields no information, in the final plotting of results w_i values are normalized once more to the amplitude belonging to the shortest time constant as shown in *Fig. 6* (this

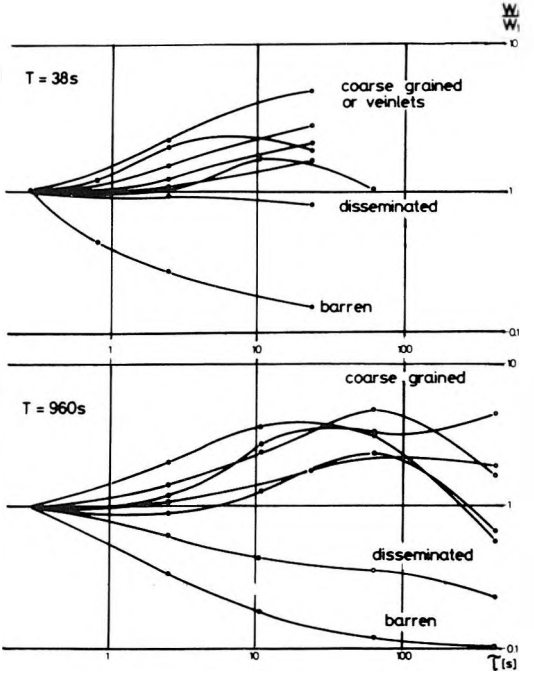

Fig. 6. Normalized amplitude—time constant diagrams obtained using short and long charging pulses (laboratory measurements)

6. ábra. Hosszú és rövid gerjesztéssel kapott normált amplitudó—időállandó diagramok (laboratóriumi mérések)

Рис. 6. Диаграммы нормированная амплитуда—постоянная времени, полученные с долгим и коротким возбуждением (лабораторные измерения)

all holds true only for EM coupling free curves or if the EM coupling term is neglected). These normalized amplitude—time constant diagrams in double logarithmic scale serve as a basis for interpretation.

Diagrams belonging to different ore types or geologic models could be found empirically only, by a number of experiments being carried out and the results being used in a statistical way.

6. Measurements on rock samples

Before going into detail about applying this method it might be useful to explain briefly the kinds of exploration tasks that we are seeking to solve by IP in Hungary. In our country the base metal occurences are linked mainly with young, hydrothermally altered Miocene—Eocene andesites and are characterized by large horizontal extent and low, uneconomical grade, at least in the depth interval of IP measurement. Within the basically pyrite mineralizations there are zones of higher grade copper-polymetallic ores, in other words we have porphyry copper deposits of poor quality. A small amount of higher grade ores can be found at the edges of the volcanic body, if the country rock was limestone or dolomite (skarn), but we have no massive ore. With regard to texture and grain size there are very fine grained disseminations, veinlets and stringers (stockwork). The highest grade ores (about 15—20%) are of veinlet type, the thickness of the fissure fillings is 3—10 mm. Therefore we have to study the decay curves of the ore types mentioned before (in our domestic work we have rarely encountered a need for sulphide—graphite discrimination).

We have carried out very many laboratory measurements on cores. In Fig. 6 amplitude—time constant diagrams of barren rock, disseminated and veinlet type mineralizations are shown (andesite matrix with pyrite, magnetite and chalcopyrite). Measurements were performed by short (58 s) and long (960 s) charging pulses. For veinlet type mineralization the amplitudes increased with increasing time constant and the trend was nearly the same for short and long charging pulses, the place of maximum depends on the length of the charging pulse. For disseminated mineralization there was no change in the amplitudes if a short charging pulse was used, the trend was slightly decreasing if long pulse was used. For barren rocks in both cases there is a rapid decrease in amplitudes. It is worth mentioning thet the shape of diagrams was influenced by the length of the charging pulse, but the basic trend remained the same for a given texture type.

In *Fig. 7* the effect of anisotropy is shown. The direction of the current flow with respect to the sample was changed during the measurements. For the sample containing only disseminated mineralization (sample B) the amplitude distribution showed no change; for samples with fissure filling (A) or oriented stringers (C) both the shape and the values of amplitudes strongly depended upon direction of current. In rock sample measurements, effects are always exaggerated, e.g. apparent polarizability values are very high, the anisotropy is

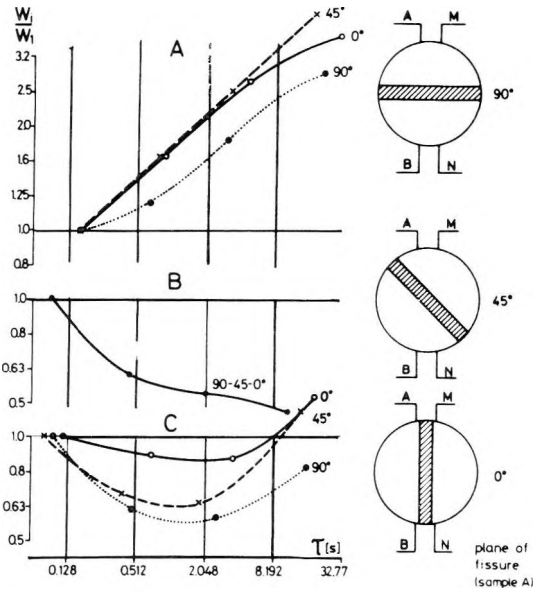

Fig. 7. Effect of anisotropy: dynamic parameters for very anisotropic (*A*), homogeneous (*B*) and moderately anisotropic (*C*) rock samples as a function of the current's direction

7. ábra. Az anizotrópia hatása: nagyon anizotróp (*A*), homogén (*B*) és mérsékelten anizotróp (*C*) kőzetminták dinamikus paraméterei az áram irányának függvényében

Рис. 7. Влияние анизотропии: динамические параметры сильно анизотропных (*A*), однородных (*B*) и умеренно анизотропных (*C*) образцов горных пород в зависимости от направления тока

very strong, the shapes of the diagrams are very different. In field measurements we could not expect the same (because of the dilution factor) so it was mandatory to carry out field measurements on geologically controlled sources too.

7. Field measurements

In a Miocene volcanic mountain AB rectangle IP measurements were made by conventional TD instruments, followed by the determination of dynamic parameters for source discrimination on anomalies only. The interpretation of decay curves measured over disseminated and veinlet type mineralizations is shown in *Fig. 8*. Because the signal-to-noise ratio was favourable we calculated the differential curves too. The apparent polarizabilities ($P_{0.5}$ measured with 32 s long charging) are nearly constant along the profile (15—17%). The derivatives of the decay curves measured with long charging pulses and the shape of the amplitude—time constant distributions are very similar. The trends of changes are the same as experienced in laboratory measurements, only the absolute values are smaller.

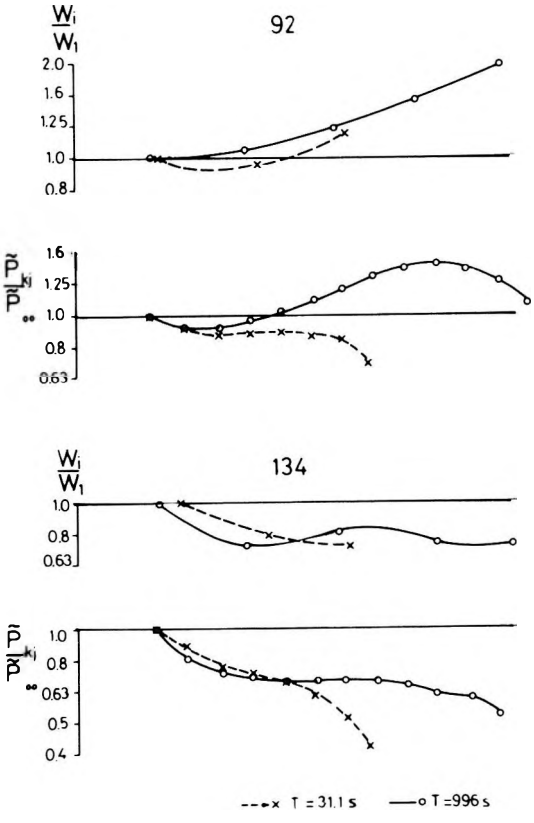

Fig. 8. Normalized amplitude—time constant (w_i/w_1) and derivative ($\tilde{P}_{kj}/\tilde{P}_{00}$) curves for veinlet (92) and disseminated (134) mineralizations obtained by different charging pulses

8. ábra. Normált amplitudó—időállandó (w_i/w_1) és derivált ($\tilde{P}_{kj}/\tilde{P}_{00}$) diagramok hálós-eres (92) és hintett (134) ércesedés esetén, különböző hosszúságú gerjesztésekkel

Рис. 8. Диаграммы нормированная амплитуда—постоянная времени (w_i/w_1) и крувые производных ($\tilde{P}_{kj}/\tilde{P}_{00}$) для жильного (92) и вкрапленного оруденения (134) при разных продолжительностях возбуждения

In the measurements shown in *Fig. 9* only the dynamic parameters could be used for source discrimination, the derivative curves were very noisy and characterless. The apparent polarizability is somewhat lower along the profile (it was the ridge of an elongated IP anomaly). It is known from drillings that the profile can be divided into two parts. On the eastern part the mineralization consists of very finely disseminated pyrite only, on the western half the grain size is somewhat coarser. The change of grain size reflects different mineral composition: the bulk of ore minerals is pyrite, the chalcopyrite content is, however, somewhat higher, but not of economic interest. The apparent polarizabilities are different at the two halves of the profile, but when IP parameters of the whole investigation area are known it is impossible to discriminate on the basis of apparent polarizability alone.

TD measurements for source discrimination were carried out by using short (31.1 s) and long (996 s) charging pulses. Of course, the measuring interval was longer when the charging pulse was longer. Decay curves of shorter pulses can be described by 3, the longer ones by 4—5 terms. If conditions were favourable (high signal-to-noise ratio) the amplitude—time constant diagrams of different charging pulses have exactly the same shape, though time constants are different (stations 98 and 116). In most cases the trend of the

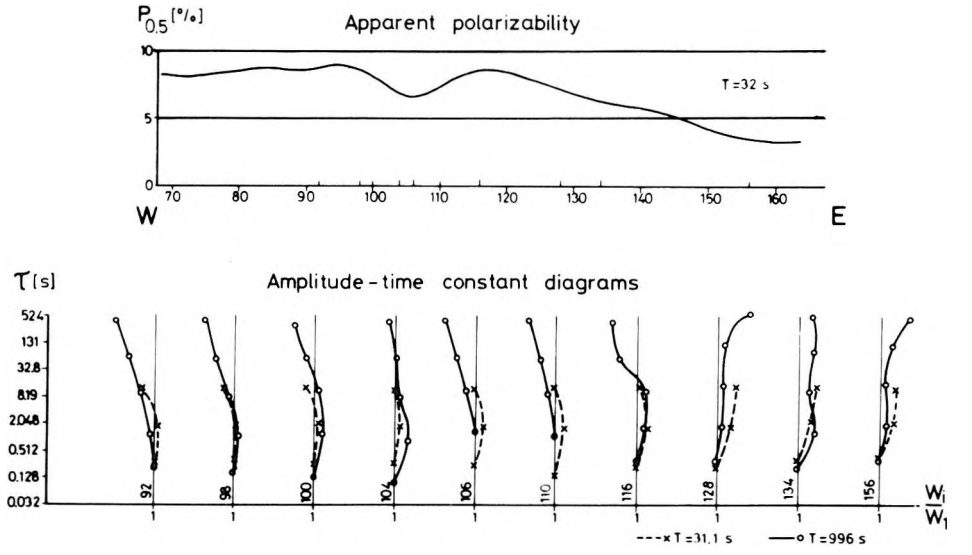

Fig. 9. Apparent polarizability and normalized amplitude—time constant diagrams along a profile with slightly different mineralizations

9. ábra. Látszólagos gerjeszthetőség és normált amplitudó—időállandó diagramok olyan szelvény mentén, ahol az ércesedés jellege kissé változik

Рис. 9. Диаграммы кажущейся поляризуемости и нормированная амплитуда—постоянная времени по профилю с небольшим изменением характера оруденения

diagrams for different charging times is similar (stations 92, 104, 156). About 10% of measurements yielded different diagrams for different charging times (stations 106, 110), mainly because of poor signal-to-noise ratio.

From field measurements two conclusions can be drawn

1) the dynamic parameters do not depend on measurement parameters, but by using long charging and measuring times more terms can be determined and the shape of the diagrams becomes unambigous,

2) the normalized amplitude—time constant diagrams obviously differ between the eastern and western parts of the profile; in the middle there is a transition zone with characterless diagrams.

Otherwise the unambiguity of dynamic parameters was also checked on these curves. By processing the same data set repeatedly, using different initial guesses and allowing a different N we finally got nearly the same values as the best approximation and the scattering of the parameters did not influence the shape of the diagrams.

8. Removal of EM coupling

We have already mentioned the problem of EM coupling. In Fig. 3 a very distorted decay curve can be seen, it is dominated over a relatively long interval

by EM coupling (curve 1525). It is more reasonable to use an exponential term to describe the EM coupling, its substantial difference being that EM coupling has a negative sign (in most cases). Our program has an option for computing negative amplitudes. We have processed decay curves measured along a profile and the results were not the best (some decay curves are shown in Fig. 3). It should be noted that the AB line of the gradient array was very long (3 km) therefore the signal-to-noise ratio was very low and only the first part of the decay curves could be used for further processing. Relatively short, noisy curves with strong EM coupling are not the best for processing and the results reflected the problems: some parameters reached unreal values. Following the changes of parameters along the profile it appeared that (see Fig. 10)

a) moving off from the current electrode the absolute value of EM coupling amplitude increases, whereas the time constant does not change,

b) amplitudes describing IP (w_0 and w_1) reached unreal values at the same distance from AB, their sum being almost the same (in other words parameters became strongly correlated),

c) at the same distance τ_1 became much longer than the sampling interval.

It was clear that because of the poor signal-to-noise ratio in the middle of the array the indirect limitation of parameters discussed before cannot be used, a direct method is needed, viz. the fixing of some parameters. We have used the averaged parameters of those parts of the profile which provided acceptable parameters for EM coupling and IP too. We allowed these parameters to fluctuate within a narrow band only. The fixed parameters were the time constants. The fixing of parameters resulted in an increase of the squared sum, but since no other possibility is available we have to accept this. The results of processing with fixed parameters reflect the changes of the depth of the polarizable rock masses covered by young sediments.

One measurement does not provide sufficient basis to draw general conclusions; there are, however, hopes of solving the EM coupling removal in TD.

Fig. 10. EM coupling removal (array is shown in Fig. 3). Prime denotes results obtained with fixed parameters and the fixed parameters themselves. For simplicity w_0 is not plotted

10. ábra. Az EM csatolás eltávolítása (az elrendezést a 3. ábra mutatja). A vessző a rögzített paraméterekkel kapott eredményeket és magukat a rögzített paramétereket jelöli. Az egyszerűség kedvéért w_0-t nem ábrázoltuk

Рис. 10. Устранение ЭМ связи (установка показана на рис. 3). Запятая показывает результаты, полученные с зафиксированными параметрами и самые зафиксированные параметры. Для простоты значение w_0 не изображено

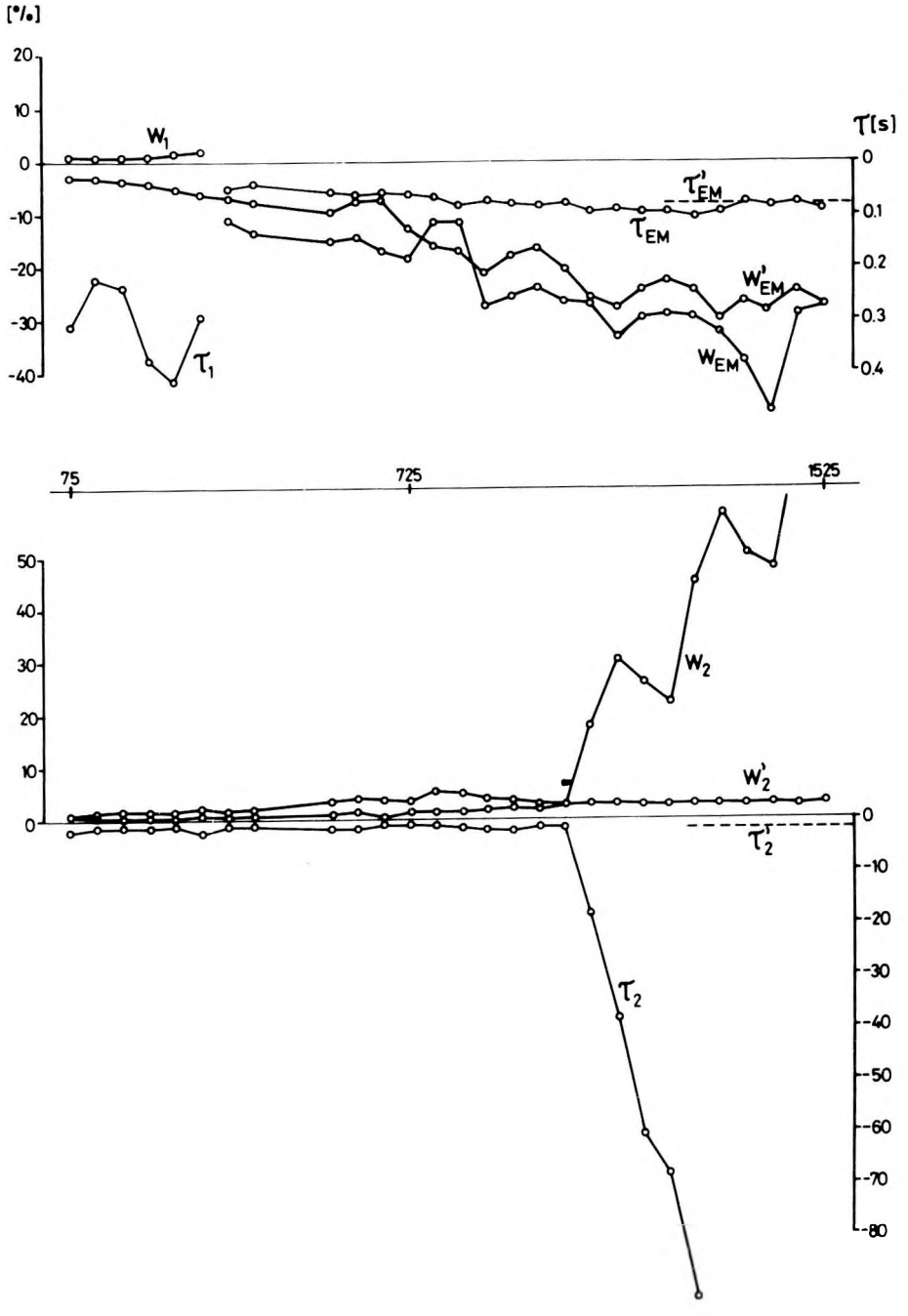
[%]
20
10
0
-10
-20
-30
-40
W1
τ1
τ'EM
τEM
W'EM
WEM
τ[s]
0
0.1
0.2
0.3
0.4
75
725
1525
50
40
30
20
10
0
W2
W'2
τ'2
τ2
-10
-20
-30
-40
-50
-60
-70
-80

9. Conclusions

The examples shown are the first successful results of a new data acquisition and processing system. The most important conclusions are as follows:

1) the data processing method is suitable to describe 80—130 samples of decay curves by a limited (7—13) number of dynamic parameters with sufficient accuracy,

2) sources of different texture really give rise to different dynamic parameter distributions and these distributions can be used for source discrimination,

3) solving of the EM coupling problem is possible,

4) further effort is needed to study the use of shorter charging times and the similarities with other methods,

5) very many laboratory and field measurements should be carried out to provide experimental data for interpretation purposes,

6) to increase production a microprocessor controlled data acquisition and processing system should be built,

7) data processing should be completed with parameter correlation and standard deviation computations.

Acknowledgement

One of the authors (L. V.) wishes to express his thanks to B. D. Smith of the United States Geological Survey for encouragement and for suggesting some useful modifications.

REFERENCES

Erkel A., Simon P. and Verő L. 1979: Measurement and interpretation of the dynamic characteristics of induced polarization decay curves. Geophysical Transactions, **25,** 61—72

Halverson M. O., Zinn W. G., McAlister E. O., Ellis R. B. and Yates W. C. 1981: Assessment of results of broad-band spectral IP field tests, in Advances in induced polarization and complex resistivity. Edited by J. S. Sumner. The University of Arizona, Tucson, Arizona, 295—344

Komarov V. A., Mikhailov G. N., Khloponina L. S., Ioffe L. M. and Smirnov A. A. 1979: Methodological guide for geoelectric system SVP 74, (in Russian) Lenuprizdat, Leningrad 32—33

Marquardt D. W. 1963: An algorithm for least-squares estimation of non-linear parameters. J. Soc. Indust. Appl. Math. **11,** 431—441

Pelton W. H., Ward S. H., Hallof P. G., Sill W. R. and Nelson P. H. 1978: Mineral discrimination and removal of inductive coupling with multifrequency IP. Geophysics, **43,** 3, 588—609

Wait J. R. 1959: The variable frequency method, in Overvoltage research and geophysical applications, edited by J. R. Wait, Pergamon Press, London, 29—49

Wong J. 1979: An electrochemical model of the induced polarization phenomenom in disseminated sulfide ores. Geophysics, **44,** 7, 1245—1265

Zonge K. L. and Hughes L. J. 1981: The complex resistivity method, in Advances in induced polarization and complex resistivity, edited by J. S. Sumner, The University of Arizona, Tucson, Arizona, 163—208

IDŐTARTOMÁNYBAN DOLGOZÓ BERENDEZÉS ÉS MÓDSZER A GERJESZTETT POLARIZÁCIÓS HATÓK MINŐSÍTÉSÉRE

CSÖRGEI JÓZSEF, ERKEL ANDRÁS, VERŐ LÁSZLÓ

A gerjesztett polarizációs módszerben új eredményeket főleg a frekvencia tartományban érnek el és a publikációkban csak röviden utalnak az idő tartományra. Egy szélessávú digitális magnetofonnal végzett időtartománybeli, laboratóriumi és terepi mérések adatfeldolgozási és értelmezési problémáit tárgyaljuk. A berendezés rövid műszaki leírását a Marquardt algoritmuson alapuló adatfeldolgozás ismertetése követi. A nagyon széles időtartományban mért lecsengési görbéket exponenciális tagok összegével közelítjük. Az amplitudók és időállandók laboratóriumi és terepi mérésekből kapott eloszlását mutatjuk be. Kőzetmintákon és földtanilag jól ismert anomáliákon végzett mérések szolgálnak az értelmezés alapjául. A módszer az elektromágneses csatolás kiküszöbölését is lehetővé teszi.

АППАРАТУРА И МЕТОДИКА ДЛЯ РАЗЛИЧЕНИЯ ИСТОЧНИКОВ ВЫЗВАННОЙ ПОЛЯРИЗАЦИИ В ВРЕМЕННОМ ДИАПАЗОНЕ

Й. ЧЁРГЕИ, А. ЭРКЕЛ, Л. ВЕРЁ

По методу ВП новые результаты достигаются прежде всего в частотном диапазоне, а относительно временного диапазона в публикациях даются только короткие ссылки. В работе обсуждаются проблемы обработки и интерпретации данных лабораторных и полевых измерений, проведенных при помощи широкополосного цифрового магнитофона в временном диапазоне. Краткому описанию аппаратуры следует изложение процедуры обработки данных, основанной на алгоритме Маркарда. Кривые затухания, замеренные в очень широком диапазоне времени, аппроксимируются суммой экспоненциальных членов. Приводится распределение амплитуд и постоянных времени, полученных по лабораторным и полевым измерениям. В основу интерпретации лежат измерения, произведенные на образцах горных пород и геологически хорошо изученных аномалиях. Метод также позволяет устранить электромагнитную связь.